Kinematic complexity of accretionary wedges- Insights from analogue models towards understanding natural wedges

Dissertation
zur Erlangung des akademischen Doktorgrades
doctor rerum naturalium (Dr. rer. nat.)
im Fachbereich Geowissenschaften
an der Freie Universität Berlin

vorgelegt von
Tasca Noela Santimano

Berlin, 2015

Erst gutachter: Prof. Dr. Onno Oncken
Freie Universität Berlin, GeoForschungsZentrum Potsdam

Zweitgutachter: Prof. Dr. Nina Kukowski
Friedrich Schiller Universität Jena,

Date of defense: January 4th, 2016

“A lot of what [we] do is to try to understand Mother Nature’s mind and her sense of beauty to see how the laws of Physics could be more beautiful. The more you learn about the equations, the more you learn about physics, the more you learn how beautiful it is. That’s the real value. It’s an ornament to the human mind”

-Frank Wilckek

“Imagination is more important than knowledge”

-Albert Einstein

Summary

This thesis addresses the complexity in the patterns of deformation in accretionary wedges based on analogue modelling. A combined approach of 1) statistically assessing results from sand wedges 2) mechanically analyzing fault behavior in the structural evolution of sand wedge and 3) comparing varying wedge geometry and dynamics to theory, are used in an effort to unravel the complexity that develops as the wedge evolves. This thesis comprises of three manuscripts addressing these three approaches respectively. The experimental database is derived from analysis of 27 analogue sand wedge models where the friction of the basal décollement is varied. The kinematics of the analogue sand wedge is monitored using Particle Image Velocimetry (PIV) that provides detailed information on the displacements in the wedge. The statistical approach (Chi square test, ANOVA test) consists of quantifying the degree of both intrinsic variations in the results of the model and extrinsic variation caused by the varying basal friction. In particular the statistical study shows that intrinsic variability of fault and wedge observables is related to the mechanics and material properties of the wedge. In addition, results show that analogue experiments are reproducible.

The next study presented in this thesis reflects on the faults of the wedge. Fault activity, in particular fault formation, reactivation and underthrusting are described. The observations are explained mechanically in relation to the fault geometry and the changing frictional properties along the fault plane. It is also demonstrated that fault activity governs the shape, activity and eventual zonation of the wedge. Additionally, a comparison between two theories 1) Critical taper theory and the 2) Minimum work theory is performed to recognize which theory best represents the deformation in accretionary wedges. The critical taper theory focuses on the geometry of the wedge and the minimum work theory focuses on the energy in the wedge. It is evident that both theories are applicable, however at different stages of an accretionary cycle. Overall, the minimum work theory determines the path of deformation needed to reach that geometry determined by the critical taper theory.

Research to explore the role of ductile behavior in the wedge is also initiated. Preliminary stages of the research include the characterization of a new elasto-plastic viscous material called Carbopol that behaves in a viscous manner after a certain yield strength is overcome i.e. Herschel Bulkley fluid. A rheological study tests the effect of concentration of three different types of commercial Carbopol products. Besides this research, the monitoring of forces in analogue models is also attempted with a new setup. The combination of high resolution force recordings and visual PIV data provides an insightful view into the dynamics of the model.

Zusammenfassung

In der vorliegenden Arbeit wird die Komplexität von Deformationsmustern in der Entwicklung von Akkretionskeilen durch folgende Ansätze aufgezeigt: (1) Die statistische Auswertung von Ergebnissen von Analog-Sandkeilen, (2) Erklärungen des mechanischen Verhaltens von Störungen, der wichtigsten Strukturelemente solcher Keile, und (3) der Vergleich von Keilgeometrie und Keildynamik mit der zugrundeliegenden Theorie. Der Experimentaufbau umfasst eine systematische Studie von 27 Analogmodellen von Sandkeilen, in denen die Reibung der basalen Abscherung variiert wird. Die zeitliche Entwicklung dieser Analogsandkeile wird mithilfe der Particle Image Velocimetry (PIV) aufgezeichnet, die detaillierte Information hinsichtlich von Versätzen innerhalb eines Keils ermöglicht. Die statistischen Ansätze (Chi-Quadrat-Test, ANOVA-Test) beinhalten die Quantifizierung der intrinsischen Variation der Modellierungsergebnisse sowie der extrinsischen Variation, die durch die Variation der basalen Reibung verursacht wird. Die statistische Auswertung zeigt insbesondere, dass die intrinsische Variabilität von beobachtbaren Größen der Störungen und Keile von der Mechanik und den Materialeigenschaften der Keile abhängen. Des Weiteren belegen die Ergebnisse, dass Analogexperimente reproduzierbar sind.

Die folgende Studie in der Arbeit richtet sich auf die Störungen, insbesondere die Bildung, Reaktivierung und Unterschiebung, innerhalb von Keilen. Beobachtungen werden hinsichtlich der Mechanik von Störungsgeometrie und veränderter Reibungseigenschaften einer Störungsebene erklärt. Es wird ebenfalls gezeigt, dass Form, Aktivität und mögliche Zonierungen von Keilen durch die Störungsaktivität bestimmt werden. Des Weiteren zeigt der Vergleich zweier Theorien, der Theorie der kritischen Keile und der Theorie der minimalen Arbeit, welche der beiden Theorien die Deformation in Akkretionskeilen am besten beschreibt. Die Theorie der kritischen Keile stützt sich auf die Keilgeometrie während die Theorie der minimalen Arbeit die Kräftebilanz in einem Keil betrachtet. Beide Theorien sind von Bedeutung, jedoch in verschiedenen Stadien der Keilentwicklung. Generell wird durch die Theorie der minimalen Arbeit der Deformationspfad beschrieben, der zur Erlangung einer bestimmten Keilgeometrie führt.

Die Arbeit zeigt auch Wege auf, die die Rolle der initialen duktilen Deformation betreffen. Vorläufige Stadien dieser Forschung beinhalten die Charakterisierung von neuen elasto-plastischen, viskosen Materialien, wie Carbopohl, das nach Erreichen der Versagensgrenze spröde deformiert. Dahingehend überprüft eine rheologische Studie den Einfluss die Konzentration von drei kommerziell erhältlichen Carbopol-Produkten. Darüberhinaus wird durch einen neuen Experimentaufbau die Aufzeichnung von Kräften in Analogexperimenten untersucht. Die Kombination von hochauflösender Aufzeichnung von Kräften und visueller PIV-Daten ermöglicht neue Betrachtungen der Dynamik von Modellen.

Table of Content

Summary i

Zusammenfassung iii

Chapter 1- Introduction 1

Chapter 2- 9

Intrinsic versus extrinsic variability of analogue sand-box experiments -insights from statistical analysis of repeated accretionary sand wedge experiments

2.1) Introduction 10
2.2) Methodology 11
2.2.1) Experimental setup and analysis procedure 11
2.2.2) Statistical analysis 20
2.2.2.1) Chi-square test (χ^2) 20
2.2.2.2) ANOVA test 20
2.3) Experimental observations 26
2.4) Statistical results 27
2.5) Discussion 31
2.5.1) Intrinsic variability in fault observables 31
2.5.1.1) Low variability of fault dip 31
2.5.1.2) Variability in fault lifetime and spacing 32
2.5.1.3) Influence of thickness on granular basal décollement 33
2.5.2) Mechanical causes for the difference between setups 33
2.5.2.1) Relationship between basal friction and fault lifetime and spacing 34
2.5.2.2) Increase in fault dip due to decreasing basal friction 34
2.5.2.3) Relating interpretations of the statistical analysis to geodynamic natural observations 35
2.6) Conclusion 36
Appendix A2.1) Derivation of material properties using a ring-shear tester 41
Appendix A2.2) Statistical tests 47

Chapter 3- 51

Systematics in the behavior of faults in accretionary wedges and their effects on wedge geometry

3.1) Introduction 52
3.2) Methodology 52
3.3) Fault behavior 53
3.4) Discussion 55
3.4.1) Fault orientation 55
3.4.2) Fault activity 56
3.4.3) Effect of fault behavior on wedge topography 60
3.5) Conclusion and implications 62

Chapter 4- 67

Smart or beautiful? Accretionary wedge evolution seen as a competition between minimum work and critical taper

4.1) Introduction 68
4.2) Wedge evolution in the analogue sand wedge and self-similar wedge (SSW) 70
4.3) Comparison of geometry and work between the two wedges 72
4.4) Implications for the analysis of accretionary wedges 73
4.5) Towards understanding natural wedges 74
4.6) Conclusion 75
Appendix A 4.1) Experimental design and analysis 79
Appendix A 4.2) Analogue accretionary wedges with different basal frictions 83

Chapter 5- Further developments 89

5.1) Rheology of a new analogue material to study ductile deformation 89
5.1.1) Introduction 89
5.1.2) Material properties of Carbopol 89
5.1.3) Rheology of Carbopol 90
5.2) Force sensors in analogue experiments 92
5.2.1) Introduction 92
5.2.2) Experimental design 92
5.2.3) Compressional wedge experiments 93
5.2.4) Data produced 93
5.2.4.1) PIV data 93
5.2.4.2) Force data 94

Conclusion 99

Acknowledgements 101

Declaration 103

Curriculum Vitae 104

Chapter 1- Introduction

Orogenic belts and the formation of their wedge shape have been of interest to geologists for more than a century. Particularly, the mechanics behind the accommodation of matter from the Earth surface, whether due to the collision of continental plates or the subduction of oceanic plate under a continental plate, has always been of great focus in geological research. The first physical models built by compressing layers of sediments provided initial observations and understanding of mountain building processes (Hall, 1815). In the late 1970s and 1980s, through natural observations and analytical analysis the key elements for the formation of a wedge shape were recognized. It was realized that a large amount of shortening along a weak basal décollement produced a wedge shape with thrust faults dipping towards the hinterland (Elliott, 1976; Chapple, 1978). In the 1980s, the theory of the Critical Taper was introduced to understand the physics behind the geometry of the wedge shape. The analytical Critical Taper model (Davis et al., 1983) identified that it is the basal friction, the internal friction and the internal kinematics that determines the taper of the wedge. Through many more analogue and numerical models our understanding of natural wedges has greatly advanced. In combination with technological advances like the laser scanner and Particle Image Velocimetry (PIV) (Graveleau et al., 2012 and references within) we are able to make better and highly resolved observations of the deformation process. Through the advances in analogue and numerical models we have a better understanding of the effect of material properties on the wedge, the effect of varying décollement properties (i.e. décollement dip and friction) and also the effect of external surface processes. Material properties particularly the packing of grains makes a difference in the frictional properties and consequently affects the deformation of the wedge (Lohrmann et al., 2003; Panien et al., 2006, Gomes, 2013, Maillot, 2013). Wedge topography and taper are directly related to the friction of the basal décollement. A decrease in basal friction produces a wedge with a shallow taper and vice versa (refer to Buiter, 2012 for a comprehensive review of studies). Additionally, surface processes like erosion affects the wedge taper causing a profound response and change in deformation path to regain the taper (refer to Buiter, 2012 for a comprehensive review of studies).

The next step of research to better understand natural wedges

The critical taper theory is a model that is simplified to explain the shape of the wedge. As a result it does not take into account the failure of the material, faults, any zones of weaknesses or heterogeneity due to faults or that could arise as the wedge develops (Woodward, 1987; Wang and Hu, 2006; Simpson, 2011). As mentioned by Buiter (2012) the critical taper model presents a static view of the wedge. Although we understand very well the effect of different parameters on the wedge, we also have to understand the interplay between parameters over time. Therefore, research should be directed towards addressing the complexity in deformation patterns that arises over various temporal scales. To address the changes that the wedge develops, advances have been made with models focusing on the forces in the system. The minimum work models (Mitra and Boyer, 1986; Hardy et al., 1998; Masek et al., 1998; DelCastello and Cooke, 2007; Cooke et al., 2014) analyzes the interplay of forces especially along fault planes and shows that deformation proceeds along the path of least work. The

limit analysis approach based on the maximum strength theorem is used to predict the timing of new thrust faults (Cubas et al., 2008) and determine the interplay of the décollement and newly accreted fault and its relation to friction and erosion (Mary et al, 2013).

Overarching goal of the thesis

An immense interest in the deformation of orogenic wedge is due to the occurrences of earthquakes especially recently. In the last two decades there has been increasing number of earthquakes. Moreover there were "unexpected" occurrences in continental interiors like the 2008 Wenchuan earthquake. This reveals that our understanding of deformation in mountain building processes especially on variable timescales is much needed. To study and explain the complexity in wedge evolution would require decades and entire careers of research. Nonetheless, the main idea and goal of this thesis is to unravel deformation patterns in accretionary wedges which occur on different timescales between seismic cycle and mountain building. These patterns over time are not accessible with human monitoring techniques and are usually described as "complex" or "random" in models. To address this complexity in wedges, I systematically look at a spectrum of deformation at different time scales from zero order: wedge growth, 1st order: accretionary cycles, fault formation and 3rd order: reactivation of faults. To endeavor into a more complete spectrum of fault behaviors analogue models are an ideal tool that allows us to observe deformation along the entire lifetime of the wedge.

Experimental design

The experimental design created to address the curiosity mentioned above consists of the temporal observation of simple analogue sand wedge models. Analogue models allow for a systematic and controlled study that is especially important to study the effects of one or more parameters. The analogue sand wedges created for this study were repeated in a controlled setup and environment (details of the setup are mentioned in Chapter 2). A total of 27 sand wedge were created where the magnitude and thickness of the basal friction was varied using varying sizes of glass beads. Basal friction was chosen to vary, since it is an important parameter that influences the shape and dynamics of a wedge (Davis et al., 1983). To understand the most complete temporal evolution of accretionary wedges, model wedges were created with sufficient shortening (160cm of convergence) to capture as many accretionary cycles and to produce a mature wedge. High temporal and spatial resolution data produced from the Particle Image Velocimetry (PIV) system allowed for a quantitative analysis of the development of the wedge. In addition and unlike numerical models, since the analogue models are physical objects, deformation consist of an inherited variability (Cubas et al., 2010). This variability is also used as a tool to understand the predictable and unpredictable behavior of wedges.

To address some areas of complex behavior in wedge evolution, I present three specific questions

1) Are analogue experiments repeatable? What is the intrinsic variability (background noise) of analogue experiments? How can this intrinsic variability be used to explain the mechanics of the wedge?

2) How does the behavior of faults vary in wedges with varying basal frictions? How does the transient change in fault kinematics affect the geometry of the wedge?
3) The Critical taper theory (Davis et al., 1983, Dahlen, 1984; Dahlen, 1990) focuses on the geometry of the wedge, however does not take into account strain localization. The Minimum work theory (Mitra and Boyer, 1986; Hardy et al., 1998; Masek et al., 1998) focuses on the balancing of forces. How does the temporal evolution of the wedge relate to both theories?

A statistical approach is used to quantify and evaluate intrinsic variability the "background noise" and the extrinsic "signal" in the analogue wedges. The data is organized based on fault (fault lifetime, spacing, dip and backthrust dip) and wedge observables (wedge height, length and slope). The intrinsic variability for each observable is quantified using the statistical analysis tool Chi square test (also used in Cubas et al., 2010) and the ANOVA test. Focus is then placed on the "signal", the formation of faults and how they relate to the accretionary cycle (1^{st} order) and wedge evolution (zero order). Here, fault activity including fault reactivation (3^{rd} order) and fault geometry are closely observed to understand how they affect the growth of the wedge. Lastly, I mechanically analyze part of the multispectral deformation patterns by relating them to two theoretical concepts. They are the Critical taper theory (Davis et al., 1983, Dahlen, 1984; Dahlen, 1990) and the Minimum work theory (Mitra and Boyer, 1986; Hardy et al., 1998; Masek et al., 1998). The aim of this study is to better understand which theory best explains the evolution of an accretionary wedge.

Furthermore, initial research on 1) the effects of elasticity and viscosity and 2) the monitoring of forces in analogue models is introduced. To identify a suitable analogue material to simulate brittle-ductile deformation in wedges, the rheology of a Herschel Bulkley material called Carbopol is studied. This rheological study was part of a larger benchmark study between four international laboratories. In addition, the monitoring of forces in analogue models is an important advancement as it provides a view into the dynamics during model development. The creation of a setup up that measures force at a high temporal resolution provides insight into the seismic cycle during the evolution of an analogue model that can be correlated to the visual observation of strain from the PIV system.

Terminology

The terminology presented here is mainly to clarify the meaning of terms used in the thesis since they may vary from terms used in other literature.

Reproducibility- Reproducibility is the ability to reproduce the experimental results with a give precision independently by the same or another experimentalist.

Repeatability- Repeatability is the variation in measurement of experiments that were reproduced by the same experimentalist, setup and laboratory conditions. Repeatability is also known as test-retest repeatability.

Static coefficient of friction- The coefficient of friction that has to be overcome, to initially deform a homogenous mass of brittle material with no prior fabric, planes of weakness or faults.

Static reactivation coefficient of friction- The coefficient of friction that has to be overcome, to cause slip on a pre-existing fault or zone of weakness i.e. to reactivate the fault. This coefficient of friction is lower than the static coefficient of friction

Kinetic coefficient of friction – The coefficient of friction at which the fault continues to slide. In other studies this is called kinetic or reactivated coefficient of friction. All coefficients of friction are measured using a Schulze Ring Shear Tester (A.2.1)

Storage modulus (G') – is a measure of the deformation energy stored by the sample during the shear process. Elastic behavior is represented by G' (Mezger, 2006)

Loss modulus (G") – is a measure of the deformation energy used dissipated during the shear process and therefore lost. Samples that lose the energy show irreversible deformation behavior. Viscous behavior is represented by G". For gel like characteristics G' > G" and for liquid characteristics or viscous behavior G' < G" (Mezger, 2006).

Linear viscoelastic (LVE) range– Both the G' and G" values are constant and show a plateau regardless of amplitude values. This occurs usually at low amplitude values (Mezger, 2006).

Yield point or yield stress– Shear stress value at which G' and G" values deviate from the LVE plateau. At this point there is a change in the behavior of the sample usually related to a change in the internal structure of the sample (Mezger, 2006).

References

Buiter, S.J.H., 2012. A review of brittle compressional wedge models. Tectonophysics 530 - 531, 1-17. doi:10.1016/j.tecto.2011.12.018

Chapple, W.M., 1978. Mechanics of thin-skinned fold-and thrust belts. Bulletin of Geological Society of America 89, 1189-1198.

Cooke, M.L., Murphy, S., 2004, Assessing the work budget and efficiency of fault systems using mechanical models: Journal of Geophysical Research. Solid Earth, v.109, doi: 10.1029/2004JB002968

Cooke, M.L., Madden, E. H., 2014, Is the Earth lazy? A review of work minimization in fault evolution: Journal of Structural Geology, v. 66, p. 334-346.

Cubas, N., Maillot, B., Barnes, C., 2013. Inverse method applied to a sand wedge: Estimation of friction parameters and uncertainty analysis. Journal of Structural Geology 55, 101-113

Cubas, N., Maillot, B., Barnes, C., 2010. Statistical analysis of an experimental compressional sand wedge. Journal of Structural Geology 32, 818-831.

Cubas, N., Leroy, Y.M., Maillot, B., 2008. Prediction of thrusting sequences in accretionary wedges. Journal of Geophysical Research 113, B12412, doi:10.1029/2008JB005717.

Dahlen, F.A., 1990. Critical Taper model of fold-and-thrust belts and accretionary wedges. Annual Review of Earth and Planetary Science 18, 55-99.

Dahlen, F.A., 1984. Noncohesive Critical Coulomb Wedges: An Exact Solution. Journal of Geophysical Research 89 (B12), 10,125-10,133.

Davis, D., Suppe, J., Dahlen, F.A., 1983. Mechanics of Fold and Thrust Belts and Accretionary Wedges. Journal of Geophysical Research 88 (B2), 1153-1172.

Del Castello, M., Cooke, M.L., 2007, Underthrusting-accretion cycle: Work budget as revealed by the boundary element method. Journal of Geophysical Research, v. 112, doi: 10.1029/2007JB004997

Elliott, D., 1976. The motion of thrusts sheets. Journal of geophysical Research 81, no. 5. 949-963.

Gomes, C. J. S., 2013. Investigating new materials in the context of analog-physical models. Journal of Structural Geology 46, 158-266.

Graveleau, F., Malavieille, J., Dominguez, S., 2012. Experimental modelling of orogenic wedges: A review. Tectonophysics 538, 1-66.

Hall, J., 1815. On the Vertical Position and Convolutions of certain Strata and their relation with Granite. Transactions of the Royal Society of Edinburgh 7, 79-108.

Hardy, S., Duncan, C., Masek, J., Brown, D., 1998, Minimum work, fault activity and the growth of critical wedges in fold and thrust belts: Basin Research, v. 10, p. 365-373.

Lohrmann, J., Kukowski, N., Adam, J., Oncken, O., 2003. The impact of analogue material properties on the geometry, kinematics, and dynamics of convergent sand wedges. Journal of Structural Geology 25, 1691-1711.

Maillot, B., Barnes, C., Mengus, J.-M, and Daniel, J.-M., 2007. Constraints on friction coefficients by an inverse analysis of sand box thrust dips. Journal of Structural Geology 29, 117-128.

Maillot, B., 2013. A sedimentation device to produce uniform sand packs. Tectonophysics 593, 85-94.

Mary, B. C. L., Maillot, B., Leroy, Y. M., 2013. Predicting orogenic wedge styles as a function of analogue erosion law and material softening. Geochemistry Geophysics Geosystems 14 (10). 4523-4543

Masek, J.G., Duncan, C.C., 1998, Minimum-work mountain building: Journal of Geophysical Research, v. 103, no. B1, p. 907-917.

Mezger, T.G., 2006. The Rheology Handbook. 2nd revised edition. Vincentz Network, Hannover.

Mitra, G. Boyer, S.E., 1986. Energy balance and deformation mechanisms of duplexes: Journal of Structural Geology, v. 8, p. 291-304.

Simpson, G., 2011. Mechanics of non-critical fold-thrust belts based on finite element models. Tectonophysics 499, 142 -155.

Woodward, N.B., 1987. Geological applicability of critical-wedge thrust-belt models. Geological Society of America Bulletin 99, 827-832.

Chapter 2

Intrinsic versus extrinsic variability of analogue sand-box experiments- insights from statistical analysis of repeated accretionary sand wedge experiments.

Abstract

Analogue models are not perfectly reproducible even under controlled boundary conditions which make their interpretation and application not always straight forward. As any scientific experiment they include some random component which can be influenced both by intrinsic (inherent processes) and extrinsic (boundary conditions, material properties) sources. In order to help in the assessment of analogue model results, the intrinsic versus extrinsic variability of results from "sandbox" models of accretionary wedges that were repeated in a controlled environment are quantified. The extrinsic source of variability, i.e. the parameter varied is the nature of the décollement (material, friction and thickness). Experiment observables include geometric properties of the faults (lifetime, spacing, dip) as well as wedge geometry (height, slope, length).

For each variable, the coefficient of variance (CV) is calculated and the variability is quantified as a symmetric distribution (Normal, Laplacian) or asymmetric distribution (Gamma) using a Chi squared test (χ^2). Observables like fault dip/ back thrust dip (CV = 0.6-0.7/ 0.2 – 0.6) are less variable and decrease in magnitude with decreasing basal friction. Variables that are time dependent like fault lifetime (CV= 0.19- 0.56) and fault spacing (CV=0.12 – 0.36) have a higher CV consequently affecting the variability of wedge slope (CV= 0.12-0.33). These observables also increase in magnitude with increasing basal friction. As the mechanical complexity of the evolving wedge increases over time so does the CV and asymmetry of the distribution. In addition the repeatability of experiments is confirmed using an ANOVA test. Through the statistical analysis of results from repeated experiments a tool is presented to quantify variability and an alternative method to gaining better insights into the dynamic mechanics of deformation in analogue sand wedges.

This study has been peer-reviewed and published as follows-
Santimano, T., Rosenau, M., Oncken, O., 2015, Intrinsic versus extrinsic variability of analogue sand-box experiments- Insights from statistical analysis of repeated accretionary sand wedge experiments: Journal of Structural Geology, v. 75, p. 80-100

2.1) Introduction

Results from experiments can vary because of extrinsic and intrinsic controls. Generally, extrinsic controls are varied systematically in order to test their influence on a system in so called parameter studies. This approach is well suited to identify control factors which have a strong influence on experimental outcomes. However, if the influence is smaller it becomes difficult to verify that the resulting variability is attributable to extrinsic controls and not intrinsic variability. Experiments including parameter studies with so called analogue models, i.e. physical lab scale models made of weak rock analogue material (e.g. loose sand, clay, wax) have been created since the early nineteenth century pioneering the work of Sir Hall (Hall, 1815, see Graveleau et al., 2012 for a comprehensive historical review) to understand geological observations (e.g. the structure of a fold-and-thrust belt) by means of forward simulation of the underlying geodynamic processes. In contrast to numerical or analytical models which will always generate the same result with insignificant variability from a given starting configuration, experiments with analogue models never give exactly the same result as a consequence of inherent variability. This might be viewed as a handicap of the analogue modelling approach but also vice versa as a chance to simulate process variability in nature. The fact that variability is a matter of interest in scientific studies stems from the rising awareness for our limited view on geodynamic processes with single observations being only part of a spectrum of possible observational outcomes. If the source of variability is similar in the model as in nature, it is argued that any physically simulated variability is preferred over statistically implemented noise from which variability typically arises in numerical models (e.g. Rosenau et al., 2010).

Several sources of variability exist in nature (and consequently in the analogue model as well as in the natural prototype) both extrinsic, i.e. in the boundary conditions or material properties, and intrinsic due to the inherently changing physical properties of the system as it evolves. In most parameter studies extrinsic variability is the focus, i.e. the change in experimental outcomes as a consequence of changes in the controlled boundary conditions or material properties. However, if intrinsic variability is unknown in such experiments, differences in the outcomes are potentially misattributed to large parts of the extrinsic controls. Only if intrinsic variability is significantly smaller than extrinsic variability, meaningful inferences from analogue models can be drawn. This indicates the importance of quantifying intrinsic vs. extrinsic variability in order to get an idea for the precision of analogue model results. However, only few studies have researched this issue so far (Cubas et al, 2010).

Benchmark study by Schreurs et al. (2006) is an example of studying extrinsic variability related to boundary conditions. In this benchmark a simple experiment of creating a compressional sand wedge, was performed in six laboratories around the world without much prescription of the setup. Benchmark experiments showed consistently an overall cyclic deformation pattern of the wedge but the detailed observables and in particular the final geometry varied significantly. This difference was attributed to the different setup preparation protocols and physical differences (grain size distribution, density and frictional properties) in materials used. In this case, it was understood that experiments needed to have a strict setup

protocol if they were to be compared. In a follow-up study, materials used were identical, the setup was constrained more heavily and consequently the variability minimized to the true intrinsic variability (Schreurs, pers. Comm.).

Here these findings are built on and intrinsic and extrinsic variability is studied in a series of classical sand wedges with systematically varying basal coefficient of friction (μ_{basal}). Boundary conditions and material properties were fixed and stable to a degree that is typical for analogue models, i.e. the same experimental device and preparation procedures were used and experiments were performed under controlled ambient temperature and air-moisture. A similar approach has been undertaken by Cubas et al. (2010) studying along-strike variation in cross-sections of early thrusts in repeated sand wedge experiments. Here the cross-sections were considered independent observations. In contrast to their approach, variation is analyzed along a single profile across many thrusts evolving during wedge evolution in repeated experiments. By inducing higher strain compared to Cubas et al. (2010) and adding variation of extrinsic parameters (basal friction) therefore this study goes beyond their work in analyzing variability related to intrinsic and extrinsic sources as well as to wedge evolution.
The findings show that the variability in the results are attributed to (1) variability in material properties and (2) the complexity of the evolving mechanics of the wedge. In the study fault dip is related only to the coefficient of friction of the granular material and therefore has a low CV. On the other hand, fault spacing is related to fault lifetime and the criticality of the wedge which may change over time, thus fault lifetime and spacing changes with time and can have a larger CV.

2.2) Methodology

2.2.1) Experimental setup and analysis procedure

The analogue experiments were kept simple and consist of creating convergent accretionary wedges. The experimental set-up (Fig. 2.1a) consists of a box with dimensions 300 cm long, 20 cm wide and has a horizontal base that is made of a rubber conveyor belt (coefficient of friction (μ) ~0.68 against sand, Fig. A2.2) and glass sidewalls (μ ~ 0.15 against sand, Fig. A2.2). In the box, a total thickness of 3 cm layer of granular material (sand, or sand and glass beads- for frictional coefficient see Table 2.1 and Fig. A2.2) is sieved on the conveyor belt for the entire length of the box. Sieving of the granular material produces a homogenous layer (Lohrmann et al., 2003; Maillot, 2013) which is void of any internal preexisting structures or zones of weakness that can be activated during the experiment. Care is taken that the final surface was horizontal and planar within the thickness of the beam of a laser level (ca. 1 mm). To create the wedge the layer of granular material is pushed against a stationary rigid back wall by moving the conveyor belt at a constant velocity of 1mm/s towards and under the back wall. The growth of the wedge is recorded from the side by a digital camera (CCD, 11 MPx, 16 bit) at 1 Hz. Image data are calibrated and cross-correlated for deriving incremental displacement (= velocity) fields by means of Particle Image Velocimetry (PIV) (Adam et al., 2005) (Fig.2.1b, 2). Further processing of the images and vector fields produces binary images (Fig. 2.1c, 2, 3a) and maps of the evolving geometry and displacement of the wedge (Fig. 2.1d, 3b,c) thus monitoring the formation and kinematics of faults (Fig. 2.3c). To

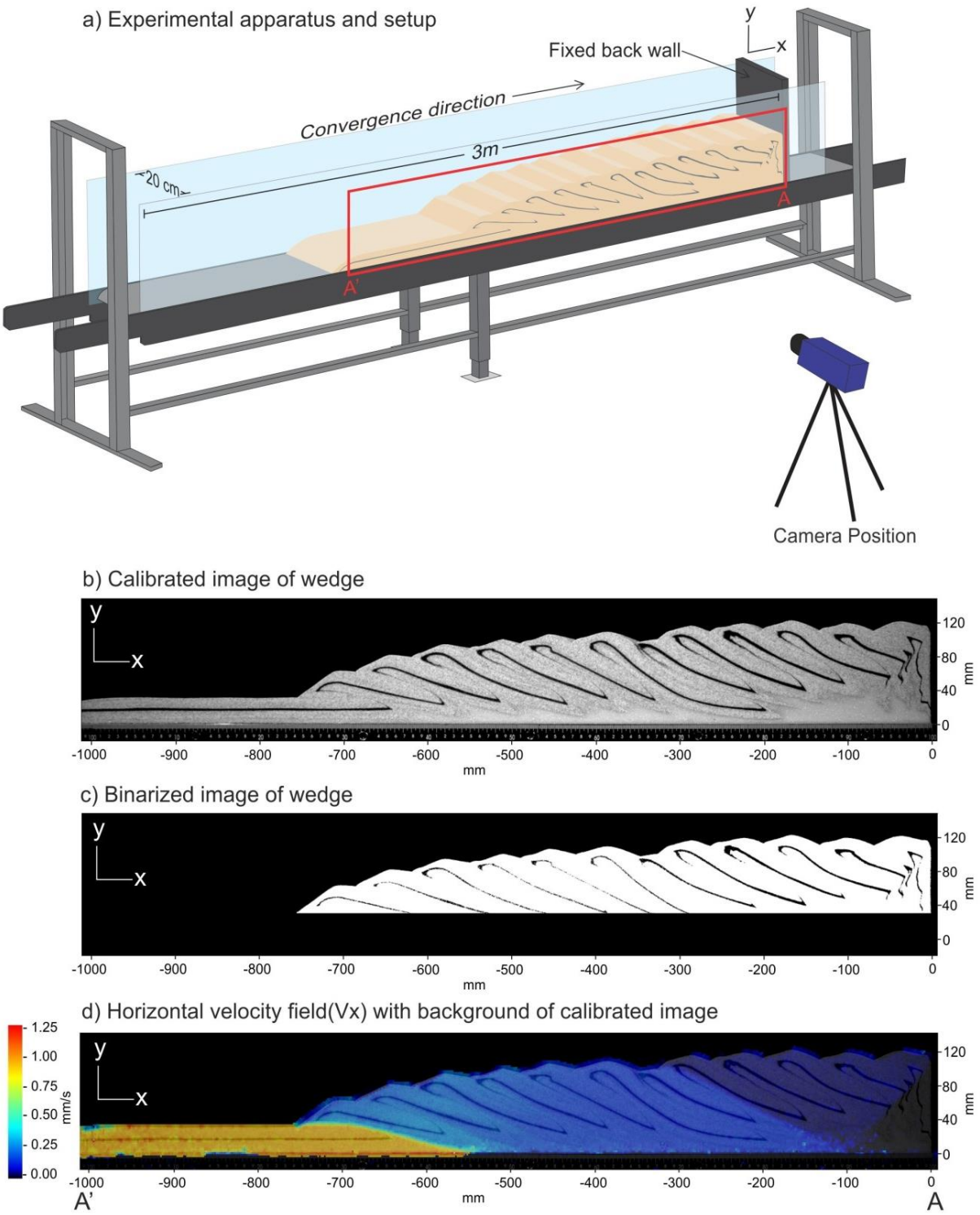

Figure 2.1 – Experimental box for all the experimental setups. Data and processed images obtained from the PIV system include a) calibrated image of the wedge, b) binarized image of the wedge and c) processed images of the wedge showing the horizontal velocity field (V_x) along the wedge. The experiment shown in this figure is from setup 3- sand +0.5cm layer of 300-400μm glass beads.

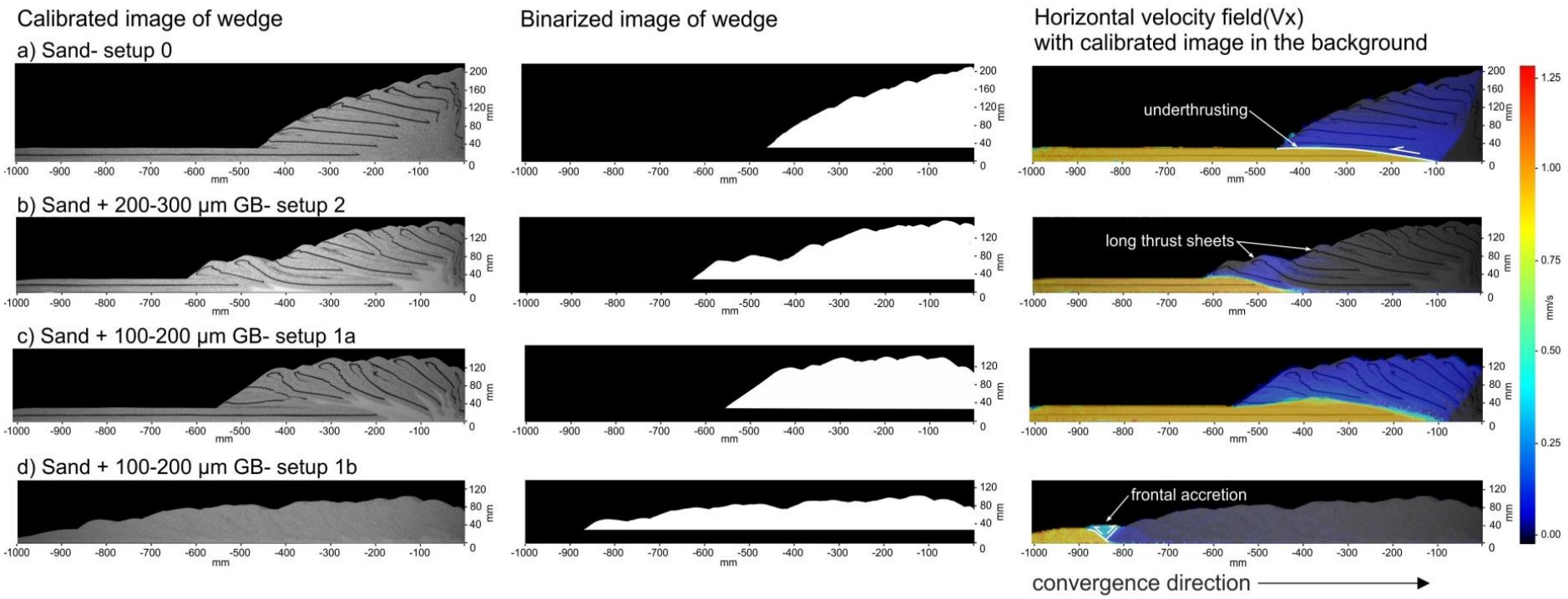

Figure 2.2- Examples of calibrated images, binarized images and processed images of the wedge showing the horizontal velocity field (V_x) for a) sand (setup 0), b) sand +0.5cm layer of 200-300µm glass beads (setup 2), c) sand +0.5cm layer of 100-200µm glass beads (setup 1a) and d) sand +0.2cm layer of 100-200µm glass beads (setup 1b). All images display 160 cm of shortening. The processed images show the difference in deformation style in particular underthrusting in setup 0 and frontal accretion in setup 1.

visualize the evolution of the faults in time as the wedge grows, a horizontal profile (Fig. 2.3b, c) of the velocity field is created in the middle of the granular layer at a height of 1.5 cm from the base. These velocity profiles are then assembled against each other in time and displayed as a deformation map (Fig. 2.3d).

From these deformation maps, fault spacing and lifetime for each accretionary cycle is measured. Specifically, fault lifetime is defined as the time between the formation of two consecutive faults. In this definition, fault life time only includes the time when a fault is the main active structure and does not include the time it is reactivated at a later stage. Fault spacing is the horizontal distance between the last fault and a new fault at the time of localization of the new fault (Fig. 2.3b, d). Kinematically, fault lifetime and fault spacing are related. Fault dip and back thrust dip are measured at the initiation of a new fault. Fault dip has been measured from the PIV images by visually fitting a straight line along the isolines of the velocity field where the gradient is highest (Fig. 2.3b, c).
Binarized images of the wedge are used to derive the height, length and slope of the wedge for every time step automatically. The height and length are measured from the crest (highest point in the wedge) to the base, and from the toe of the wedge to the crest respectively (Fig. 2.3a, 4). This part of the complete wedge is most representative of an active wedge (Lohrmann et al., 2003). Wedge slope is measured as the arc tan (height of the wedge / length of the wedge).

In summary, the observables measured for each experimental setup consist of fault characteristics i.e. fault lifetime, fault spacing (Fig. 2.5), dip of the fault and its respective back thrust as well as wedge geometry i.e. height, length and wedge slope. Estimation errors attached to these observables are 4mm for all lengths, 2 seconds for periods and 2^o for angles.
In this study, the effect of different basal décollement layers is tested on the intrinsic variability of the wedge evolution. From a sand only (no detachment layer) reference experiment (static/kinetic μ_{basal} ~0.68/0.55) basal properties were varied by introducing a weak décollement layer of different thickness (0.2cm vs. 0.5 cm) and made of different sizes of glass beads (100-200 μm, 200-300 μm, 300-400 μm with static/kinetic μ_{basal} increasing with size ~0.47-0.53/0.40-0.43, Appendix 2.1). The five different experimental setups that were realized are as follows:
Setup 0) 3cm layer of sand (Number of experiments (N) = 7, Fig. 2.2a)
Setup 3) 2.5cm layer of sand on 0.5 cm 300-400 μm glass beads (N =5, Fig. 2.1),
Setup 2) 2.5cm layer of sand on 0.5 cm 200-300 glass beads (N = 5, Fig. 2.2b),
Setup 1a) 2.5cm layer of sand on 0.5 cm 100-200 μm glass beads (Setup a) (N = 5, Fig. 2.2c) and
Setup 1b) 2.8cm layer of sand on 0.2 cm 100-200 μm glass beads (Setup b) (N = 5, Fig. 2.2d).
Each experiment is repeated up to 7 times for a total of 27 experiments. The internal coefficient of friction ($\mu_{internal}$) for all granular material used in this study is measured in the Schulze Ring shear tester (Schulze, 1994). Table 2.1 displays the static friction for the first or primary failure or fault, reactivation static friction for the reactivation of the fault as well as the kinetic friction.

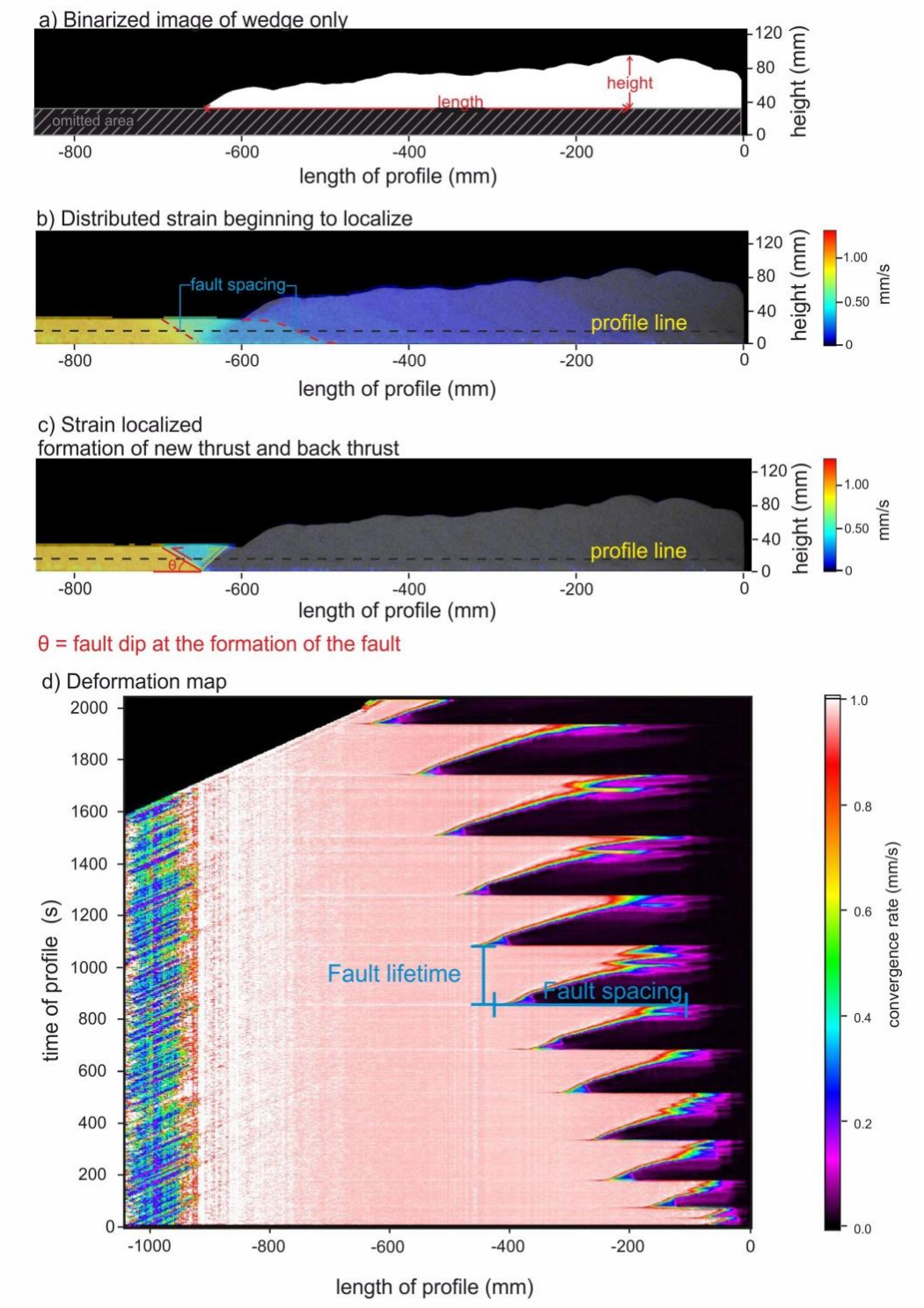

Figure 2.3 – Method of how the observables are measured using the data collected by the PIV cameras a) Binarized images of the wedge are used to calculate the height and length of the wedge for each time step. The incoming layer is not included in the length or height of the wedge. b) Fault spacing is measured as the horizontal distance, along the profile line, between two consecutive faults, when the former fault is at the end of its activity as a first order fault and a new fault is formed. The velocity along the profile line for each time step is plotted in d. The fault spacing is accurately measured from this plot. c) Fault dip and back

thrust dip are measured after strain is completely localized and at the initiation of a new fault plane and back thrust plane. d) Deformation map displaying the velocity for each profile line from c). Therefore the x axis is the length of the wedge and the y axis is the time step. Pink area represents the velocity of the incoming layer. The transition between pink to black in the x axis is the location of the fault plane on the profile line. From this map the fault lifetime and fault spacing can be measured. Fault lifetime is the time (or number of time steps) the fault is active as a first order structure.

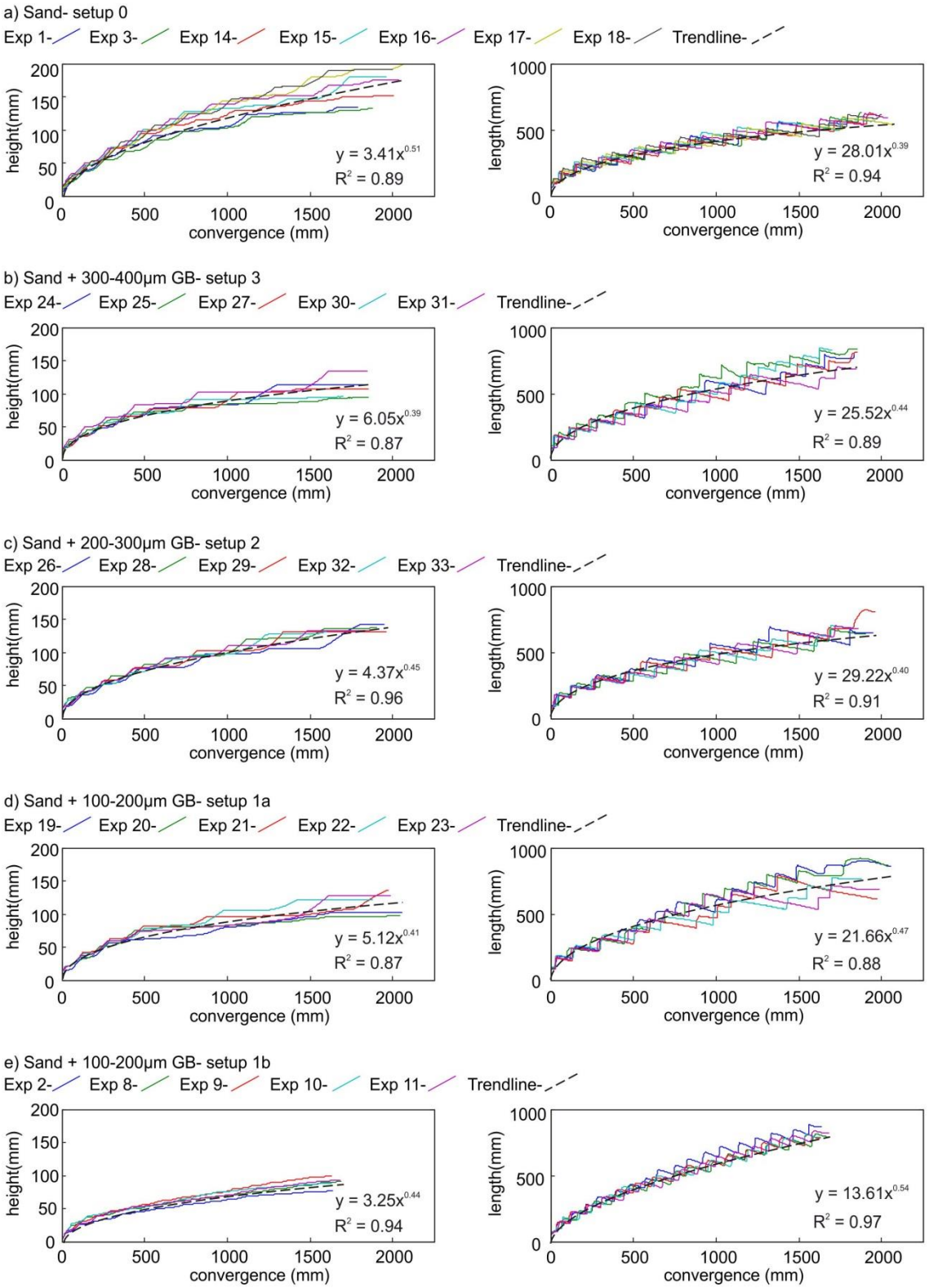

Figure 2.4 – Wedge height and length for all experiments with a) sand (setup 0), b) sand +0.5cm layer of 300-400µm glass beads (setup 3), c) sand +0.5cm layer of 200-300µm glass beads (setup 2), d) sand +0.5cm layer of 100-200µm glass beads (setup 1a) and e) sand +0.2cm layer of 100-200µm glass beads (setup 1b). Dashed black line represents the power law trendline for both height and length of the wedge.

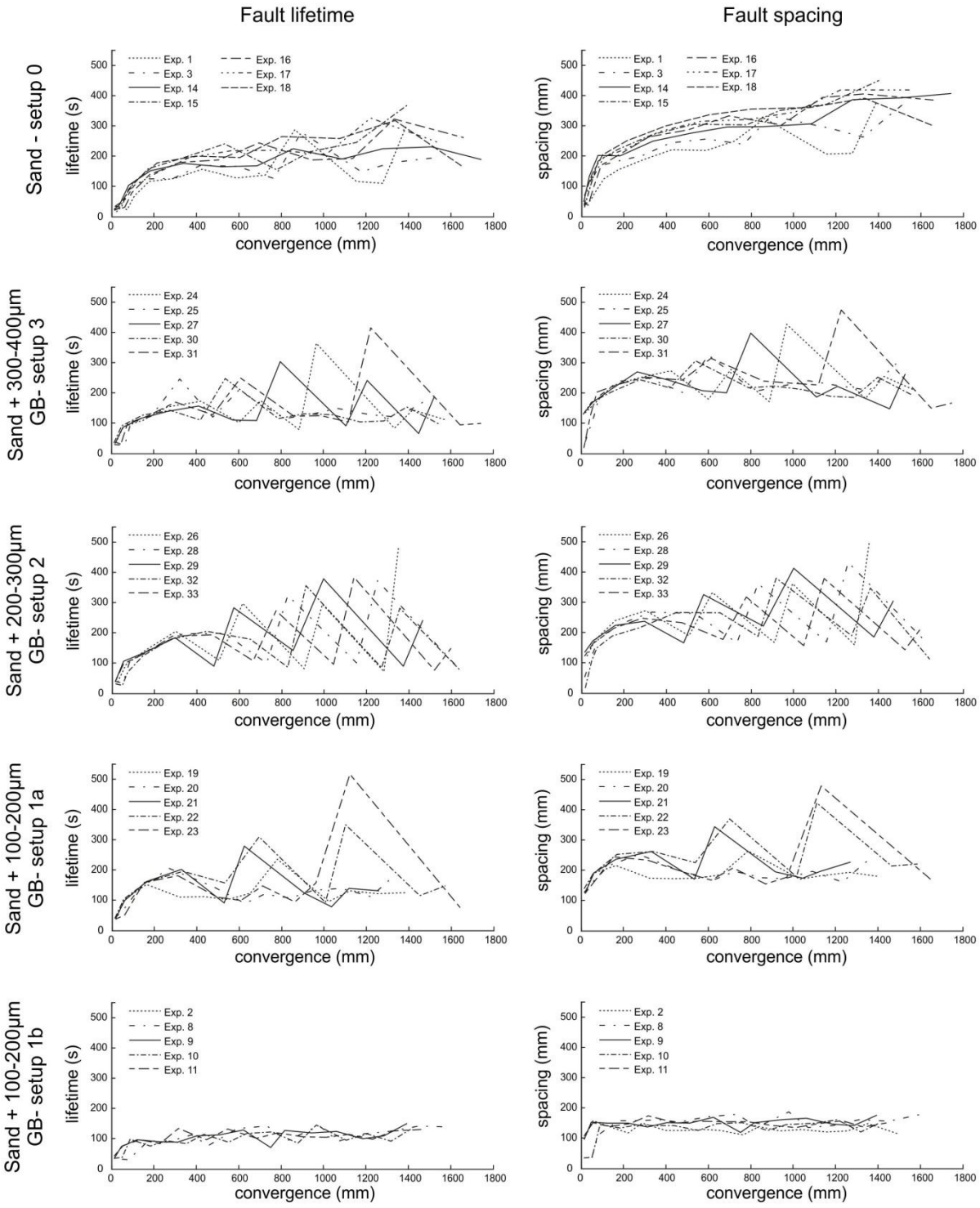

Figure 2.5- Fault lifetime and fault spacing for all experiments with a) sand (setup 0), b) sand +300-400µm glass beads (setup 3) , c) sand +200-300µm glass beads (setup 2), d) sand +100-200µm glass beads (setup1a), e) sand +100-200µm glass beads (setup 1b). b) c) and d) show the occurrence of long lived and widely spaced faults followed by short lived and closely spaced faults, thus producing a zig-zag trend.

Material	Type	Density (g/cm^3)	Grain size (μm)	Static friction	Standard deviation	Static reactivation friction	Standard deviation	Kinetic friction	Standard deviation
Glass beads	Internal	1.59	100-200	0.47	0.03	0.46	0.01	0.40	0.02
Glass beads	Internal	1.60	200-300	0.50	0.04	0.47	0.02	0.42	0.02
Glass beads	Internal	1.64	300-400	0.53	0.04	0.51	0.02	0.43	0.01
Sand	Internal	1.72	> 630	0.68	0.04	0.63	0.02	0.55	0.01
Sand on rubber conveyor belt	Basal			0.62	0.05	0.60	0.02	0.56	0.02
Sand on glass	Basal			0.15	0.09	0.12	0.07	0.12	0.06

Table 2.1 – Material physical properties for the grains used in the experiments include grain size, density, static friction, static reactivation friction and kinetic friction. The coefficients of friction for all materials were measured in a Ring-shear tester and the data can be found in Fig. A2.2

2.2.2) Statistical analysis

The reason to conduct a statistical analysis on a large data base from repeated experiments is threefold: First, to quantify intrinsic variability in the experiments, second, to detect trends which would be statistically irrelevant and therefore go unnoticed in a small number database or because they lay close to/within the error bars and thirdly, to quantify the repeatability of the measurements in experiments within identical setups. All the data for each observable (fault lifetime, fault spacing, fault dip, back thrust dip and wedge slope) of each setup is grouped into one population. Hence five populations is created for each setup and a total of 25 populations (Table 2.2). For each population the basic statistical values i.e. mean, standard deviation and coefficient of variation (CV) were calculated (Table 2.2) before more advanced statistical treatment followed.

2.2.2.1) Chi-square test (χ^2)

As a way to compare data populations beyond the mean and standard variation, the probability density function (pdf) is calculated for each population and compared to theoretical distributions namely the Normal, Gamma and Laplacian distributions (Fig 2.6). To quantitatively determine which of the three distributions fit the best to each population, a Chi square test (χ^2**)** is implemented (Table 2.2). The χ^2 is calculated using the difference between the observed values from experiments and the theoretical value based on the distribution type. The χ^2 is calculated for the observables fault lifetime, fault spacing, fault dip and wedge slope for all setups according to Cubas et al., 2010- Appendix A2.1. More information about the theory of the χ^2 test and the probability distributions used in this paper are available in Appendix A2.2.

In general, normal distributions characterize natural data symmetrically distributed around a mean. Laplacian distributions characterize symmetrically distributed data with a very narrow peak (mode), i.e. those with low variability (low CV). However, it allows values to be further away from the median value at the tails (Cubas et al., 2010). In contrast the Gamma distribution characterizes asymmetric distributions of larger variability. Importantly, symmetric vs. asymmetric distributions are interpreted here in terms of observables that don't vary much vs. observable that are variable especially over time. For example, a periodic process over time characterized by a single frequency and size plus some scatter or noise generates a symmetric distribution while a more complex process characterized by self-similar growing frequency and size generates an asymmetric distribution.

2.2.2.2) ANOVA test

In addition, to detect subtle differences amongst similar populations in the large database, the analysis of variance test (ANOVA) is employed for each population. The ANOVA test primarily analyses the statistical variance within a population. Specifically, since a population is made up of measurements from different experiments of the same setup, the test analyses variance between the different experiments and within the experiments. In this manner the test determines whether all the measurements from the different experiments can be classified as originating from undistinguishable experiments or sources. The test therefore allows, to detect

statistically relevant differences between experiments that would otherwise (e.g. by the classical standard deviation criterion) be unnoticed. This particular test is chosen by examining the population in particular 1) the extent of the intrinsic variability within the population 2) if the distribution of the population is close to normal and 3) the independence of the data in a population (McKillup & Dyar, 2010). In this study the ANOVA test is used for each observable of each set-up 1) to analyze the variation between experiments in each setup and determine repeatability of the data and 2) analyze the variation between different setups to determine if any difference due to basal friction exists. For this test the significance level is set at 5% (Fisher, 1954). Therefore, with a p value more than 5%, the null hypothesis which states that there is no difference between two or more experiments is accepted. The one – way ANOVA test is used since there is only one parameter- μ_{basal} that is changing. This statistical test can be easily computed using statistical softwares or in Matlab or Excel using predefined functions. More details on the ANOVA test are included in Appendix 2.2.

As part of the ANOVA test the coefficient of determination (R^2) is also calculated. R^2 is a quantitative value of how much of the variance in a population is explained due to repeated experiments in contrast to intrinsic variability within experiments. A large R^2 value indicates that the variation is due to the experimental setup or extrinsic sources in contrast to a small R^2 indicating that the variation is within the system (Zar, 2010).

The Fisher (F) value is also calculated and compared to the critical F (F_{crit}) value to determine if the null hypothesis should be rejected. F values lower than the F_{crit} value indicates that the null hypothesis is accepted. F_{crit} can be found on a universal table based on the degrees of freedom and the significance level.

In summary the p value indicates the difference in the variance between experiments and whether the null hypothesis should be accepted or rejected, the F value confirms this conclusion and the R^2 value suggests whether the variance is intrinsic or extrinsic. The disadvantage of the ANOVA test is that if the variance of almost all measurements in a population is consistent but there is one measurement that is an outlier and has a differing variance from the rest of the population, then the p value and F value reject the null hypothesis. On the other hand, since the ANOVA test compares the magnitude of the variance, it only accepts the null hypothesis when the difference between variances of all measurements in a group is not significant.

For the two statistical analyses – χ^2 and ANOVA test, the first 3 faults from all experiments were omitted. The reason for omitting these faults is simply because faults at this stage are small, short lived and not representative of critical wedge evolution (Gutscher et al., 1996). They rather represent the initiation stage of wedge formation characterized by the dominance of uplift over lateral growth. This stage ends when the wedge reaches the critical taper after which wedge growth is quasi-stable. These faults are noticeable in the bottom right corner of the deformation map (Fig. 2.3d) and are clearly different in their size and temporal lifetime. Therefore when analyzing data from analogue experiments it is important to distinguish the parts of the experiment that are representative of the natural process studied.

			Normal model				Gamma model			Laplacian model		
Setup	Population	n	Mean	Standard deviation	$\chi 2$ test	CV	a	b	$\chi 2$ test	Median	Median deviation	$\chi 2$ test
Sand only	Fault Lifetime	58	194	63	0.63	0.33	9.51	20	0.76	188	48	**0.89**
setup 0	Fault Spacing	58	294	76	**0.96**	0.26	14	20	0.95	298	62	0.94
	Fault dip	64	26	1.82	0.66	0.07	217	0.12	0.63	26	1.32	**0.67**
	Back thrust dip	64	45	2.50	N.A.	0.06	390	0.12	N.A.	45	0.92	N.A.
	Wedge slope	1297	17	2.12	0.95	0.12	65	0.26	**0.96**	17	1.68	0.91
Sand + 300-400	Fault Lifetime	48	153	71	N.A.	0.47	6.34	24	0.39	129	50	**0.57**
µm GB	Fault Spacing	48	241	65	0.04	0.27	16	14	0.46	227	43	**0.80**
setup 3	Fault dip	53	26	1.59	**0.22**	0.06	286	0.09	0.20	26	1.14	0.19
	Back thrust dip	52	44	0.82	N.A.	0.02	2883	0.02	N.A.	45	0.41	**0.48**
	Wedge slope	853	12	3.23	0.73	0.26	14	0.85	0.76	12	2.49	**0.78**
Sand +200-300	Fault Lifetime	39	189	106	0.65	0.56	3.47	54	**0.81**	176	85	0.59
µm GB	Fault Spacing	39	258	93	0.86	0.36	8.35	30	**0.91**	237	76	0.78
setup 2	Fault dip	43	28	1.59	0.36	0.06	327	0.09	**0.36**	29	1.41	0.23
	Back thrust dip	43	44	2.16	N.A.	0.05	395	0.11	N.A.	45	1.33	**0.67**
	Wedge slope	896	15	3.04	0.77	0.19	28	0.55	**0.86**	15	2.43	0.77
Sand +100-200	Fault Lifetime	40	155	84	N.A.	0.54	5.33	29	0.17	129	55	**0.40**
µm GB	Fault Spacing	40	217	71	0.11	0.33	12	16	**0.42**	193	48	0.38
setup 1a	Fault dip	45	29	1.79	0.21	0.06	268	0.11	0.21	29	1.13	**0.50**
	Back thrust dip	45	44	2.74	N.A.	0.06	235	0.19	N.A.	45	1.78	**0.08**
	Wedge slope	938	12	4.14	N.A.	0.33	10	1.23	**0.69**	11	3.34	0.41
Sand +100-200	Fault Lifetime	63	106	20	0.91	0.19	26	4.04	**0.92**	105	17	0.87
µm GB	Fault Spacing	63	146	16	0.94	0.12	75	1.94	0.94	148	13	**0.98**
setup 1b	Fault dip	68	30	1.92	**0.30**	0.06	255	0.12	0.28	30	1.66	0.16
	Back thrust dip	67	44	0.80	N.A.	0.02	3019	0.01	N.A.	45	0.31	**0.47**
	Wedge slope	764	9.69	2.54	N.A.	0.26	17	0.56	N.A.	9.10	1.86	**0.78**

Table 2.2 – (previous page) Statistics for all the observables for each experimental setup. For each observable, the number of samples (n), mean, standard deviation, coefficient of variation (CV), median and median deviation are presented. The Chi-square test (χ^2) is calculated between the observed values and the expected values based on the Normal model, the Gamma model and the Laplacian model. The best fit distribution according to the χ^2 test is presented in bold. For the Gamma model the shape parameter (a) and scale parameter (b) are also indicated.

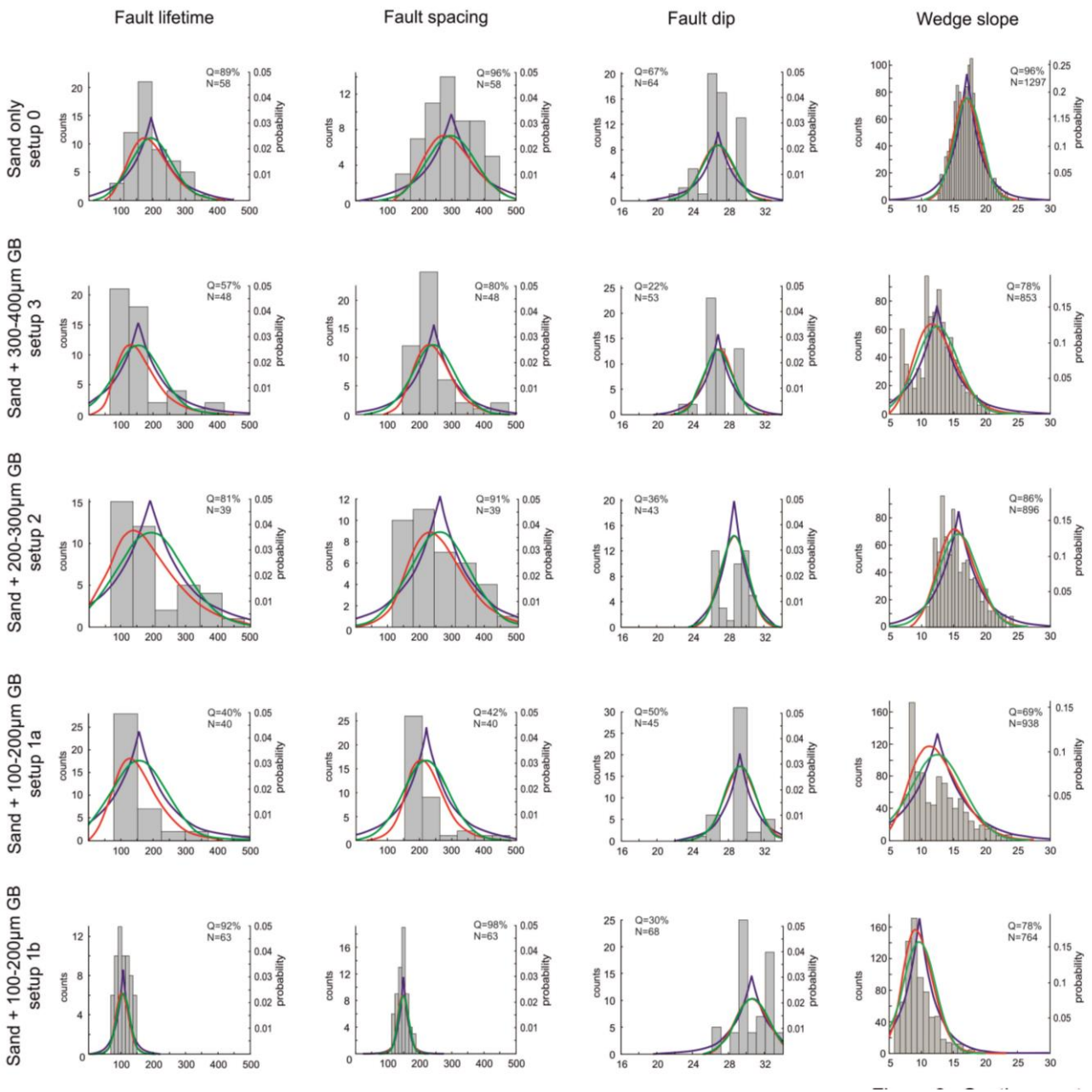
Fault lifetime
Fault spacing
Fault dip
Wedge slope
Sand only
setup 0
Sand + 300-400µm GB
setup 3
Sand + 200-300µm GB
setup 2
Sand + 100-200µm GB
setup 1a
Sand + 100-200µm GB
setup 1b
Q=89%
N=58
Q=96%
N=58
Q=67%
N=64
Q=96%
N=1297
Q=57%
N=48
Q=80%
N=48
Q=22%
N=53
Q=78%
N=853
Q=81%
N=39
Q=91%
N=39
Q=36%
N=43
Q=86%
N=896
Q=40%
N=40
Q=42%
N=40
Q=50%
N=45
Q=69%
N=938
Q=92%
N=63
Q=98%
N=63
Q=30%
N=68
Q=78%
N=764
counts
probability

Figure 2.6 – (previous page) Histograms for each observables- fault lifetime, fault spacing, fault dip and wedge slope for each experimental setup. Normal, Gamma and Laplacian probability distributions are represented in green, red and blue curves respectively. Q value is for the best fit distribution curve based on the Chi square test (Table 2.2) and N indicates the number of samples.

2.3) Experimental observations

All analogue accretionary wedges regardless of μ_{basal} evolve in a cyclic fashion. The cyclic evolution of a wedge involves the growth of the wedge until it reaches the critical taper it can sustain, at which time the formation of a new fault begins the next cycle (Chapple, 1978; Davis et al., 1983; Platt, 1988; Dahlen, 1990; Hoth et al., 2007). In this respect, wedge geometry alternates synchronizing from increasing length of the wedge i.e. horizontal growth by new thrust fault formation and thereby lowering the slope of the wedge, to increasing height of the wedge i.e. vertical growth by underthrusting thus allowing the slope to increase to the critical taper angle. Consequently, fault lifetime, fault spacing and wedge slope are interdependent. According to Dahlen (1990) (equation 99), wedge slope is related to the internal angle of friction of the granular material and basal friction which also governs the fault dip angle, therefore wedge slope and fault dip are related. However, in this study, since fault dip is measured only at the initiation of the fault it is dependent on the internal angle of friction of the granular material and independent of the other observables. This independence of the fault dip from other observables is also evident in a cross-correlation of observables from this study (Fig. A2.2.1) and in the study by Cubas et al. (2010). On a smaller time scale, the geometric change shows systematic cyclicity between accretionary cycles. At the formation of a new fault, the pop-up of the fault at the toe of the wedge provides a linear increase in length of the wedge. At this point the height of the wedge is stationary. The height increases at the end of an accretionary cycle thus steepening the slope of the wedge. On a larger time scale, over multiple accretionary cycles, wedge growth according to critical wedge theory with a roughly constant slope results in an increase in height and width over time according to power law functions (Dahlen, 1990).

In a self-similar like wedge, which grows ideally by "regular" accretion (i.e. adding material in a fashion optimized to maintaining the critical taper throughout wedge evolution) fault lifetime and fault spacing are related and they evolve systematically throughout the evolution of the wedge: For high μ_{basal} wedges fault lifetime and spacing increases over time. As a result of the underthrusting mode both are limited by the length of the wedge (Gutscher et al., 1996). For low μ_{basal} wedges which grow rather by frontal than basal accretion fault lifetime and spacing stabilizes towards a value which is consistent in maintaining the critical taper (Fig. 2.5). In terms of intrinsic variability, fluctuations around these consistent trends become important. Noticeably fluctuations are minimized in wedges with a thin or absent décollement layer (setup 1b and 0). In wedges with a thick décollement layer (setup 3, 2, 1a), distinct faults can be extra-long lived (i.e. they are apparently longer active than necessary to maintain the critical taper) and thus increase the spacing between two adjacent faults (Fig. 2.5). Such extra-long lived faults occur when the fault that underthrusts the wedge is occasionally weakened due to the entrainment of low friction material along the fault plane (glass beads from the thick décollement layer). On the other hand, lack of such a weakening mechanism can cause older faults to be reactivated in order to heighten the wedge to the taper angle (Platt, 1988).

The reactivation of internal pre-existing faults can be classified as second order deformation and formation of new faults at the toe of the wedge as first order deformation. In both styles of deformation the height of the wedge is increased to conform to the critical taper. The two

varying styles of deformation are observed in setup 1a and 1b which demonstrate underthrusting style of deformation (Fig. 2.2) and fault reactivation (distributed strain) respectively. Difference in the two setups is observed in the fault lifetime and spacing (Fig. 2.5). Underthrusting produces long-lived faults followed by short lived faults, whereas wedges with uniformed spaced first order faults may consist of fault reactivation.

2.4) Statistical results

Histograms of the observables for each setup are represented by one of the three distribution types, Normal, Gamma and Laplacian. The best fitting type of distribution for each population is calculated by the Chi square test (χ^2) (Table 2.2). The main goal of representing the populations with distribution curves is to describe the symmetry and variability of the populations. For many of the populations, the difference between χ^2 calculated for each distribution type is very small (Table 2.2), therefore, all three distribution curves have been displayed in Fig. 2.6. The majority of the observables are best represented by a Gamma or Laplacian distribution (Table 2.2). Histograms of the fault dip for the setup 3 and 1b represent a Normal distribution. Fault spacing for setup 0 is best represented by a Normal distribution but can also be described as a Gamma or Laplacian distribution since the χ^2 test for all three distributions is very similar. Fault dip for many setups could be represented as a bimodal distribution, however the difference in dip between each peak and mean value is approximately 2^o which is within the error bars of the estimation. Observable back thrust dip between different setups is indistinguishable within the standard deviation (approximately 3°) and is not further considered in this analysis. The maximum CV for all setups is for the observable fault lifetime followed by the related observable fault spacing that has the second highest CV. The minimum CV for all setup is for the populations related to dip (Table 2.2, Fig.2.7a). Fault dips also have mean values that decreases with increasing μ_{basal} (Fig. 2.6). Wedge slope has a lower variability (CV ranges from 0.12 to 0.33 for all setups) compared to fault lifetime (CV= 0.19-0.56) and spacing (CV= 0.12-0.36), however the mean value for all three observables are linked and show a decreasing trend with decreasing μ_{basal} in this probabilistic approach (Table 2.2, Fig. 2.6). Overall the observables from the reference setup (setup 0) experiments are more symmetrical than of lower μ_{basal} where many of the distribution curves of the observables are right skewed. The distribution for fault lifetime-setup 3 and 2 can also be considered bi-modal. However, the second mode is not well developed and not present for the related observable fault spacing of the same setups. Aside from setup 0 and the experiment with a thinner décollement layer (setup 1b), the trend of the CV for the observables fault lifetime and spacing increase as μ_{basal} decreases for the other three setups (setup 3, 2, 1a) (Fig. 2.7a).

The ANOVA test is used primarily to quantify the variation in the results within a population and determines whether results in the population come from the same system. Fault spacing and lifetime are two observables that have the highest CV especially for setups with glass beads (except setup 1b) due to the co-existence of large and short lived faults. Despite this observation the ANOVA test concludes that all results for the population fault spacing and lifetime come from alike experiments. Therefore the ANOVA test also recognizes that the magnitude of the variation in the observables is also repeatable between the experiments. For

the observable fault lifetime in all the setups, the p- value supports the hypothesis that there is no difference between experiments within the setups. On the contrary, results show that there is a difference (p-value below 5%) between experiments for the population fault dip for the setup 1a , fault spacing for the setup 0 and 1b and back thrust dip for the setup 2 (Table 2.3). In these populations, an outlier in any one of the experiments causes a different magnitude of variability than the other experiments and thus the results of the ANOVA test reject the null hypothesis. If there realistically is a difference between experiments in a population then the ANOVA test would show a rejection of the null hypothesis for all the observables in that setup, which is not the case.

F values clearly support the hypothesis that there is a difference between experiments of different μ_{basal}. From the ANOVA, the three experimental setups with the same décollement thickness - setup 3, 2, 1a show an overall decreasing trend in the p value for the observables fault lifetime and spacing, indicating that the difference in the variance between experiments increases as μ_{basal} decreases (Fig. 2.7b). However the p values are not below the 5% significance level and the null hypothesis that all measurements in the populations come from similar sources is accepted. In contrast the R^2 value for the above mentioned observables and setups increases with decreasing μ_{basal} indicating that the statistical variance due to variations between experiments in a population (Fig. 2.7c) also increases. Compared to the other setups the same observables - fault lifetime and spacing - of setup 0 and 1b have lower p values (the null hypothesis for fault spacing of setup 0 and 1a are rejected) and higher R^2 values. Also indicating that the difference between the variances of different experiments is high but this variation is not within the experiments but due to extrinsic sources. However the difference between the variances for these two setups is not higher than that for setup 3, 2, 1a since the CV for fault lifetime and spacing for setup 0 and 1a is still lower than that for setup 3, 2, 1a (Table 2.2, Fig. 2.7a).

Although majority of the p values (Table 2.3) for all observables and all setups support the hypothesis that there is no difference in measurements between experiments, there are some exceptions. These exceptions can be explained by outliers in the data. An outlier or value significantly larger or smaller than the mean value in an experiment causes a different variance for that experiment. When this experiment is compared to other experiments of the same setup but with a significantly different variance, the calculated p value appears to be less than the 5% significance level.

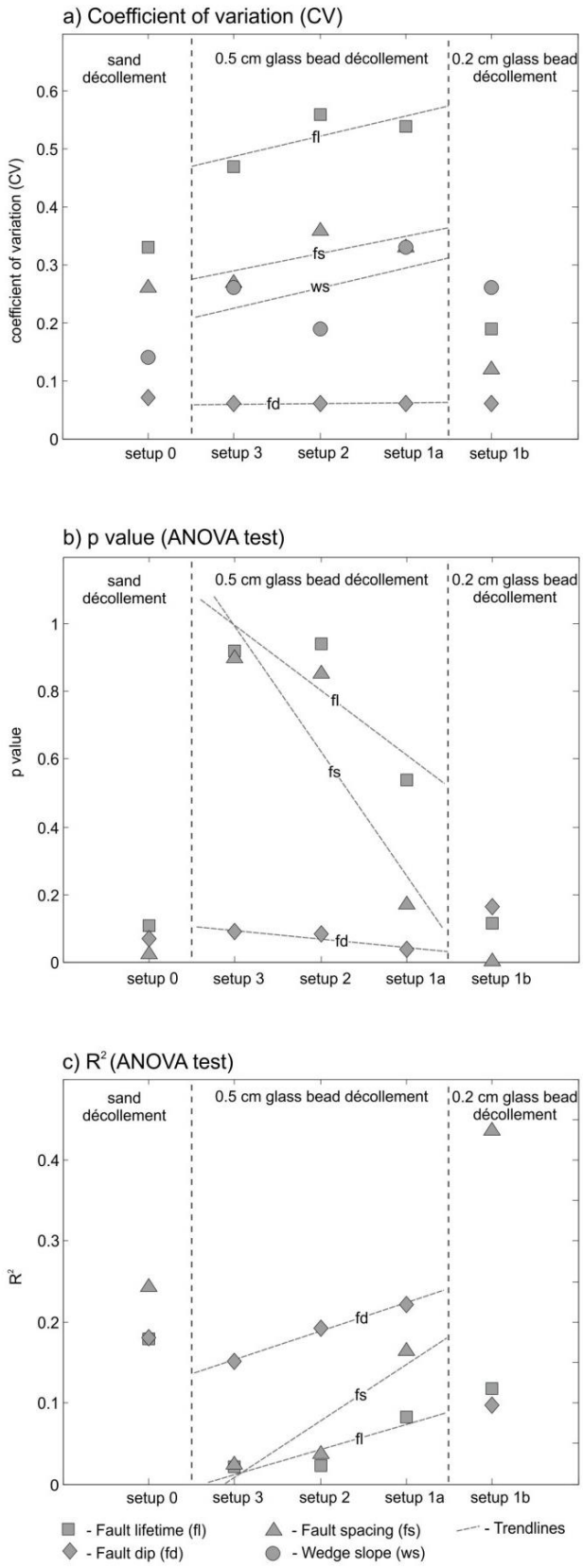

Figure 2.7- Plots showing the comparison of a) CV b) p value (ANOVA test) and c) R^2 (ANOVA test) for each observable in the different setups. Linear trendlines are only shown for setups 3, 2, 1a since they differ from the other setups (0 and 1b) in the style of deformation and the thickness of the décollement layer

Setup		**Fault lifetime**	**Fault spacing**	**Fault dip**	**Back thrust dip**
	between experiments of each setup				
Sand setup 0	p value	0.10	**0.02**	0.06	0.91
	R^2	0.17	0.24	0.18	0.03
	F value	1.85	**2.74**	2.08	0.33
	F crit	2.28	2.28	2.26	2.26
Sand +300-400 µm GB setup 3	p value	0.92	0.90	0.08	0.66
	R^2	0.02	0.02	0.15	0.04
	F value	0.22	0.26	2.15	0.60
	F crit	2.58	2.58	2.56	2.57
Sand +200-300 µm GB setup 2	p value	0.94	0.85	0.08	**0.03**
	R^2	0.02	0.03	0.19	0.23
	F value	0.19	0.33	2.25	**2.92**
	F crit	2.65	2.65	2.61	2.61
Sand +100-200 µm GB setup 1a	p value	0.53	0.16	**0.03**	0.46
	R^2	0.08	0.16	0.22	0.08
	F value	0.79	1.71	**2.85**	0.92
	F crit	2.64	2.64	2.60	2.60
Sand +100-200 µm GB setup 1b	p value	0.11	**8.36E-07**	0.16	0.07
	R^2	0.11	0.43	0.09	0.12
	F value	1.94	**11.20**	1.69	2.24
	F crit	2.53	2.53	2.51	2.52
	between different basal frictions or setups				
	p value	**1.42E-08**	**2.94E-14**	**4.54E-13**	**0.03**
	R^2	0.59	0.77	0.62	0.17
	F value	**16.85**	**39.12**	**26.54**	**2.73**
	F crit	2.57	2.57	2.51	2.55

Table 2.3- ANOVA test results for each observable for each experimental setup. The calculated p-value, R^2, Fisher value and critical Fisher value are shown in the table. Bold values indicate a rejection of the null hypothesis.

2.5) Discussion

Here I discuss the range of variability between different fault observables (i.e. fault lifetime, fault spacing, fault dip) and wedge observables (i.e. wedge slope) and the difference in the variability between different setups. It is demonstrated that the mechanics of deformation controls the intrinsic variability in observables and that regardless of the varying intrinsic variability in the populations, the mechanical relationship between fault, wedge observables and μ_{basal} is apparent. Since the experiments consist of large amounts of shortening and formation of many faults, I also examine the time evolution of the wedge and it's reflection on the statistical data.

2.5.1) Intrinsic variability in fault observables

It is observed that fault observables of the same setup have different magnitudes of variability. For example fault lifetime and spacing have a higher variability and asymmetry than fault dip. Since faults are first order structures that change the geometry of the wedge, they also influence any variability in the wedge slope. As a feedback fault lifetime is determined by wedge criticality. Any changes in the physical properties of the wedge changes the frequency of fault formation therefore making the observables fault lifetime, fault spacing and wedge slope dependent on each other. Since wedge slope is also dependent on the μ_{basal} and $\mu_{internal}$ (Davis, et al., 1983; Dahlen, 1990) which determines the fault dip, all observables are related to each other. However, fault lifetime and fault spacing show a significantly higher CV than fault dip and back thrust dip (Table 2.2). A comparison of the CV for all the fault observables reveals that the CV for fault lifetime and fault spacing range from 0.12 to 0.56. The CV for fault dip is significantly lower and ranges from 0.06 to 0.07. This observation for fault dip is also evident in the study by Cubas et al. (2010). The main difference between the observables is that fault lifetime and spacing are time dependent. As the wedge grows the mechanical process related to fault frequency may change with the evolution of the wedge (Platt, 1988). Wedge slope in the experiments is also time dependent and changes both within an accretionary cycle and as the wedge grows toward criticality over multiple cycles. Effectively criticality in "real" wedges might vary over time because of the weakening of the wedge due to incorporation of weak faults. The skew in fault lifetime and spacing populations (Fig. 2.6) or possible development of a second mode in the fault lifetime distribution (setup 3 and 2) may reflect evolving wedge dynamics. This explains why fault lifetime, fault spacing and wedge slope have a higher CV than fault dip. Fault dip and back thrust dip in this study are not time dependent since they are measured only at the instance when a new fault is formed and not throughout the lifetime of the fault. Since these two observables only depend on the μ of the granular material, there is little possibility for variation thus generating a smaller CV than the other observables.

2.5.1.1) Low variability of fault dip

The low variability in fault dip is represented by a CV = 0.06-0.07, and mostly symmetrical type of distribution. Since the dip is measured at the initial formation of the fault, the change in dip i.e. rotation of the fault during the rest of the accretionary cycle is not recorded. Therefore the measurement is not time dependent. Fault dip initiates at the velocity discontinuity between the conveyor belt and the overlying granular layer. After initiation it

propagates into the overlying sand layer (Suppe and Medwedeff, 1990). The relationship between fault dip and μ is defined as

$$\delta = 45 - \frac{\phi}{2} - \psi \quad (1)$$

where δ is the angle of the fault, ϕ is the angle of internal friction of the sediment (in this case the sand) and ψ is the angle between the maximum compressive stress and the x axis (Coulomb, 1773; Hafner, 1951; Lallemand et al, 1994). Therefore fault dip is related only to ϕ and ψ at any point in time. A range in the μ_{basal} or a measuring error may explain the small variations in fault dip. In these experiments granular material is used with a particular range in grain size to control the μ_{basal}. Since there is a range in the grain size, this also produces a range in the μ_{basal} and may produce the small range in fault dip measurements. On the other hand, the highest standard deviation for the fault dip is $\pm 1.92^{o}$ (Table 2.2). The estimated measuring error is 2^{o} and the highest standard deviation for frictional coefficients measured in the Ring shear tester is ± 0.047 for sand on a conveyor belt (Fig A2.2E). This would produce a deviation of $\pm 2.67^{o}$ ($\phi = \tan^{-1} \mu$). Therefore the variation in fault dip could come from the variation in the size of the granular material or measuring error.

2.5.1.2) Variability in fault lifetime and spacing

The $\mu_{internal}$ and μ_{basal} of the wedge controls the slope or critical taper of the wedge (Davis et al, 1983; Dahlen, 1984; Dahlen, 1990; Suppe, 2007). The critical taper is directly related to the fault strength, in particular to the properties of the décollement, and inversely related to the wedge strength or cohesion and internal angle of friction of the wedge (Dahlen, 1990; Suppe, 2007). Since faults are the first order structures that aid in changing the geometry of the wedge and hence the taper, the lifetime and accordingly the spacing of the fault is such that it is able to bring the wedge slope to the preferred taper. Therefore, the lifetime of a fault is dependent on wedge slope (Chapple, 1978).

In setup 0, the experiments have the highest μ_{basal} and since there is a strong basal coupling, the resulting wedge is steeper than the wedges from the other setups (Table 2.2, Fig. 2.6) (Gutscher et al, 1996; Saha et al., 2013). In this setup thrust sheets continue to underthrust the wedge to raise the height of the wedge. Compared to setup 1b where the μ_{basal} is lowest, the resulting wedge is shallower (Fig. 2.6) and the wedge deforms by frontal accretion. In both these setups the fault lifetime and spacing have trends that are similar over time (Fig. 2.5). However the slight skewness in the distributions (Fig. 2.6) is mainly because the two observables are time dependent. At the beginning of the wedge formation, faults are short lived and closely spaced. As the wedge is established and due to self-similar like growth of the wedge the fault properties also grow creating a skew in the distribution (Saha et al., 2013).

In a system (setup 3, 2, 1a) with altering fault properties due to the entrainment of glass beads, the internal wedge properties also change. Lowering of the fault plane friction can lengthen the fault lifetime as a result, making deformation easier to continue along the fault for a longer time (Platt, 1988; Cubas et al, 2008). To compensate for the long duration of these faults, long lived faults are always followed by short lived faults. Perhaps, this is the wedges way to return back to a state of criticality. In these setups, the long-lived faults produce a skew towards larger faults or even the formation of a second peak in the histograms (Fig. 2.6). The

skewness or asymmetry in the histograms represents the evolution of the wedge over time in particular the change in fault properties. As a result of the large difference in fault length, the distributions for both fault lifetime and fault spacing are further skewed for these setups compared to setup 0 and 1b.

2.5.1.3) Influence of thickness on granular basal décollement

The evolution of the wedge is affected by the physical properties of the initial sand layer and décollement layer. This study demonstrates that the thickness of the granular décollement layer also influences the style of deformation that the wedge employs to reach its critical taper. The influence of the thickness of the décollement layer can be seen in the experiment with setup 1a and 1b. The only difference between the two setups is the thickness of the basal décollement layer. Setup 1a has a décollement layer of ~ 0.5 cm and setup 1b has décollement layer of ~ 0.2cm. When a new fault is formed in the wedge with a thick décollement layer, the glass beads from the décollement layer get entrained onto the fault plane lowering the frictional coefficient along the fault plane. This allows the wedge to continue deforming along the weak fault plane and to continue underthrusting the wedge allowing it to grow in height. In this manner, a thick décollement layer weakens the fault plane by the entrainment of low friction material changing the style of deformation from frontal accretion to underthrusting (Platt, 1988). This interaction between materials of differing friction also affects the wedge making it heterogeneous and changing the overall strength of the wedge. Since the critical taper is dependent on a force balance that includes the cohesion and internal friction (Davis et al., 1983), the taper changes and the wedge must adjust accordingly. The adjustment of the wedge over time as a response to changing parameters and an evolving taper is represented by an asymmetric distribution or possible second peak that represents the change in fault behavior.

A thinner basal décollement layer allows the frictional properties of the fault and consequently the physical properties of the wedge to remain more consistent throughout the growth of the wedge. Therefore there is no change in the force balance or the preferred critical taper angle. In comparison to the wedges with altering fault plane friction, the wedges with thin décollement layer (setup 1b) or décollement layer with granular material that is the same as the rest of the wedge (setup 0), have a very periodic and predictable fault lifetime and spacing. This observation is strongly supported by the lower CV for observables fault lifetime and spacing in setup 1b and 0 compared to the CV of the same observables in setup 1a (Table 2.2, Fig 2.7). Since the experiments with wedges of thin décollement layer (setup 1b) show little or no evidence of underthrusting, deformation moves to older faults and reactivates these older faults to raise the height of the hinterland part of the wedge in order to reach the preferred taper angle (Platt, 1988).

2.5.2) Mechanical causes for the differences between setups

Fault dip, fault lifetime and spacing and consequently wedge slope are all related to the μ of the entire wedge i.e. $\mu_{internal}$ and μ_{basal} of the wedge. In this study a difference as low as 0.03 in the μ_{basal} shows a systematic change in fault and wedge observables. The relationship shows that as μ_{basal} increases, fault lifetime and spacing also increase but fault dip decreases (Davis

et al., 1983, Dahlen, 1984; Konstantinovskaia and Malavieille, 2005). In addition, the thickness of the décollement layer between setups causes a significant difference in the mechanical evolution of the wedge for the different setups.

2.5.2.1) Relationship between basal friction and fault lifetime and spacing

Fault lifetime and spacing decreases for decreasing μ_{basal} primarily because of the frictional properties of the décollement granular material and its relationship to the critical taper angle. For low μ_{basal} the critical taper angle is low therefore a deforming wedge of certain length does not have to grow as much in height compared to a wedge with the same length but higher μ_{basal}. Thus, fault structures that are essential in changing the geometry of the wedge are driven by the μ_{basal} of the wedge. The lifetime of the fault is directly related to the height of the critical wedge and how much the wedge must be underthrusted for the wedge to reach the critical height (Davis et al., 1983; Cubas et al., 2008).

In the wedges (setup 3, 2, 1a) with the thick (~0.5 cm) décollement layer the entrainment of low friction material along the fault plane changes the style of deformation of the wedge. These wedges with a thick décollement layer produce long faults followed by short lived faults therefore producing a skewed distribution of fault lifetime and spacing (Fig. 2.6). Accordingly, the CV for fault spacing and fault lifetime for setup 3, 2, 1a are higher than that for setup 0 and 1b.The experiments with setup 0, 1a and 1b has the highest and lowest μ_{basal} respectively in this study. Setups 0 and 1b have little change to the physical properties of the fault plane thus producing a more symmetric distribution of fault lifetime and spacing (Fig. 2.6).

Although the experiments have a systematic change in the μ_{basal}, the statistical results i.e. CV, p value and R^2 value show that the experiments can be further divided into two categories based on the thickness of the décollement layer and the resulting style of deformation. Accordingly the CV is lower for the experiments with evenly spaced faults (setup 0 and 1b) and higher for experiments with underthrusting due to weakened faults (setup 3, 2, 1a) (Fig. 2.7a). In addition for the latter experiments the CV increases as μ_{basal} decreases. The p value shows a decreasing trend and R^2 an increasing trend (Fig. 2.7b, c), indicating that as μ_{basal} decreases the repeatability value of experiments decreases. This observation could imply that wedges with lower μ_{basal} become more susceptible to extrinsic changes if all other components within the system are the same for each setup. It is known that experimental artifacts become significant when basal friction is very low in comparison to lateral friction (Vendeville, 2007), and this would also produce very low p values.

2.5.2.2) Increase in fault dip due to decreasing basal friction

For all the setups the fault dip for the fore thrusts ranges from 26^o +/- 1.82 to 30^o +/- 1.92, and increases with decreasing μ_{basal}. As μ_{basal} decreases by an average of 0.07 fault dip increases by a minimum of 0.6^o. In these experiments the décollement layer is sand (setup 0) or glass beads (setup 3, 2, 1a and b). Fault dip is controlled primarily by the mechanics of faulting, in particular the internal angle of friction (Hafner, 1951). Since the fault propagates from the velocity discontinuity between the conveyor belt and the décollement layer, fault dip is related

to the internal angle of friction for sand (setup 0) and glass beads (setup 3, 2, 1a, b). Mechanically, the dip of a fault is also related to the orientation of the maximum component of stress (σ_1). In a completely Andersonian setting i.e. where shear stress at the base is zero, ψ (equation 1) is also zero. In this case, the orientation of the maximum stress component is parallel to the convergence direction in a uniform thickness of incoming granular material. However, in these experimental settings, there is the formation of shear zone between the conveyor belt and the granular material. Here the magnitude of the shear stress is proportional to the μ_{basal}. As shear stress at the base increases due to increasing μ_{basal} so does the rotation of the maximum stress component and increase in ψ. Therefore, according to equation 1, the consistent decrease in fault dip with increasing μ_{basal} is an effect of the rotation of the maximum stress component from the horizontal. This is also consistent with the findings of Davis and Engelder (1985) studying salt detachments. Statistically fault dip demonstrates a consistently low CV for all the setups regardless of μ_{basal}, style of deformation and in comparison to the other observables (Fig. 2.7a). This supports the idea that in each setup fault dip is dependent only on the internal angle of friction of the granular material and independent of other observables. For the three setups that demonstrate underthrusting (setup 3, 2, 1a), p values for fault dip tend to decrease and R^2 show a shallow but increasing trend, also indicating an increased effect of the extrinsic variability possibly due lower stability in the system when μ_{basal} is lowered. This observation is similar to the other observables of the same setups.

2.5.2.3) Relating interpretations of the statistical analysis to geodynamic natural observations

The statistical trends produced from this study are more beneficial if they can be related to observations in nature. It is important to note the mechanical interaction of parameters (i.e. coefficient of friction, basal friction) when interpreting data from nature or creating models. In particular, for observables (fault lifetime, spacing or wedge slope) that may have a high variability, a distinctive solution may not be apparent (for example, in this study, the change in fault lifetime and spacing is due to the change in fault plane friction). Therefore to make reliable interpretations a larger data set is preferred. In addition if the probability distribution curve is known for that observable then this may also aid in the strength of the interpretations. On the other hand, if the observable is highly variable, it presents a clue that there are other controlling factors involved and that need to be investigated. Ideally, when creating a model (analogue or numerical) of a natural system, quantitative values of the physical parameter ($\mu_{internal}$, μ_{basal}, fault plane friction) of the system are taken from nature. However, if the parameter is known to vary especially over time, then it is also important to test a range of values in the model.

It is also important to know the evolutionary stage of deformation. For example one system can have two styles of deformation over time - frontal accretion at earlier stages of the evolution of the wedge and subsequent predominance of underthrusting. Statistically they may originate from the same system. However measurement taken from one or the other stage or at the transition between stages can result in varying interpretations about the initial setting. Furthermore, a change in the fault behavior observed in the field may not necessary mean a

different system but only a change in the deformation style due to internal or external influences on the system. This study is an example of this case and shows that this change in the style of deformation can be initiated by a small change in the thickness of the décollement layer.

2.6) Conclusion

Observables related to faults show different magnitudes of variability although they are from the same experimental setup. For example fault dip (CV= 0.06-0.07) shows a lower variability than fault lifetime (CV= 0.19-56), spacing (CV= 0.12-0.36) and wedge slope (CV= 0.12-0.33). The difference in variability is related to the dependency of the observable on the interaction of different components of the wedge as it evolves. Fault dip is only dependent on the internal angle of friction of the basal and overlying granular material and measured at the initial stage of formation of the fault, therefore the CV for fault dip is low. In contrast fault lifetime, spacing and subsequently wedge slope varies with changes in the growth of the wedge. Other dynamic changes in the wedge that affect fault lifetime and spacing is the change in fault plane friction due to entrainment of low friction material from a thick décollement layer.

A difference in μ_{basal} between 0.03 and 0.15 among the varying setups is statistically distinguishable for all observables. Fault lifetime, fault spacing and related wedge slope decrease with decreasing μ_{basal}. Fault dip increases with decreasing μ_{basal}. These observations are consistent with the mechanics of faulting and deformation of the wedge defined by the critical taper theory (Davis et al., 1983). The setups can be further categorized based on the style of deformation resulting from the difference in initial setup design. The statistical test ANOVA confirms that data from experiments within each setup are repeatable to a high degree (low R^2 values – Table 2.3). Moreover, the statistical results (p value and R^2 from the ANOVA test) show that repeatability decreases in setups with high CV and decreasing μ_{basal}. Overall, results signify that the variability of the observables is related to its dependency on the complexity of the system. Therefore, when applying a theoretical analysis, for example, wedge mechanical analysis to natural systems one needs to take into consideration the possible range of values for each observable from natural observations (Maillot et al., 2007; Cubas et al., 2013).

Repeating experiments presents the opportunity to quantify the intrinsic variability that is due to geodynamic processes in the experimental system. It allows one to identify the robustness of the results. A single result from one experiment could be near or far from the precise mean value and this uncertainty can be minimized by the repetition of experiments. Thus adding a higher degree of precision to the interpretations. This does not imply that data from previous analogue modelling studies that lack repetition are incorrect. The study also shows that despite the higher variability in some observables, the relationship between μ_{basal} and mean values for fault and wedge observables is evident. Many observables from previous experiments that are quantitatively measured like fault dips have a low variability, therefore interpretations are credible. Repeating experiments also allows the experimenter to assess whether the variability of the results is due to the experimental setup or due to the processes involved in the system and accordingly improve the design. Thus, experimenters are advised

to repeat experiments especially those created to study complex tectonic processes, if the technical possibility exist.

Below is a summary of the statistical tools that can be used to analyze data from repeated experiments for better interpretation of the results.

1) Represent the results or observables with distribution curves to qualitatively describe the variability. Determine which distribution best fits the population by calculating the χ^2 for each distribution. I advise to use the statistical analysis by Cubas et al. (2010) - Appendix 2.1.
2) The type of distribution that represents a population indicates the variability and also the sensitivity of the observable. An observable that is more sensitive to changes in the system or dependent on other observables will have a population with a large statistical variation (fault lifetime, fault spacing and wedge slope). On the contrary, populations with small statistical variations are from independent observables like fault dip.
3) Use the variability between experiments to determine how reproducible data from experiments are with the help of the ANOVA test. The p value and R^2 value indicate not only whether the experiments are repeatable but also to what extent. In this study it is observed that experiments with low μ_{basal} are less repeatable. This observation could imply that wedges with lower μ_{basal} become more susceptible to extrinsic changes if all other components within the system are the same.

References

Adam, J., Urai, J.L., Wieneke, B., Oncken, O., Pfeifer, K., Kukowski, N., Lohrmann, J., Hoth, S., van der Zee, W., Schmatz, J., 2005. Shear localization and strain distribution during tectonic faulting- new insights from granular-flow experiments and high-resolution optical image correlation techniques. Journal of Structural Geology 27, 283-301.

Chapple, W.M., 1978. Mechanics of thin-skinned fold-and thrust belts. Bulletin of Geological Society of America 89, 1189-1198.

Coulomb, C.A., 1773. Essai sur une application des règles de maximis et minimis à quelques problems de statique relatifs à l'architecture. Mémoires de Mathématiques et de Physique, Académie Royale des Sciences 7, 343-382.

Cubas, N., Maillot, B., Barnes, C., 2013. Inverse method applied to a sand wedge: Estimation of friction parameters and uncertainty analysis. Journal of Structural Geology 55, 101-113

Cubas, N., Maillot, B., Barnes, C., 2010. Statistical analysis of an experimental compressional sand wedge. Journal of Structural Geology 32, 818-831.

Cubas, N., Leroy, Y.M., Maillot, B., 2008. Prediction of thrusting sequences in accretionary wedges. Journal of Geophysical Research 113, B12412, doi:10.1029/2008JB005717.

Dahlen, F.A., 1984. Noncohesive Critical Coulomb Wedges: An Exact Solution. Journal of Geophysical Research 89 (B12), 10,125-10,133.

Dahlen, F.A., 1990. Critical Taper model of fold-and-thrust belts and accretionary wedges. Annual Review of Earth and Planetary Science 18, 55-99.

Davis, D., Engelder, T., 1985. The role of salt in fold-and-thrust belts. Tectonophysics 119(1), 67-88.

Davis, D., Suppe, J., Dahlen, F.A., 1983. Mechanics of Fold and Thrust Belts and Accretionary Wedges. Journal of Geophysical Research 88 (B2), 1153-1172.

Fisher, R.A., 1954. Statistical Methods for Research Workers. Oliver and Boyd, Edinburgh.

Graveleau, F., Malavieille, J., Dominguez, S., 2012. Experimental modelling of orogenic wedges: A review. Tectonophysics 538, 1-66.

Gutscher, M-A., Kukowski, N., Malavieille, J., Lallemand, S., 1996. Cyclical behavior of thrust wedges: Insights from high basal friction sandbox experiments. Geology 24(2), 135-138.

Hafner, W., 1951. Stress distributions and faulting. Bulletin of the Geological Society of America 62, 373-398.

Hall, J., 1815. On the Vertical Position and Convolutions of certain Strata and their relation with Granite. Transactions of the Royal Society of Edinburgh 7,79-108.

Hoth, S., Hoffmann-Rothe, A., Kukowski, N., 2007. Frontal accretion: An internal clock for bivergent wedge deformation and surface uplift. Journal of Geophysical Research 112, DOI: 10.1029/2006JB004357.

Konstantinovskaia E., Malavieille, J., 2005. Erosion and exhumation in accretionary orogens: Experimental and geological approaches. Geochemistry, Geophysics, Geosystems 6(2), doi:10.1029/2004GC000794.

Lallemand, S., Schnürle, P., Malavieille, J., 1994. Coulomb theory applied to accretionary and non-accretionary wedges: Possible causes for tectonic erosion and/or frontal accretion. Journal of Geophysical Research 99(B6), 12,033-12,055.

Lohrmann, J., Kukowski, N., Adam, J., Oncken, O., 2003. The impact of analogue material properties on the geometry, kinematics, and dynamics of convergent sand wedges. Journal of Structural Geology 25, 1691-1711.

Maillot, B., 2013. A sedimentation device to produce uniform sand packs. Tectonophysics 593, 85-94.

Maillot, B., Barnes, C., Mengus, J.-M, and Daniel, J.-M., 2007. Constraints on friction coefficients by an inverse analysis of sand box thrust dips. Journal of Structural Geology 29, 117-128.

McKillup, S., Dyar, M.D., 2010. Geostatistics Explained: an Introductory Guide for Earth Scientists. Cambridge University Press, Cambridge.

Platt, J.P., 1988. The mechanics of frontal imbrication: a first-order analysis. Geologische Rundschau 77/2, 577-589.

Rosenau, M., Nerlich, R., Brune, S., Onken, O., 2010. Experimental insights into the scaling and variability of local tsunamis triggered by giant subduction megathrust earthquakes. Journal of Geophysical Research 115, B09314, doi:10.1029/2009JB007100.

Saha, P., Bose, S., Mandal, N., 2013. Varying frontal thrust spacing in mono-vergent wedges: An insight from analogue models. Journal of Earth System Science 122 (3), 699-714.

Schreurs, G., Buiter S.J.H., Boutelier, D., Corti, G., Costa, E., Cruden, A. R., Daniel, J-M., Hoth, S., Koyi, H.A., Kokowski, N., Lohrmann, J., Ravaglia, A., Schlische, R.W., Withjack,

M.O., Yamada, Y., Cavozzi, C., Delventisette, C., Elder Brandy, J. A., Hoffmann-Rothe, A., Mengus, J-M., Montanari, D., Nilforoushan, F., 2006. Analogue benchmarks of shortening and extension experiments. In: Buiter, S.J.H., & Schreurs, G. (Eds.), Analogue and Numerical Modelling of Crustal-Scale Processes. Geological Society of London, 1-27.

Schulze, D.,1994. Entwicklung und Anwendung eines neuartigen Ringschergerätes. Aufbereitungstechnick 35(10), 524-535

Suppe, J., and Medwedeff, D.A., 1990. Geometry and kinematics of fault-propagation folding. Eclogae Geol. Helv. 83, 409-454

Suppe, J., 2007. Absolute fault and crustal strength from wedge tapers. Geology 35, 1127-1130

Vendeville, B.C., 2007. The 3-D Nature of stress Fields in Physical Experiments and Its Impact on Models Overall Evolution. Solicited Oral Contribution. In: EGU General Assembly, Vienna, 15-20 April, 2007

Zar, J.H., 2010. Biostatistical Analysis, Fifth Edition. Pearson Prentice-Hall, New Jersey.

Appendix A2.1
Methods: Derivation of material properties using a ring-shear tester

Material properties were derived using a Schulze Ring shear tester specially designed to measure friction coefficients in loose granular material accurately at low confining pressures and shear velocities similar to sandbox experiments (Lohrmann et al., 2003; Schulze 1994). In this tester, a sand layer is sheared either against a base or internally at constant normal load and velocity while the shear stress is measured continuously. The resulting stress curve (example shown in Appendix Fig. A2.1) typically rises from zero to a peak level (= static friction) within the first few millimetres of shear before it drops and stabilizes after formation of a shear zone in the material or at the interface (= kinetic friction). Stopping the shearing and resetting the shear stress followed by a renewed shearing (re-shear) results in a second, similar shear curve whose peak (= reactivation static friction) is somewhat lower than the first peak. From these curves, the strengths at first and second peak as well as on the plateau are picked manually and assigned static, reactivated static and kinetic frictional strength for the applied normal load, respectively. Density of material is calculated based on the weight of the material sieved into the shear cell and the volume which is monitored accurately throughout the shear test.

Two analysis methods are applied to derive friction coefficients and a realistic variability from that data: First, linear regression of the normal load vs. shear strength data pairs, i.e. by fitting a linear failure envelope to the data in the Mohr space. The slope of the line and the y-axis intercept are accordingly the friction coefficient and cohesion, respectively. However, because this method overestimates real precision and may be biased by a curved failure envelope a second analysis is performed which relies on calculating all possible two point slopes and intercepts for mutually combined data pairs. These data are then evaluated by means of univariate statistics by means of calculating mean and standard deviation and comparing the probability density function (pdf) to that of a normal distribution. Usually it is found that the peaks of the experimental pdf are much narrower than a normal distribution pdf suggesting that the calculated standard deviation is a conservative value which tends to underestimates real precision. The standard deviations reported in Table A2.1 represent a trade-off between the mean and standard deviations derived by the two methods described above. Because inferred cohesion values are low (in the order of view tens of Pa) and show a large scatter (tens to hundreds of Pa) cohesion values are not relied on but it is conclude that cohesion is neglectable in the material.

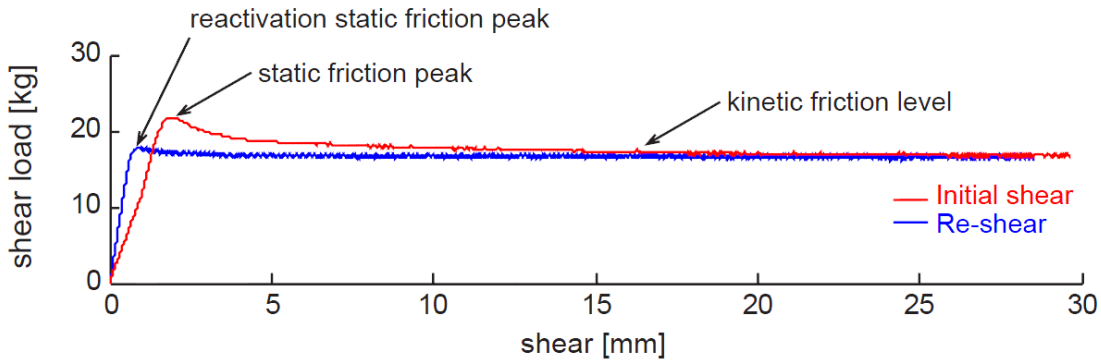

Figure A2.1.1- Example of stress curve raw data as derived from Ring shear testing. See text for explanation.

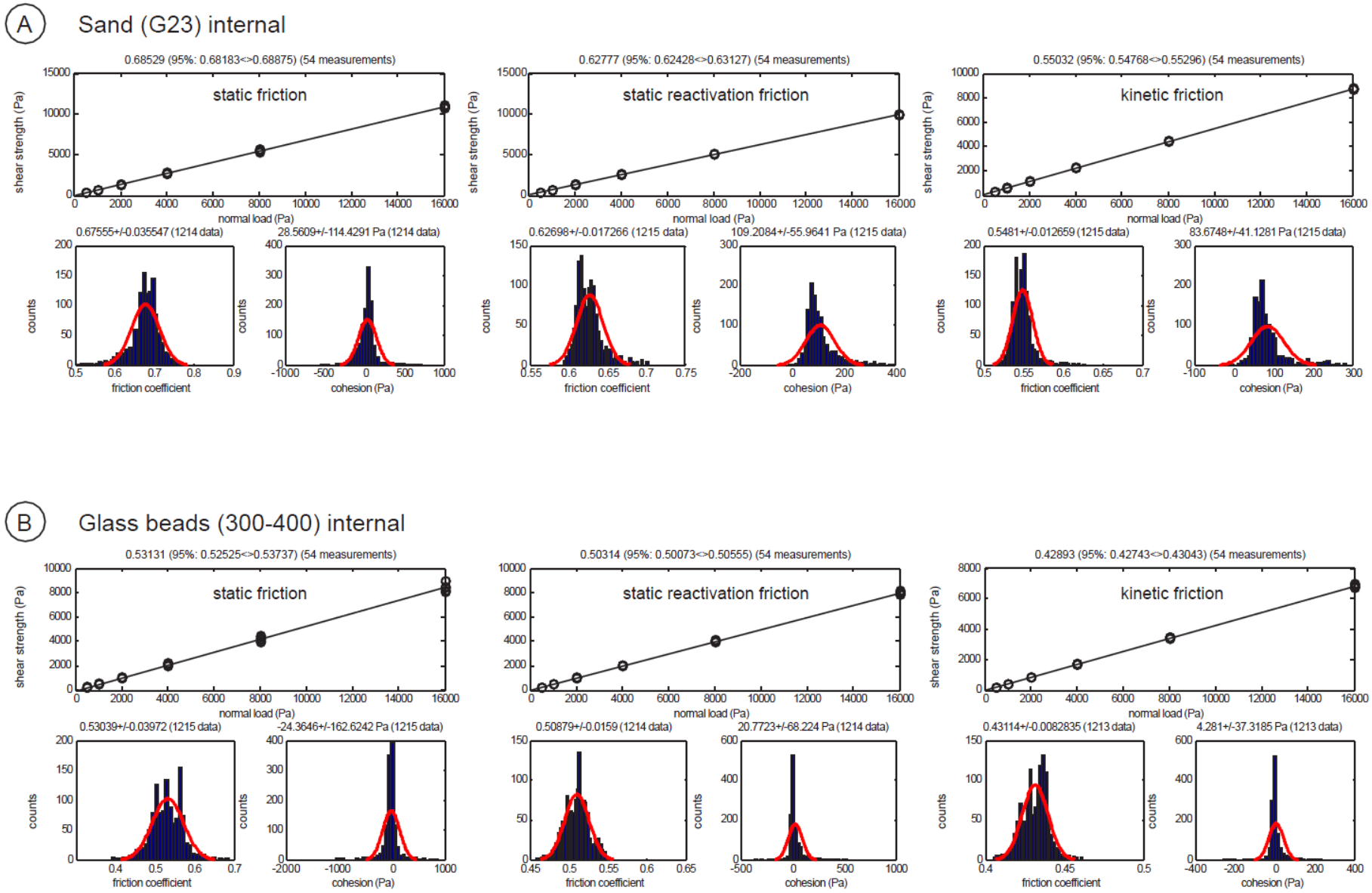
A
Sand (G23) internal
0.68529 (95%: 0.68183<>0.68875) (54 measurements)
static friction
shear strength (Pa)
normal load (Pa)
0.67555+/-0.035547 (1214 data)
28.5609+/-114.4291 Pa (1214 data)
counts
friction coefficient
cohesion (Pa)
0.62777 (95%: 0.62428<>0.63127) (54 measurements)
static reactivation friction
0.62698+/-0.017266 (1215 data)
109.2084+/-55.9641 Pa (1215 data)
0.55032 (95%: 0.54768<>0.55296) (54 measurements)
kinetic friction
0.5481+/-0.012659 (1215 data)
83.6748+/-41.1281 Pa (1215 data)
B
Glass beads (300-400) internal
0.53131 (95%: 0.52525<>0.53737) (54 measurements)
static friction
0.53039+/-0.03972 (1215 data)
-24.3646+/-162.6242 Pa (1215 data)
0.50314 (95%: 0.50073<>0.50555) (54 measurements)
static reactivation friction
0.50879+/-0.0159 (1214 data)
20.7723+/-68.224 Pa (1214 data)
0.42893 (95%: 0.42743<>0.43043) (54 measurements)
kinetic friction
0.43114+/-0.0082835 (1213 data)
4.281+/-37.3185 Pa (1213 data)

C Glass beads (200-300) internal

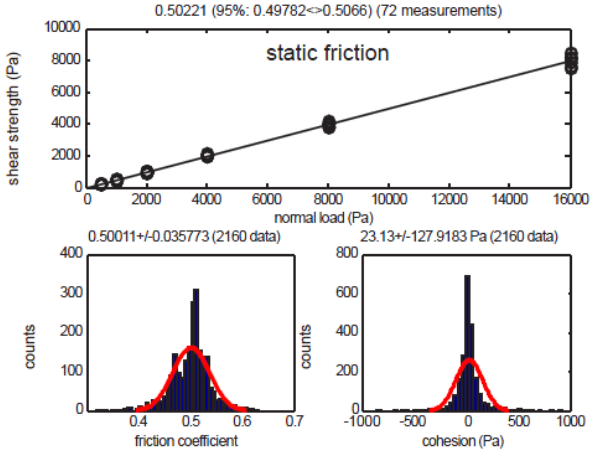

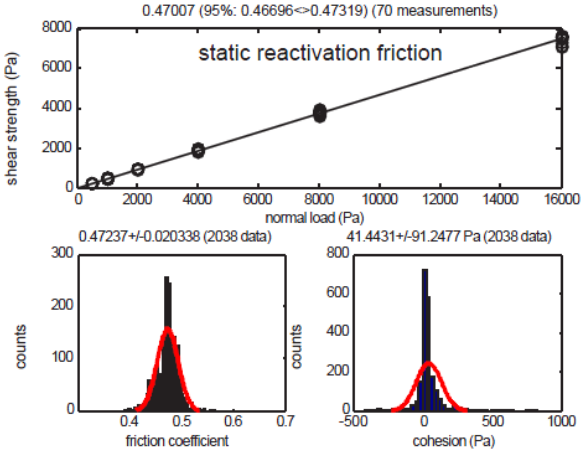

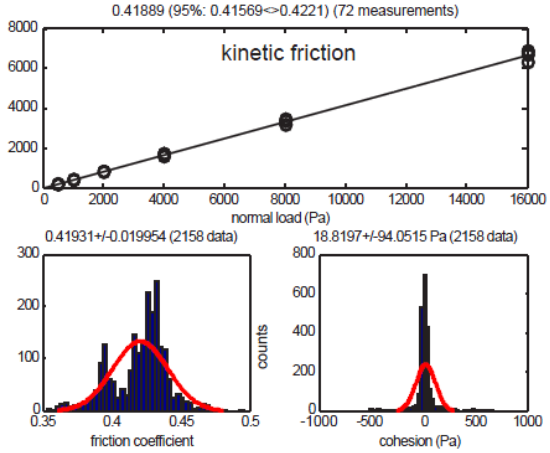

D Glass beads (100-200) internal

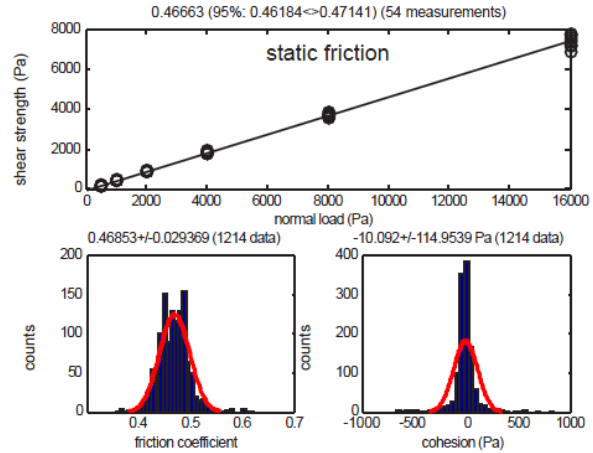

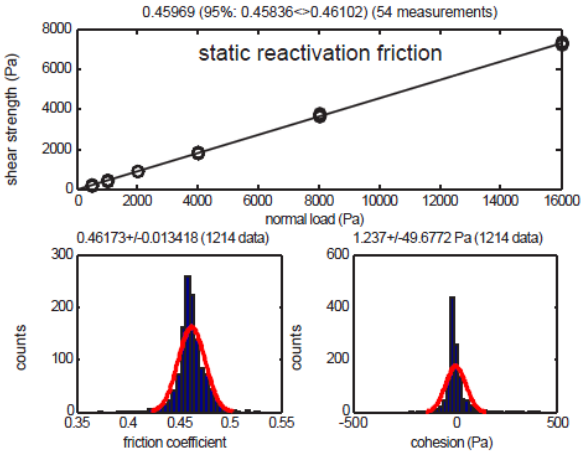

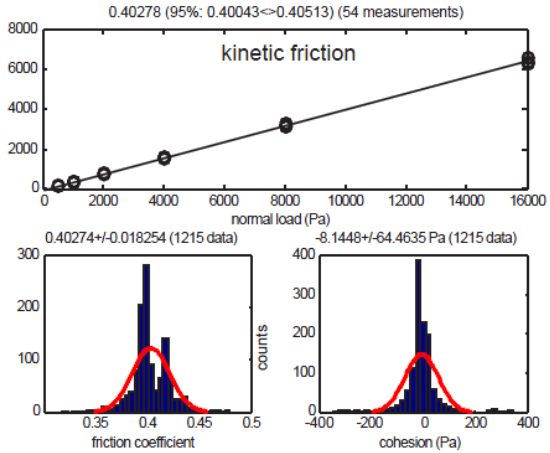

E Sand (G23) basal on black rubber belt

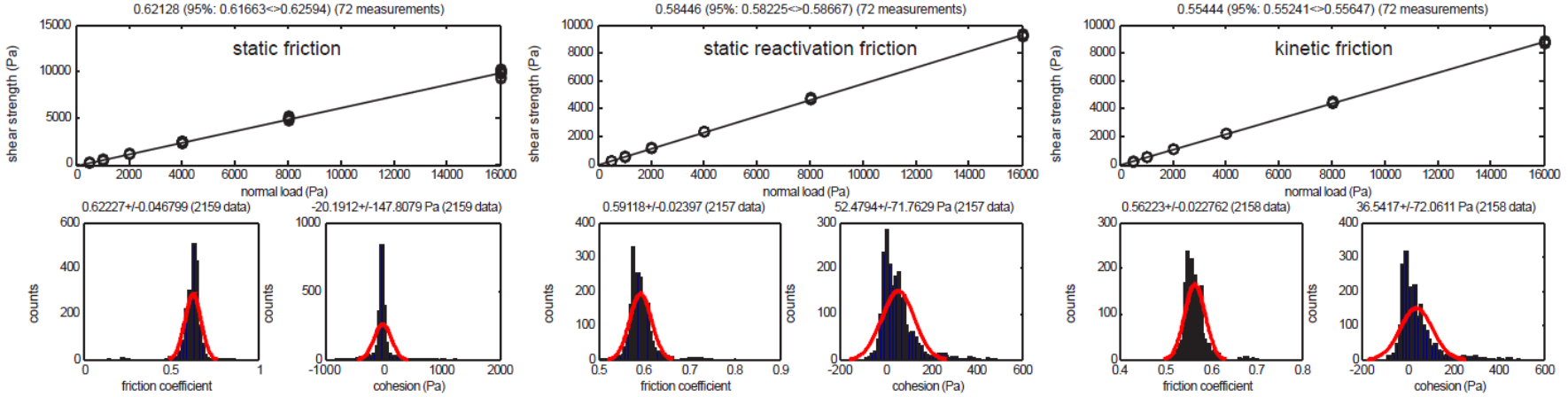

F Sand (G23) basal on glass

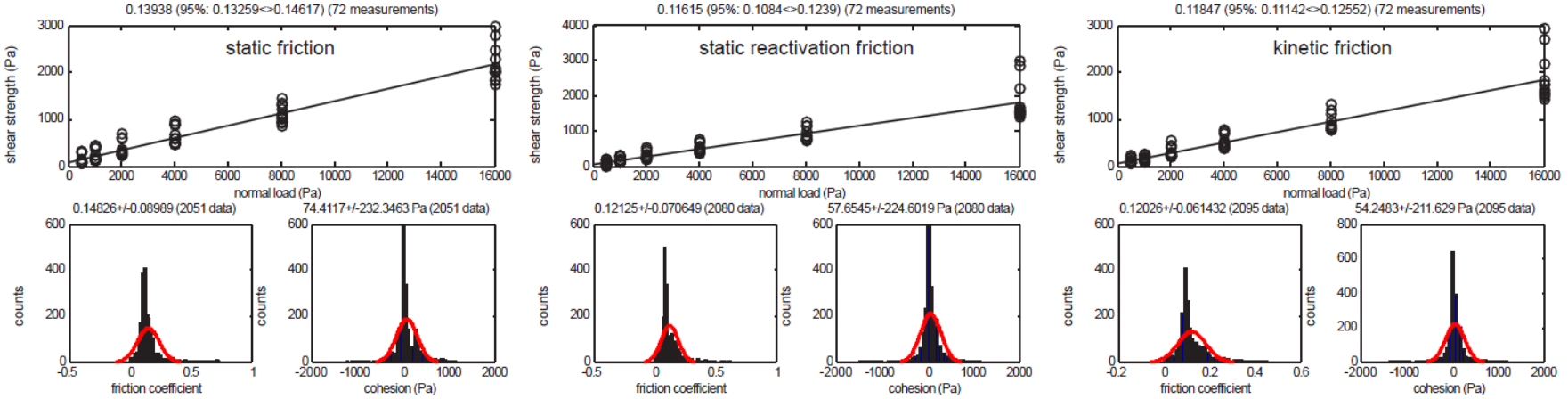

Figure A2.1- (previous three pages) Friction data set. In Each panel A-F the static, reactivated static and kinetic friction data are plotted in Mohr space (with a linear fit indicated) and as histograms of fiction coefficients and cohesion as derived from mutual two-point regression analysis. See text for explanation.

Appendix A2.2

Method: Statistical tests used in this study

1) Chi square test (χ^2 test)

The theoretical formula for this test is similar to that in Cubas et al. (2010) and calculated as follows

$$D^2 = \sum_{i=1}^{m} \frac{(O_i - E_i)^2}{E_i} \quad (2)$$

Where O= observed values, E = expected values based on the distribution and m= number of intervals from the histograms. χ^2 test as shown in Table A2.2 is calculated as follows

$$\chi^2 test = 1 - D^2 \quad (3)$$

Therefore a high χ^2 test value indicates the least difference between the theoretical values and the dataset.

The theoretical distribution functions for the different distribution types are as follows

Normal distribution

$$f(x) = \frac{1}{\sigma\sqrt{2\pi}} e^{\frac{-(x-\bar{x})^2}{2\sigma^2}} \quad (4)$$

where $\bar{x}$ = mean, σ^2 = variance

Gamma distribution

$$f(x) = \frac{x^{a-1} e^{\frac{-x}{b}}}{b^a \Gamma(a)} \quad (5)$$

where a = shape factor, b = scale factor and Γ is the Gamma function

Laplacian distribution

$$f(x) = \frac{1}{2b} e^{\left(\frac{-|x-\tilde{x}|}{b}\right)} \quad (6)$$

where $\tilde{x}$ = median, $2b^2$ = variance

2) ANOVA test

For a population consisting of measurements from several experiments, *N* is the number of experiments and n_T is the total number of measurements in all experiments. The sum, mean ($\bar{x}$), and variance (σ^2) is calculated for each experiment in the population. The degree of freedom (df), Sum of squares (SS) and Mean of squares (MS) are calculated between experiments (B) and also within each experiment (W) as follows

$$df_B = N - 1 \quad (7)$$

$$df_W = n_T - N \quad (8)$$

$$SS_B = \sum_{i=1}^{N} n_i (\bar{x}_i - \bar{x}_T)^2 \quad (9)$$

where n_i, $\bar{x}_i$ is the number of measurements and mean respectively for the i^{th} experiment, and $\bar{x}_T$ is the mean of all measurements.

$$SS_W = \sum_{\substack{i=1 \\ j=1}}^{N} \left(x_{ij} - \bar{x}_i\right)^2 \quad (10)$$

where x_{ij} is the j^{th} measurement in experiment i

$$MS = \frac{SS}{df} \quad (11)$$

$$SS_{Total} = SS_B + SS_W \quad (12)$$

$$MS_{Total} = MS_B + MS_W \quad (13)$$

As part of the ANOVA test the coefficient of determination (R^2) is calculated. R^2 is a quantitative value of how much of the variance of an observable is explained due to variation between the experiments in contrast to within experiments.

$$R^2 = \frac{SS_B}{SS_{total}} \quad (14)$$

A large R^2 value indicates that the variation is due to the experimental setup or extrinsic sources in contrast to a small R^2 indicating that the variation is within the system (Zar, 2010).

The Fisher (F) value is calculated to determine if the null hypothesis can be rejected.

$$F = \frac{MS_B}{MS_W} = \frac{Variance_B}{Variance_W} \quad (15)$$

3) Cross-correlation of fault observables.

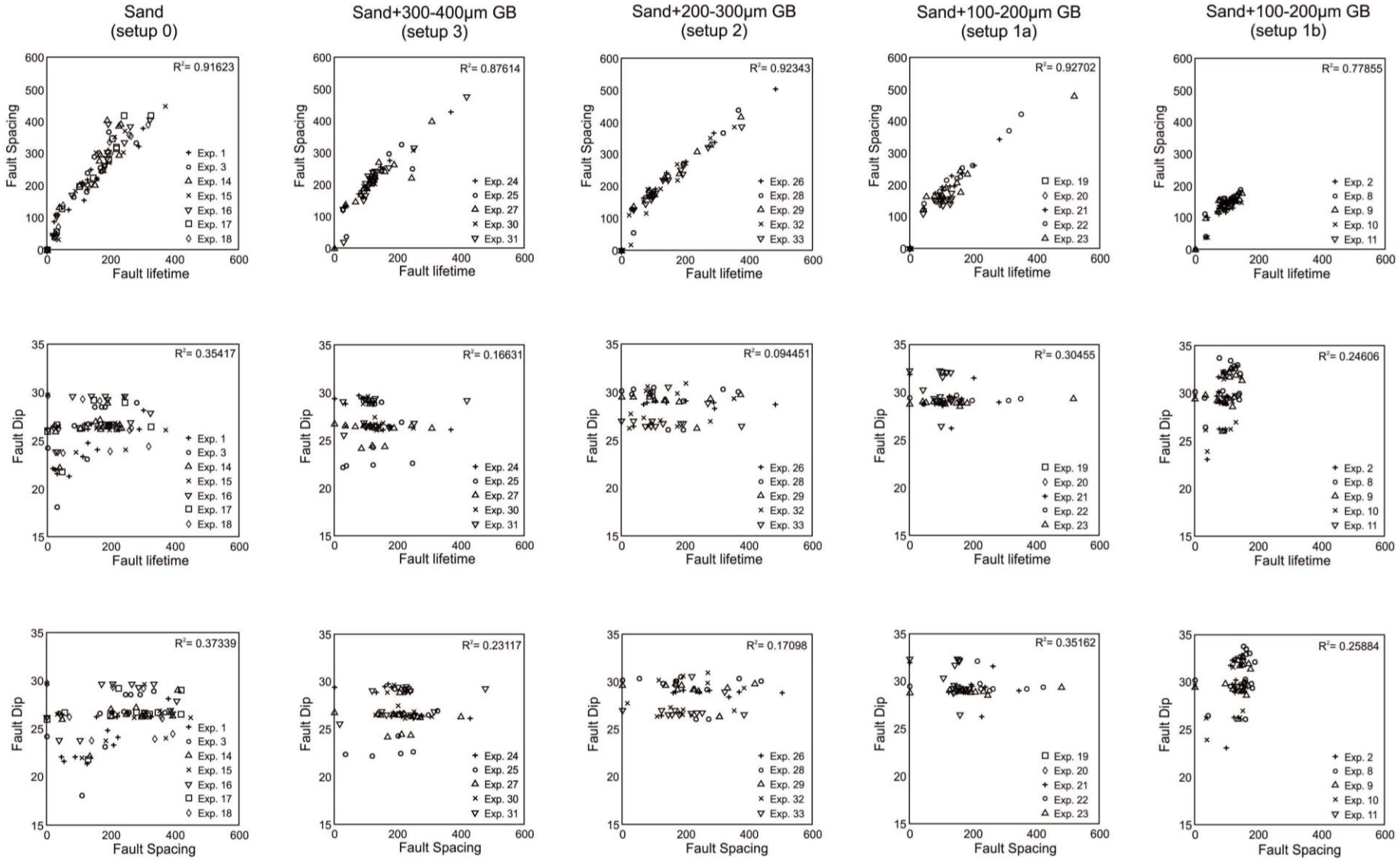

Figure A2.2.1- Graphs showing the correlation between the fault observables- fault lifetime, fault spacing and fault dip for all setups. There is a clear correlation between fault lifetime and fault spacing showing their interdependence. There is a very low correlation between fault dip and fault lifetime or spacing indicating that fault dip is independent of the latter observables.

Chapter 3

Systematics of the fault behavior in accretionary wedges.

Abstract

In wedge growth, it is the faults that accommodate the stresses acting on the wedge. Faults are responsible for the vertical and horizontal growth of the wedge. However, the temporal behavior and interaction of faults in wedge evolution is complex and not well realized. To better understand fault behavior in wedges, deformation in analogue sand wedge models are observed. The wedges differ by the basal friction (μ_{basal}) and the thickness of the basal décollement. Wedges with low μ_{basal} deform by frontal accretion while wedges with high μ_{basal} deform by underthrusting. Moreover, underthrusting can also occur in low μ_{basal} wedges if the fault plane is weakened. In the analogue experiments the weakening of the fault plane is cause by the interaction of the fault plane with the low friction material from the basal décollement. It is also observed that older faults are reactivated in low μ_{basal} wedges where there is no weakening of the fault plane. Here, it is evident that the older faults are reactivated to accommodate the stresses acting on the wedge and therefore allowing for strain partitioning. Fault formation and initial deformation is controlled by the wedge material properties and the taper. Over time, deformation along the fault is controlled by the fault plane friction and the geometry of the fault. Through fault activity, the wedge also develops its topography and overall activity. The degree of fault activity is related to the zonation of the wedge as previously realized in other studies (Lohrmann et al., 2003). This study presents different fault behaviors and the conditions they occur under. In turn, it also presents the idea that there may be varying causes to a specific fault observation.

3.1) Introduction

In an orogenic belt, fault planes are important first order structures along which deformation occurs and subsequently affects the initial geometry of an orogenic wedge. Moreover, wedge growth and fault activity are related to the principles of the Critical Taper Theory (Davis et al, 1983). The Critical Taper Theory states that a sand wedge evolves towards a critical state characterized by a critical geometry which is a function of basal and internal strength. At criticality, the wedge is at the verge of failure but no obvious internal deformation occurs. Generally two critical geometries exist, compressional and extensional, enclosing a stable geometry where the wedge is below verge of failure. In a sub-compressional or supra-extensional-critical state, the wedges have an instable geometry and internal deformation occurs in order to adjust its geometry accordingly to reach the critical taper. This adjustment to reach criticality is made by creating new faults especially if new material is added to the wedge, or reactivating old faults in order to change the length or height of the wedge respectively.

Although it is known that faults are created in the wedge to accommodate incoming material and to reach criticality, the systematics of fault behavior to achieve this is not always known. The activity of all the faults in the wedge is dependent on the forces acting on it (Cooke and Madden, 2014). However, the behavior of each fault is dependent on the wedge material properties, fault properties and fault geometry. This study presents a range of possible fault behavior from analogue accretionary sand wedge with varying basal frictions. From these sand wedges particular focus is on the fault activity and fault geometry as a 1st order structure and as a 2^{nd} order structure when it is reactivated. The change in geometry of a 1^{st} order fault during one accretionary cycle and 2^{nd} order fault-reactivated fault until the end of the wedge lifetime is also analyzed. Analogue sand wedge are also used in this study to observe the continuous change of the fault over time with the motivation to identify the conditions that cause the different types of fault behavior.

3.2) Methodology

The analogue sand wedges used for the statistical study (Chapter 2) are also used to study the kinematics of faults. Details of the experimental apparatus and setup are described in section 2.2. To recall, the different setups consisted of a sand only (no detachment layer) reference experiment (static/kinetic μ_{basal} ~0.68/0.55) and other setups where the basal properties were varied by introducing a weak décollement layer of different thickness (0.2cm vs. 0.5 cm) and made of different sizes of glass beads (100-200 μm, 200-300 μm, 300-400 μm with static/kinetic μ_{basal} increasing with size ~0.47-0.53/0.40-0.43, Appendix 2.1). The five different experimental setups that were realized are as follows:

Setup 0) 3cm layer of sand (Fig. 2.2a)
Setup 3) 2.5cm layer of sand on 0.5 cm 300-400 μm glass beads (Fig. 2.1),
Setup 2) 2.5cm layer of sand on 0.5 cm 200-300 glass beads (Fig. 2.2b),
Setup 1a) 2.5cm layer of sand on 0.5 cm 100-200 μm glass beads (Setup a) (Fig. 2.2c) and
Setup 1b) 2.8cm layer of sand on 0.2 cm 100-200 μm glass beads (Setup b) (Fig. 2.2d).

The internal coefficient of friction ($\mu_{internal}$) for all granular material used is measured in the Schulze Ring shear tester (Schulze, 1994). Table 2.1 displays the static friction for the first or primary failure or fault, static reactivation friction for the reactivation of the fault as well as the kinetic friction.

Processing of the images and vector fields produced maps of the evolving geometry and displacement of the wedge (Fig. 2.1d, 2.3b, c) thus monitoring the formation and kinematics of faults (Fig. 2.3d). To visualize the evolution of the faults in time as the wedge grows, a horizontal profile (Fig. 2.3b, c) of the velocity field is created in the middle of the granular layer at a height of 1.5 cm from the base. These velocity profiles are then assembled against each other in time and displayed as a deformation map (Fig. 2.3d, 3.1a, b, c, d, e). From the deformation maps, fault spacing and lifetime for each accretionary cycle is measured (Chapter 2). These maps highlight the occurrence of long and short lived faults in setup 3, 2 and 1a (Fig. 3.1b, c, d). In addition, the reactivation of older faults when first order faults are active is clearly visible as a change in velocity step along the profile and towards the hinterland of the wedge (Fig. 3.1d). Among all the setup, there are three distinct fault behaviors that are observed. They are as follows:
1) understhrusting in high μ_{basal} wedges (setup 0)
2) formation of alternating long and short lived faults (setup 3, 2, 1a) (Fig. 3.1 b, c, d)
3) reactivation of faults in low μ_{basal} wedges (setup 1b) (Fig.3.1e)
Therefore further analysis is performed especially on wedges from setup 0, 1a and 1b. Wedges from setup 1a are chosen since they have the same material properties for the basal décollement as setup 1b, however the only difference is the thickness of the décollement.

The high resolution optical images and processed velocity step maps are used to visually observe the behavior of the faults especially fault geometry. Observations consist of recording a) the fault dip of a new fault (1^{st} order structure) during the entire accretionary cycle and 2) the rotation of a fault plane from the end of its accretionary cycle through the life of the entire wedge. At this temporal stage the fault plane is considered a 2^{nd} order structure. The goal of this analysis is to identify favorable and unfavorable fault orientation for displacement and reactivation. When several 2^{nd} order faults are reactivated along with the 1^{st} order fault the velocity maps are used to observe the interaction of the faults. Specifically the velocity step (between the footwall and the hanging wall) for each fault is plotted over time. The optical images are also carefully examined to observe the interaction of material from the basal décollement and the fault plane especially in setup 1a. Here, attention is focused on the accumulation of glass beads that get entrained onto the fault plane changing the friction along the fault plane (Fig 3.2).

3.3) Fault and wedge behavior

The formation of faults in all accretionary wedges regardless of μ_{basal} is cyclic. During the initial formation of the wedge from a horizontal layer of sediment, faults are short lived and closely spaced. This is evident for the first three accretionary cycles in all sand wedges irrespective of μ_{basal} (Fig. 3.1). After the initial formation of the wedge the dynamics of the wedge change to either underthrusting or frontal accretion depending on the μ_{basal}. The high

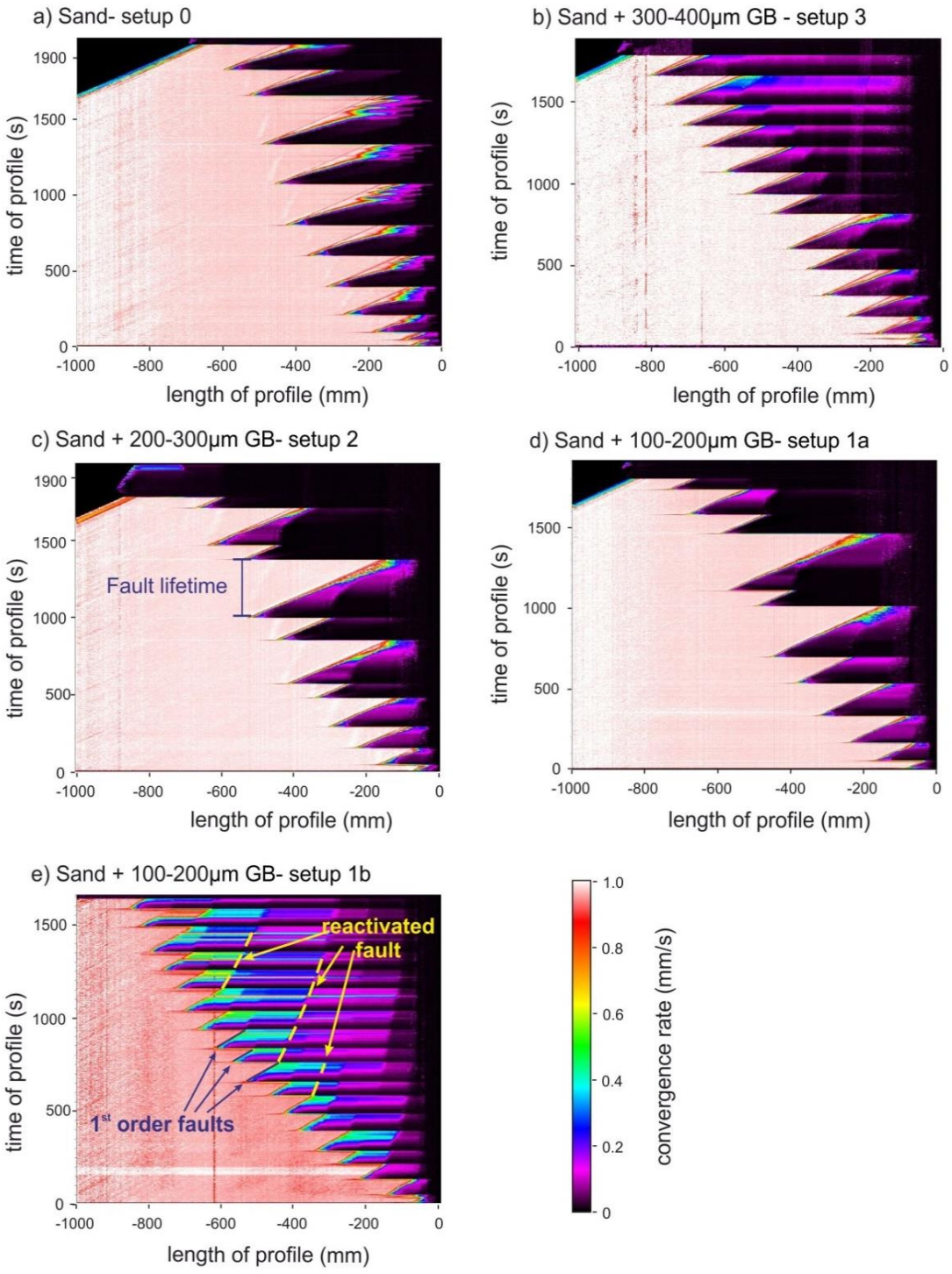

Figure 3.1- Deformation maps for a wedge with a) high μ_{basal} (setup 0), b and c) intermediate μ_{basal} (setup 3 and 2), d and e) low μ_{basal} (setup 1a and 1b). These maps are similar to those in Figure 2.3d. The difference between setup 1a and 1b is the thickness in the décollement layer. Setup 1b (thin décollement layer) has older faults that are reactivated. This is evident in the profiles that have significant velocity values in the wedge (left of the pink area) after the incoming layer. This is not evident in the other map since the other wedges do not have the occurrence of fault reactivation.

μ_{basal} wedges deform by underthrusting compared to the low μ_{basal} wedge with a thin basal décollement that deforms mainly by frontal accretion (Gutscher et al., 1996; Konstantinovskaia and Malavieille, 2005; Saha et al., 2013). As a result, the lifetime of the fault in high μ_{basal} wedges is also longer (Fig. 3.1a) than those in low μ_{basal} wedges (Fig. 3.1e).

The analogue sand wedges show a complex level of deformation over their evolution. Low μ_{basal} wedges can also display underthrusting if the fault plane is weakened. In wedges with a thicker basal décollement (Setup 3, 2 and 1a) the fault lifetime appears to be controlled by the accumulation of glass beads and the eventual entrainment of the glass beads onto the fault plane. When the glass beads have formed a significant layer on the fault plane, it allows the fault to underthrusting the wedge. However this occurs at alternating accretionary cycles and as a result produces alternating long and short fault lifetimes.

3.4) Discussion

3.4.1) Fault orientation

Fault orientation is an important parameter that changes over the lifetime of an accretionary cycle and then over the lifetime of the wedge. In the beginning of each accretionary cycle as strain localizes the fault dip is dependent on the μ_{basal} and $\mu_{internal}$. In high μ_{basal} wedges the dip of the fault is steeper and decreases with decreasing μ_{basal} (see Buiter, 2012 and reference therein). After the fault plane is formed the dip of the fault steepens. During this time the pop up caused by the new fault and the backthrust is uplifted. As the fault begins to thrust under the wedge and displacement along the fault plane increases, the fault plane begins to rotate to shallower angles. This is observed in all three setups regardless of the initial conditions (Fig 3.3a, b, c). The shearing of the incoming layer caused by movement at the surface of the décollement relative to the rest of the layer causes the shallowing of the fault plane. In the high μ_{basal} wedge, the fault plane later begins to steepen (after 317 mm of convergence- Fig. 3.3a). Here, the fault plane has reached near the back stop and is affected by the lack of space. The steepening of the fault is merely an effect of the experimental setup.

When a new fault forms and begins to underthrust the wedge, the fault dip of the former fault first steepens. As the new fault continues to underthrust (high μ_{basal} wedges) and is beneath more than half of the former fault the dip of this fault shallows (Fig. 3.4a). Figure 3.4a is a record of the fault plane steepening at the beginning of an accretionary cycle and then shallowing at the end. Towards the end of the experiment, the fault plane further steepens as it is in the hinterland and pushes against the backstop of the experimental setup. Wedges that constantly grow by frontal accretion (low μ_{basal} wedges) show rotation of the older fault to steep angles as they become part of the hinterland (Fig. 3.4b, c). In contrast faults in wedges that grow with underthrusting tend to uplift the older faults. Therefore, they are stacked underneath each other with the relative age of the oldest fault on top of the wedge. Since frontal accretion occurs in low μ_{basal} wedges, steepened faults are seen in this wedge. Figure 3.4b shows the geometry of a fault from setup 1a. Here the shallowing at the end is caused by the underthrusting of a long lived fault. When the fault is part of the hinterland, there is no activity in this part of the wedge after 16.7cm of shortening and therefore the fault plane

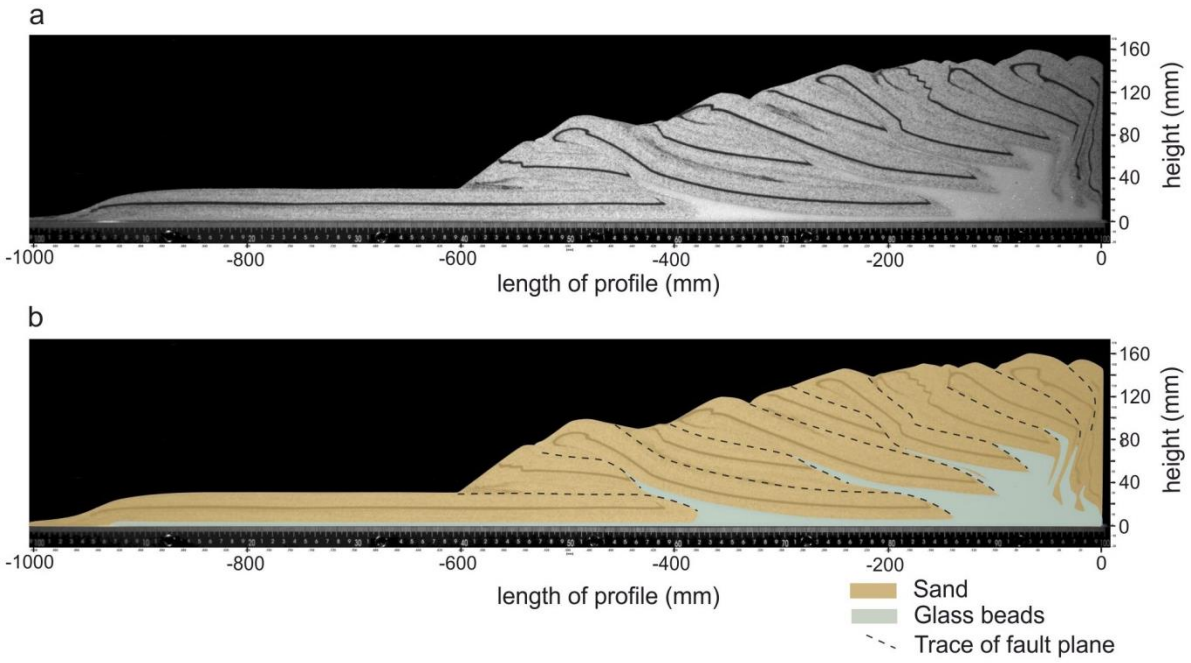

Figure 3.2- a) calibrated cross-sectional image of the wedge from setup 2. b) Colored overlay on the calibrated image to show the position of glass beads (200 -300μm) that moved from the basal décollement into the wedge along the fault planes (dashed lines). This wedge has undergone 170cm of shortening.

geometry is constant. A fault in setup 1b also shows steepening of the fault plane, however it shallows as it reaches towards the hinterland. Moments of stable fault dip between accretionary cycles is when it is not reactivated. At the beginning of the accretionary cycle the front of the fault plane is also first uplifted (steepening the plane) and then it shallows similar to the fault planes in Figure 3.4a- high μ_{basal} wedge. However here it occurs during smaller time intervals. As a 1st order fault, the dip of the fault is controlled by the frictional material properties of the wedge, however as a 2nd order structure the fault geometry is controlled by a new fault and the dynamics of the wedge.

3.4.2) Fault activity

The initiation of fault formation is controlled by the critical taper (Davis et al., 1983). Wedges with high μ_{basal} have steeper slopes created by underthrusting of long thrust sheets that allows the wedge to build in height. Wedges with is low μ_{basal} have shallower slopes grow by frontal accretion primarily in length by short-lived and narrowly spaced faults instead of underthrusting. The first three faults in all wedges regardless of μ_{basal} are short lived and closely spaced to build the wedge from a horizontal layer of sand.

The shape of the wedge is due to different styles of deformation. Underthrusting and fault reactivation cause uplift and raise the height of the wedge while frontal accretion lengthens the wedge. Underthrusting is also used when there is a change in

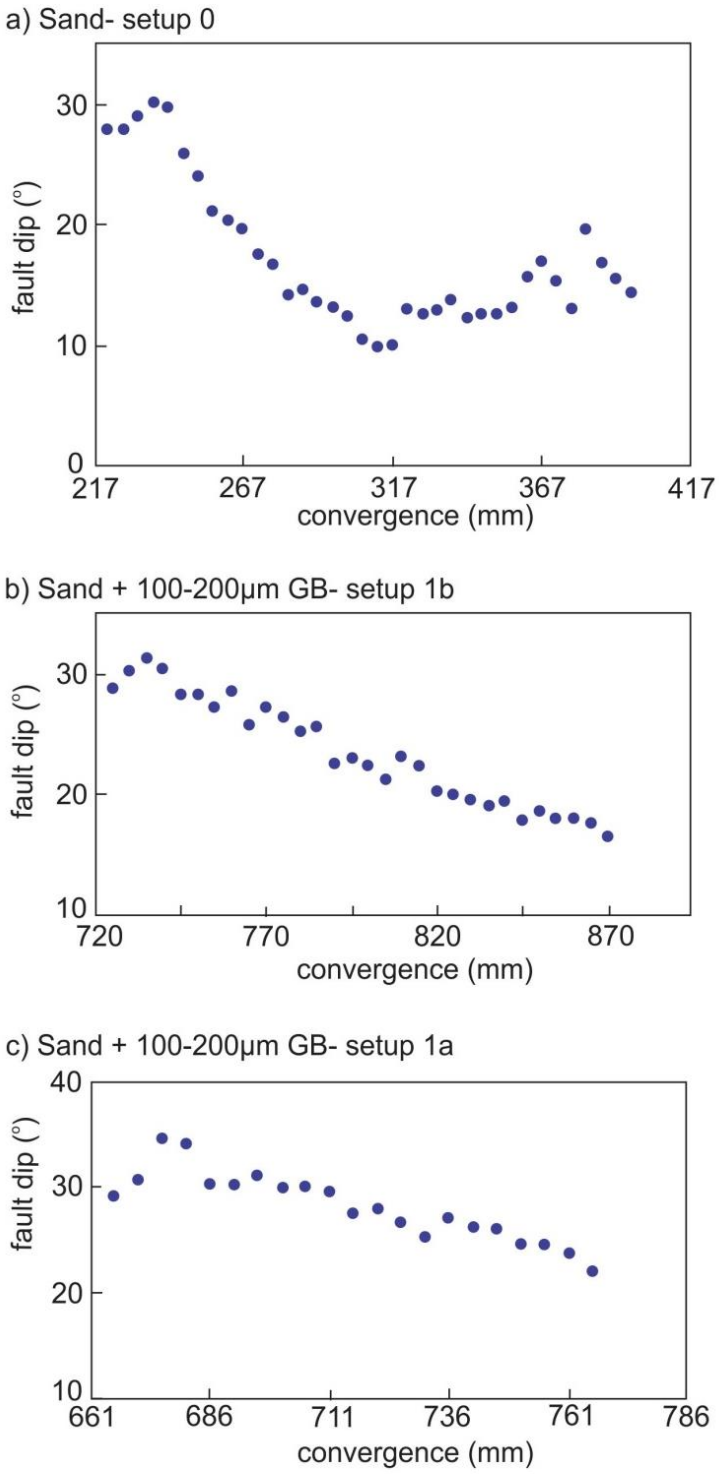

Figure 3.3- Fault dip of a first order fault during one accretionary cycle in wedges with a) high μ_{basal} (setup 0), b) low μ_{basal} (setup 1a) with no occurrence of fault reactivation and c) low μ_{basal} with the occurrence of fault reactivation.

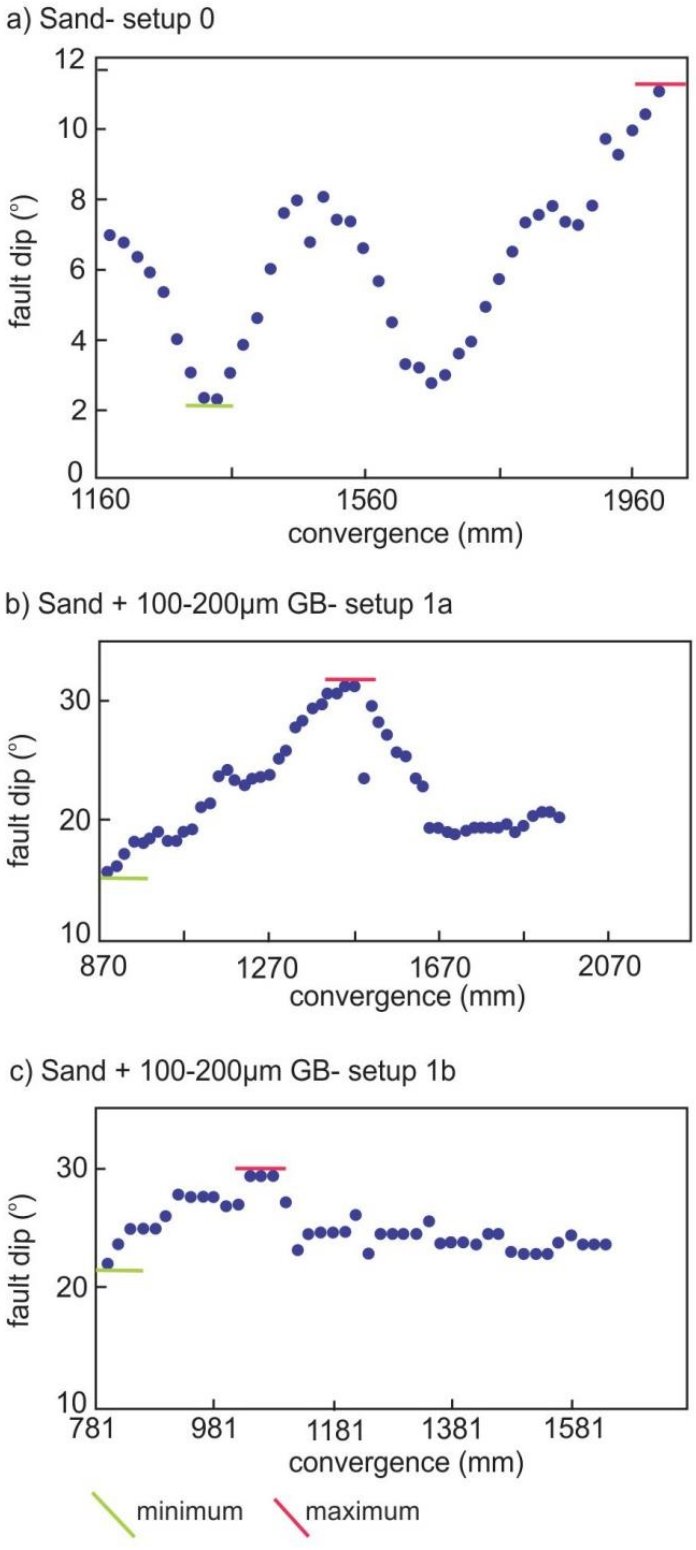

Figure 3.4- Fault dip of a 2nd order fault at the end of its accretionary cycle to the end of the experiment for a) high μ_{basal} (setup 0), b) low μ_{basal} (setup 1a) with no occurrence of fault reactivation and c) low μ_{basal} with the occurrence of fault reactivation. Minimum and maximum fault dip values are only for the particular fault in each wedge.

the friction along the fault plane. In the analogue models this is caused by the entrainment of low friction material onto the fault plane from thick décollement layers. The addition of a different material as a décollement layer and the thickness of the layer inherently introduces a degree of complexity and a change in the wedge dynamics. In this case, it is not only high μ_{basal}, but also the weakening of the fault plane in low μ_{basal} that uses underthrusting as the deformation mechanism. Here the control on the fault lifetime has changed from μ_{basal} to friction along the fault plane. This behavior is observed in wedges with a thick décollement (Setup 3, 2 and 1a) and the style of deformation changes from frontal accretion for the first few faults to underthrusting. Such a setup is analogous to natural salt décollements or other low friction décollements that are fragile and can interact with the overlying material (Davis and Engelder, 1985). In the analogue experiments, the entrainment of glass beads only happens when there is an accumulation of the material (Fig. 3.2). It takes approximately two fault lifetimes to accumulate sufficient glass beads for interaction with the fault plane thus producing a pattern of alternating short and long lived faults.

Another mechanism that causes uplift is the reactivation of older faults (Fig. 3.5). Reactivation starts systematically in the middle of an accretionary cycle and continues till the end of the cycle. In this series of analogue experiments, fault reactivation is only seen in wedges with low μ_{basal} and thin décollement layers that do not have a chance to interact with the fault plane or affect the friction along the fault plane. Here fault reactivation occurs to accommodate the incoming material and stresses that cannot be completely accommodated by the 1st order new fault. In this case fault reactivation is controlled by the μ_{basal}. As a result the strain is partitioned between two or more faults (Fig. 3.6). Figure 3.6 shows the velocity step across a 1st order fault and three reactivated faults. The velocity step is the difference in velocity between the footwall and hanging wall of each fault and is measured along a horizontal profile line (Fig. 3.6a). The sum of all the velocity steps for each time step is equivalent to the convergence velocity of the incoming layer (Fig. 3.6b). As displacement along the 1st order fault decrease the displacement along the three 2nd order faults increase. Interestingly here all three 2nd order fault become active and it is fault 3 that has a higher displacement than fault 2. It is expected that fault 2, closest to the 1st order fault, would show more displacement since it is consecutively before the 1st order fault. In this wedge there appears to be no systematic timing of reactivation or amount of displacement based on location. Total displacement values in both the horizontal and vertical component along the same horizontal profile line show peaks at the end of the accretionary cycle and during fault reactivation (Fig. 3.7a, b). This indicates that the amount of displacement during fault reactivation is not constant. Additionally the vertical component appears to have a cut-off while the horizontal component increases with shortening.

For the faults to be reactivated they need to have a geometry or fault dip that is favorable for reactivation. Fault geometry in relation with principal stresses on a Mohr circle show that the dip of the 2nd order fault in high μ_{basal} wedges (although the minimum fault dip is very shallow- Fig. 3.8a) and low μ_{basal} wedges (Fig. 3.8b, c) are within a favorable range to be reactivated. Nonetheless, faults in the wedges from setup 1b are not reactivated since deformation is favored to continue with the 1st order fault due to its weakened fault plane.

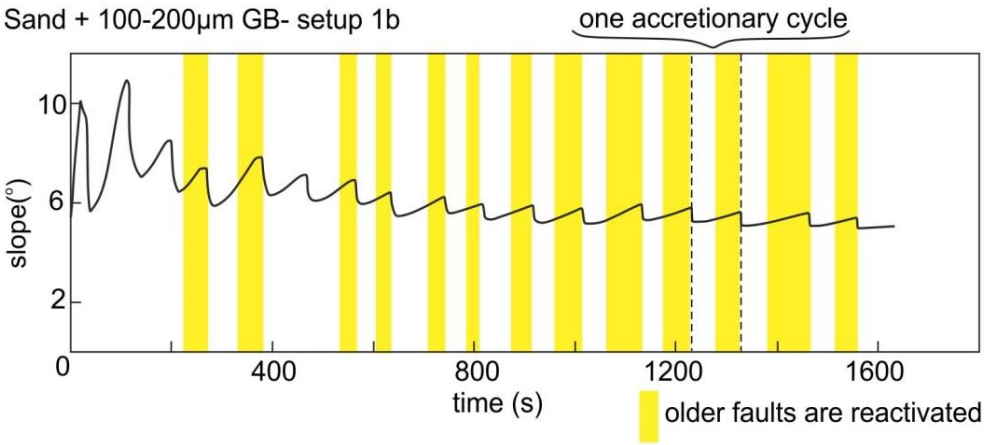

Figure 3.5- Uplift and increase in the slope of the wedge (during an accretionary cycle) caused by fault reactivation.

Therefore, it appears that 2nd order faults are only reactivated as a support to the 1st order faults. Stresses acting on the fault also need to be high enough to cause fault reactivation. After the formation of a 1st order fault stresses are low and increase as the load on the fault increases. This may be a reason why fault reactivation begins in the middle of an accretionary cycle (Fig. 3.5).

3.4.3) Effect of fault behavior on wedge topography

It is the fault behavior that primarily shapes the topography of the wedge. As mentioned earlier, underthrusting and fault reactivation of fault causes uplift and vertical growth of wedge while frontal accretion causes lengthening of the wedge. Of course the deformation mechanism is dependent on the frictional properties of the materials that make up the wedge and the critical taper that the wedge can sustain. In addition, the varying fault activity in different parts of the wedge create a zonation of the wedge. According to Lohrmann et al., 2003 the wedge can be divided into three zones (Fig.3.9a). 1) The Frontal deformation zone (FDZ), 2) the Frontal imbricate zone (FIZ) and the Internal Accumulation zone (IAZ). The FDZ consist of only the new fault and the taper of this part of the wedge is steepest. The FIZ consist of older faults that may be reactivated. The FIZ has a slightly shallower taper than the FDZ. When the FIZ is underthrusted by a new fault, the wedge taper of this zone initially shallows and then steepen as the new thrust continues to underthrust the entire zone. Lastly the IAZ is a zone that is not active and has the shallowest taper and is almost plateau-like. In this zone the faults are usually rotated to a steep angle that is not favorable to accommodate slip. In Fig. 3.9b shows the zonation of a wedge with low μ_{basal}. For comparison, wedges with high μ_{basal} in this series of experiments cannot be divided into zones in the same way since the wedge as consistently the same slope (Fig. 2.2a). It may be the case that high μ_{basal} wedges need a lot more shortening to occur before they can be divided into zones. It may be the case that it is the wedge material properties that control the timing of wedge zonation.

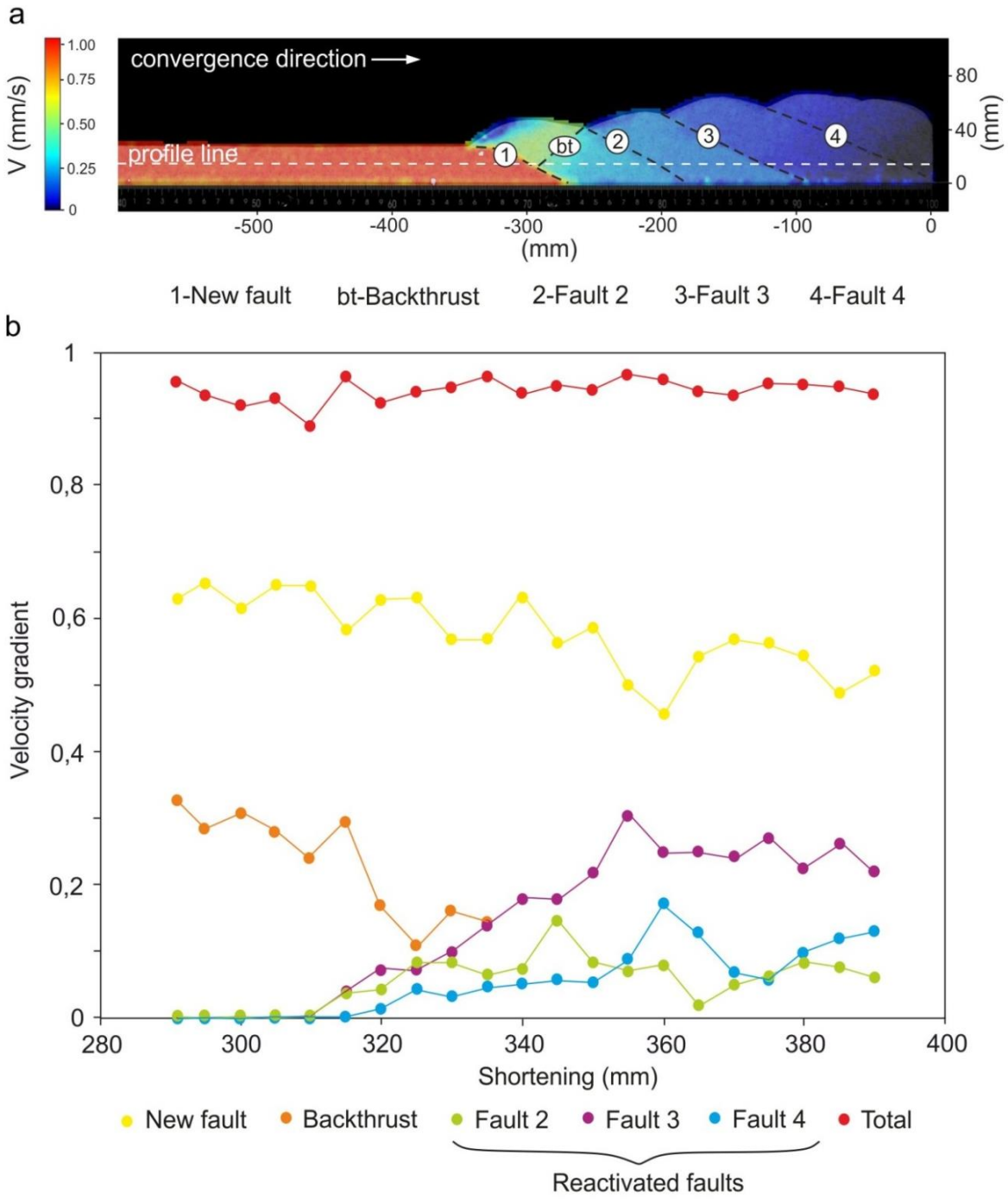

Figure 3.6- The partitioning of strain when a 1st order fault and three older faults are reactivated. a) Cross-section of the wedge showing the method used to derive the velocity step for each fault. The velocity step is the difference in velocity between the footwall and hanging wall of the fault, along the profile line. This image represents 33.3cm of shortening. b) Plot showing the change in the velocity step for each fault measured at every 5mm of convergence. The values are for a timespan of one accretionary cycle. The total value (red) represents the sum of all the velocity steps for all the faults.

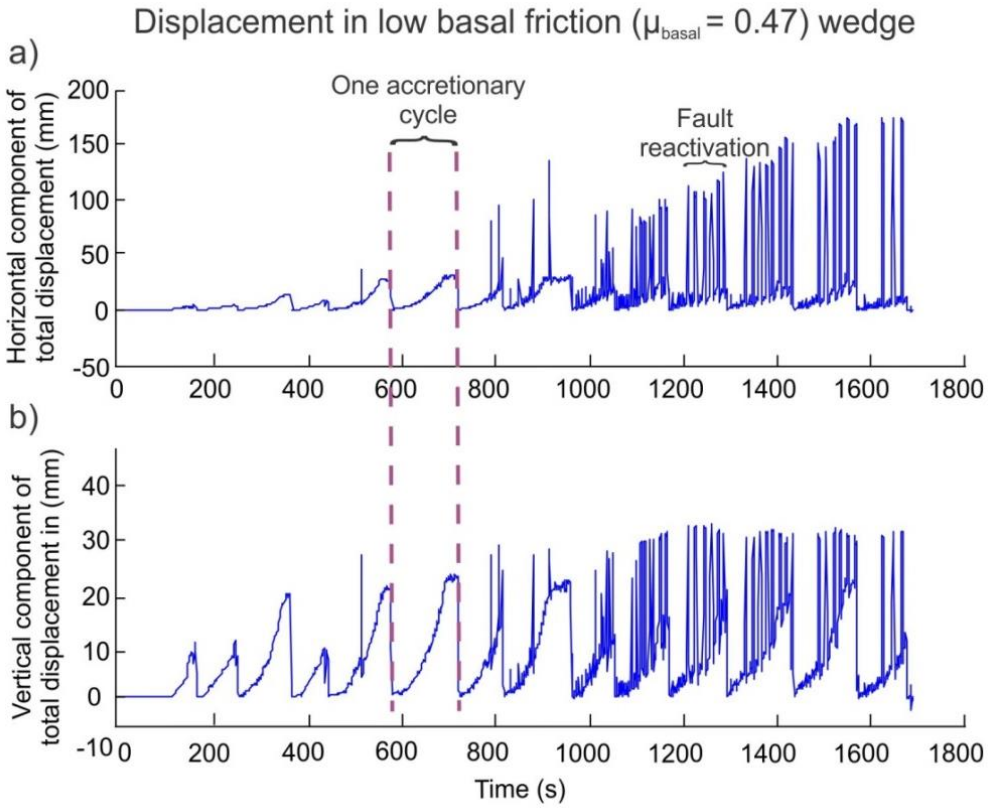

Figure 3.7-These plots represent the sum of displacement for all vectors along the profile line (Fig. 3.6a). The plots highlight the discontinuous reactivation of faults evident from peaks in the total a) horizontal and b) vertical component of displacement.

3.5) Conclusion and implication

The analogue wedges present a range of fault behaviors, some of which are dependent on the material properties of the wedge and others the properties of the faults itself. Underthrusting is related to high basal friction wedges as well as to the weakening of the fault plane in low basal friction wedges. The weakening of the fault plane can be caused by the entrainment of low friction material from the basal décollement. In this case the weakening of the fault plane occurs over time and can be related to the age of the wedge. In a network of faults, 1st order faults are active along with one or more 2nd order faults. In this case, the two or more reactivated faults are active at the same time to accommodate the stresses acting on the wedge by strain partitioning.

Implications of this study show that for each observation of fault behavior there may be one or more causes. For example underthrusting is due to high μ_{basal} or at later stage of wedge development can also be found in wedges with low μ_{basal} and weakened fault planes. To distinguish between both these cases, other observables like the fault plane friction is helpful.

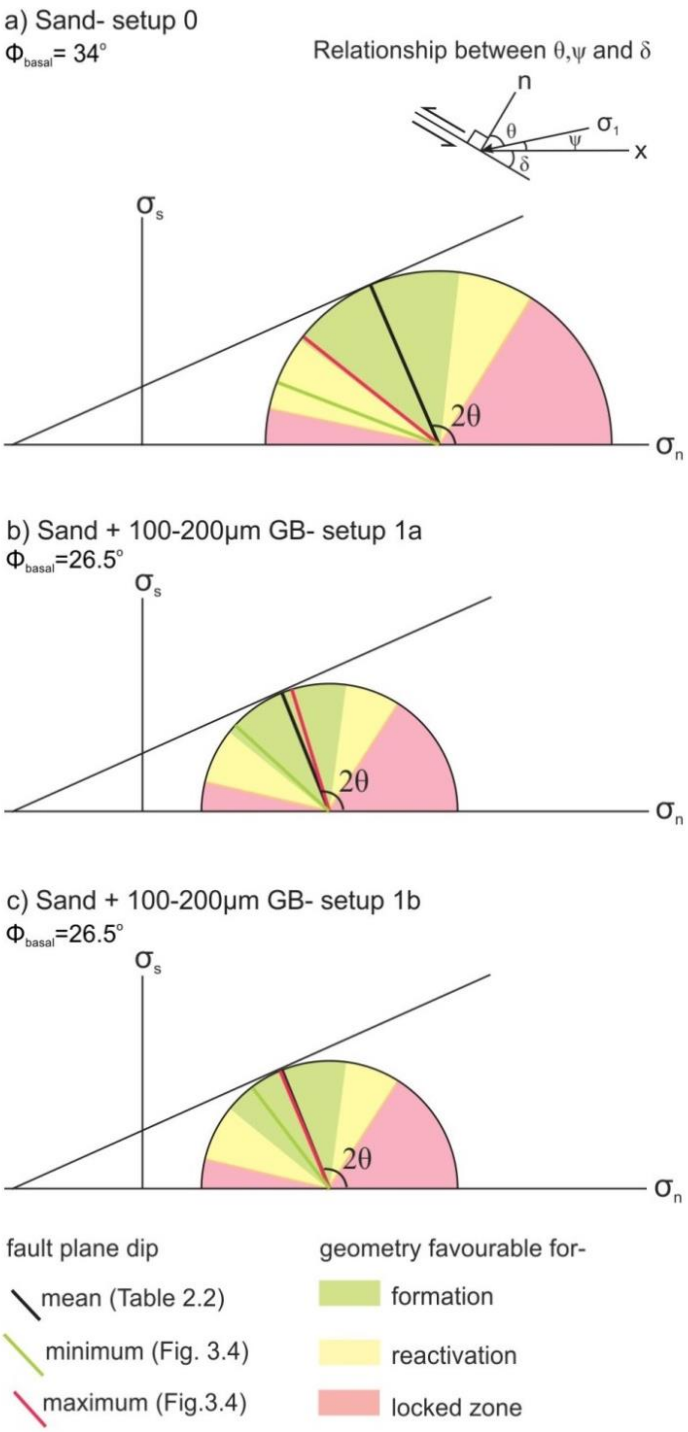

Figure 3.8- Mohr circle constructed to show the fault dip of 2nd order faults in relation to favorable geometries for displacement. Fault dip values for a) high μ_{basal} (setup 0), b) low μ_{basal} (setup 1a) with no occurrence of fault reactivation and c) low μ_{basal} with the occurrence of fault reactivation, are taken from Fig. 3.4. The Mohr circles are constructed using experimental data (Table 3.1)

setup	α[1]	ϕ[2]	ψ[3]	fault dip	2θ[4]
0	17.0	34.0	7.5	26.0[i]	113.0
0	17.0	32.1	8.2	2.4[ii]	158.9
0	17.0	32.1	8,2	11.1[iii]	141.5
1a	12.0	34.0	4,8	29.0[i]	112.2
1a	12.0	32.1	5.5	15.6[ii]	137.7
1a	12.0	32.1	5.5	30.9[iii]	107.2
1b	9.7	34.0	3,8	30.0[i]	112.2
1b	9.7	32.1	4.3	21.9[ii]	127.4
1b	9.7	32.1	4.3	29.2[iii]	112.8

[1] mean dip (from Table 2.2)
[2] $\phi = 34.0^{o}$ ($\mu_{internal}$ =0.68) and 32.1^{o} ($\mu_{internal}$ =0.62) refers to the static and static reactivation coefficient of frictions respectively
[3] $\psi = 0.5 \arcsin (\sin \alpha / \sin \phi) - 0.5 \alpha$ (Dahlen et al., 1984)
[4] $2\theta = 2 (90- \psi-$ fault dip)
i- mean value (from Table 2.2) ii- minimum value iii- maximum value (from figure 3.4)

Table 3.1- Values used to calculate 2θ that is plotted on Figure 3.8 for a wedge with high μ_{basal} (setup 0), low μ_{basal} with no fault reactivation (setup 1a) and low μ_{basal} with fault reactivation (setup 1b). The static coefficient of friction is used with the mean fault dip because these are 1st order faults. The static reactivation coefficient of friction is used for reactivated or 2nd order faults.

The IAZ of the wedge shows little deformation, however it is unknown whether continued shortening of a natural wedge would eventually activate the faults in this part of the wedge even though they are at very steep geometries. This idea also reflects on the fact that to completely understand the fault and wedge pattern of deformation analogue experiments should consist of as much shortening and as many accretionary cycles as possible. Since fault activity is related to the topography and overall activity of the wedge, perhaps natural wedges can also be divided into wedges according to the slip rates of the faults.

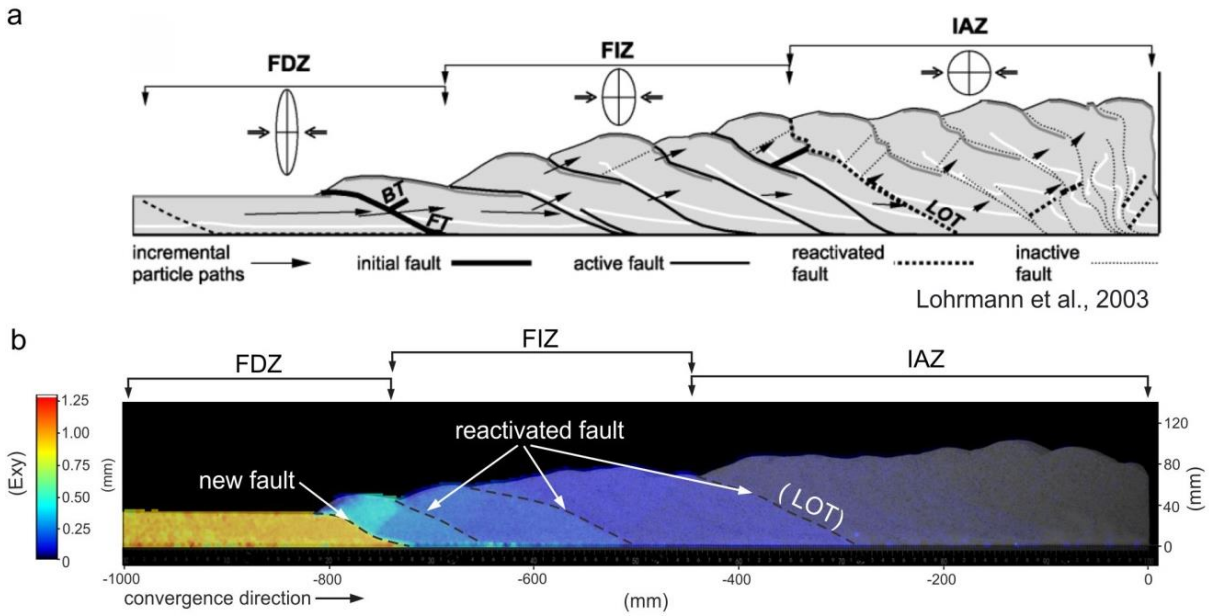

Figure 3.9- a) Wedge zonation according to Lohrmann et al. (2003) showing the frontal deformation zone (FDZ), the frontal imbrication zone (FIZ) and the internal accumulation zone (IAZ). LOT indicates the leading out-of-sequence thrust. b) Application of wedge zonation to an analogue wedge from setup 1b. The different zones are clearly distinguishable based on the fault activity and the slope of the wedge.

References

Buiter, S.J.H., 2012. A review of brittle compressional wedge models. Tectonophysics 530 - 531, 1-17. doi:10.1016/j.tecto.2011.12.018

Cooke, M.L., Madden, E. H., 2014, Is the Earth lazy? A review of work minimization in fault evolution: Journal of Structural Geology, v. 66, p. 334-346.

Dahlen, F.A., 1984. Noncohesive Critical Coulomb Wedges: An Exact Solution. Journal of Geophysical Research 89 (B12), 10,125-10,133.

Davis, D., Suppe, J., Dahlen, F.A., 1983. Mechanics of Fold and Thrust Belts and Accretionary Wedges. Journal of Geophysical Research 88 (B2), 1153-1172.

Davis, D., Engelder, T., 1985. The role of salt in fold-and-thrust belts. Tectonophysics 119(1), 67-88.

Gutscher, M-A., Kukowski, N., Malavieille, J., Lallemand, S., 1996. Cyclical behavior of thrust wedges: Insights from high basal friction sandbox experiments. Geology 24(2), 135-138.

Konstantinovskaia E., Malavieille, J., 2005. Erosion and exhumation in accretionary orogens: Experimental and geological approaches. Geochemistry, Geophysics, Geosystems 6(2), doi:10.1029/2004GC000794.

Lohrmann, J., Kukowski, N., Adam, J., Oncken, O., 2003. The impact of analogue material properties on the geometry, kinematics, and dynamics of convergent sand wedges. Journal of Structural Geology 25, 1691-1711.

Saha, P., Bose, S., Mandal, N., 2013. Varying frontal thrust spacing in mono-vergent wedges: An insight from analogue models. Journal of Earth System Science 122 (3), 699-714.

Chapter 4

Smart or beautiful? Accretionary wedge evolution seen as a competition between minimum work and critical taper.

Abstract

In order to understand orogenic and accretionary wedge growth two theories, the critical taper theory and the minimum work concept, gained popularity in the last decade. However, both theories rely on strong simplifying assumptions and describe rather statistically snapshots of natural wedge evolution. The latter is characterized by thrust formation and reactivation associated with fluctuations of geometrical and mechanical properties and therefore transient deviations from the ideal "smart" (minimum work) and "beautiful" (critical taper) state given as ideal endmembers of the two theories, respectively. To test the applicability and interplay of both concepts, an analogue (sand) accretionary wedge that grows with varying styles of deformation i.e. frontal accretion and underthrusting is compared to an ideal self-similar growing analytical wedge which grows by incorporating material quasi-homogenously to its base at a constant critical taper at minimum work. The deviation in geometry and the work done through accretion cycles of the "real" analogue wedge in relation to the ideal self-similar wedge (SSW) is analyzed at high spatio-temporal resolution. At the beginning of every accretionary cycle the analogue wedge transitions from a critical taper wedge (in particular from the static friction envelope to the kinetic friction envelope) to a minimum work wedge. With increasing number of accretion cycles deviations decrease, i.e. the wedge progresses towards an ideal state that is a unification of the two models. Overall the analysis shows that deformation in accretionary wedges is a competition between minimizing work and reaching the critical taper. Importantly for analyzing natural wedges using the two theories is therefore the maturation stage (i.e. number of thrust slices) and the accretionary cycle stage. According to our analysis, CT is only valid at the beginning of an accretionary cycle while MW applies at late stages of an accretionary cycle. The more mature a wedge is, the smaller the deviations from CT and MW at sub-accretionary cycle stage. Ignoring the latter would lead e.g. to overestimate of basal friction.

This study has been submitted for publication as follow-
Santimano, T., Rosenau, M., Oncken, O., 2015, Smart or beautiful? Accretionary wedge evolution seen as a competition between minimum work and critical taper- In Review Geology

4.1) Introduction

Deformation in accretionary wedges has been described by two theories: The Critical taper theory (CTT) (Davis et al., 1983) and the minimum work concept (MWC) (Mitra and Boyer, 1986; Masek & Duncan, 1998). Both are applied in nature to make predictions of deformation pattern and physical properties (e.g. Fagereng, 2011; Cubas et al., 2013: von Hagke et al., 2014). CTT is based on force balance and predicts the ideal ("beautiful") shape- critical taper (CT) of an accretionary wedge. Physical parameters that particularly determine the shape of (dry) accretionary wedges are the basal coefficient of friction (μ_{basal}) of the décollement layer, the internal coefficient of friction ($\mu_{internal}$) of the wedge and the internal kinematics (Davis et al., 1983; Lohrmann et al., 2003) (Fig. 4.1A). To maintain the ideal state, the wedge has to grow self-similarly without changes to the above physical properties. However, the idea of self-similar growth of the wedge does not take into account strain weakening or the temporal cycle of fault formation that is seen in natural orogens and analogue wedges. In sand wedge models strain weakening and the deformation along faults is important to reach the critical taper (preferred geometry) and thus crucial in defining the topography of the wedge (Lohrmann et al., 2003; Hoth et al., 2007). Slip along faults can be predicted by MWC which states that deformation is accommodated in an energetically "smart" way by faults that will propagate in the direction that allow to minimize external work (due to the addition of new material) acting on the wedge (Del Castello and Cooke, 2007; Cooke and Madden, 2014; Cubas et al., 2008).

Both the CTT and the MWC are based on the balancing of forces acting on and within the wedge. The CTT focuses on the geometry and critical taper or slope that the wedge can sustain, whereas the MWC focuses on the energy efficiency of the faults in the wedge. In general, faults in natural and analogue wedges transition from frontal accretion when a new fault is formed to underthrusting, thus changing wedge topography. Therefore, wedges are not always at critical taper geometry but transition between states of being at criticality (Lohrmann et al., 2003; Simpson, 2011; Wang and Hu, 2006). Theoretically criticality is a state when the wedge has a taper that will fail with any perturbation like the addition of new material. This geometry is based on the above mentioned physical properties considering that all of them are constant over time. This also implies that the wedge is homogenous and there is no change in the properties as it evolves, which is not the case in natural wedges. The external work acting on the wedge is also not constant. The MWC determines the energy efficient activity of the fault accordingly to reduce external work (Del Castello and Cooke, 2007). Therefore, the minimum work done over time can vary. In a self-similarly growing wedge work would at the same time be minimized by continuous sliding on the base. Such a wedge would be in a state which is smart and beautiful at the same time but such a state is clearly not feasible in nature because of the complexity of natural wedges. Here, the impact of such imperfectness is studied by means of analogue and analytical modelling in order to describe quantitatively the deviations from a hypothetical ideal state.

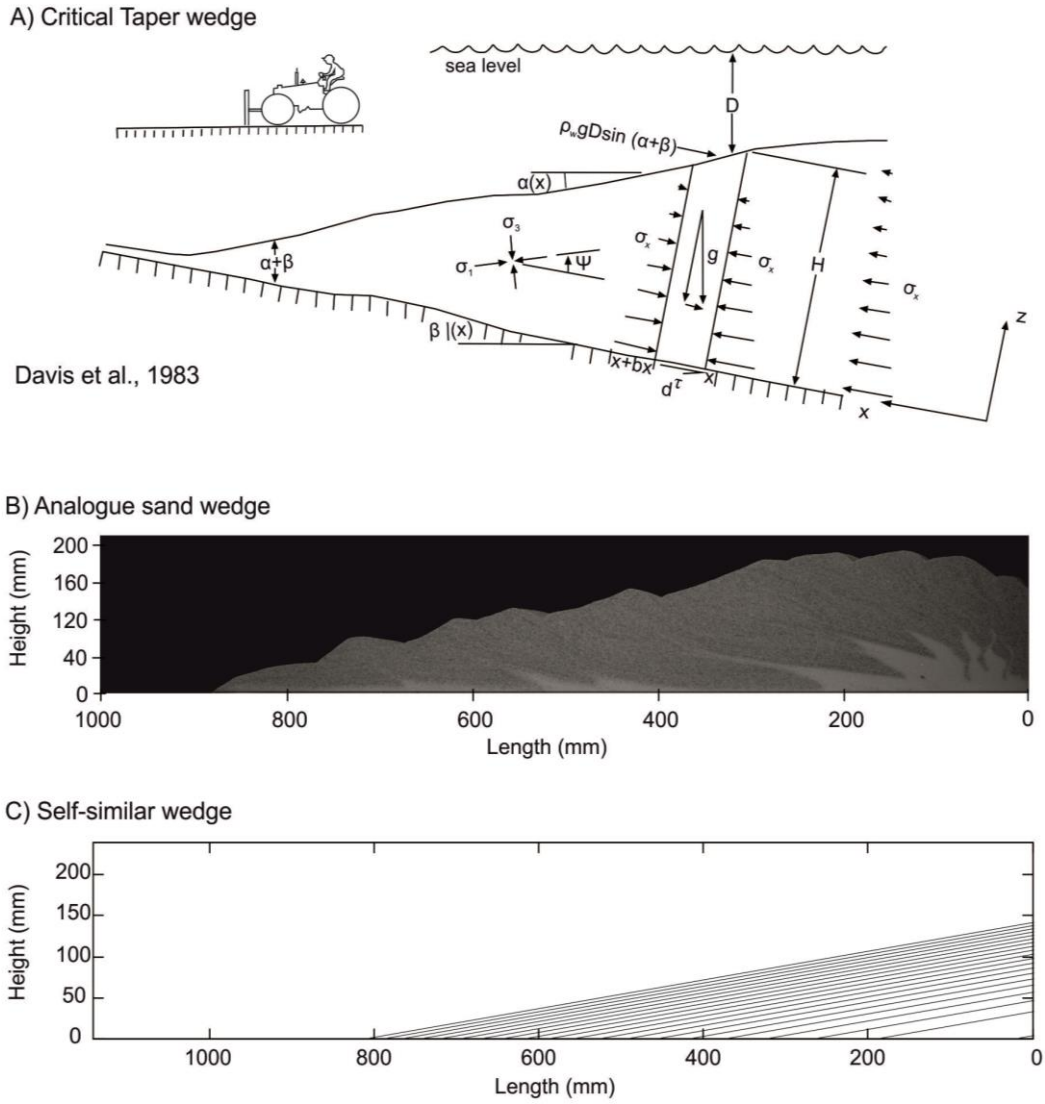

Figure 4.1- (A) Critical taper wedge after Davis et al., (1983) is an analytical approach that explains the geometry of the wedge based on the physical properties of the brittle material. (B) Analogue sand wedge with a basal décollement made of glass beads has an overall wedge shape and an irregular surface topography due to varying styles of deformation. (C) The analytical wedge has a self-similar geometry and maintains a constant surface slope as it grows.

To better understand how each concept relates to wedge evolution, observed geometrical evolution and work history of the analogue wedge (Fig. 4.1B) is compared to analytical solutions of a self-similarly growing, always critically tapered and minimum work wedge (Fig. 4.1C). A comparison of the analogue wedge to the theoretical taper angles based on static (first order failure) and kinetic (sliding along the fault plane) $\mu_{interal}$ is also realized. I describe geometry changes and the work done especially over the time evolution of the wedge through accretion cycles is described and hypothesize that there is a competition between minimizing work and reaching the critical taper that controls the evolution of accretionary wedges. Only with this knowledge, the applicability of the CTT and MWC on natural wedges can be judged.

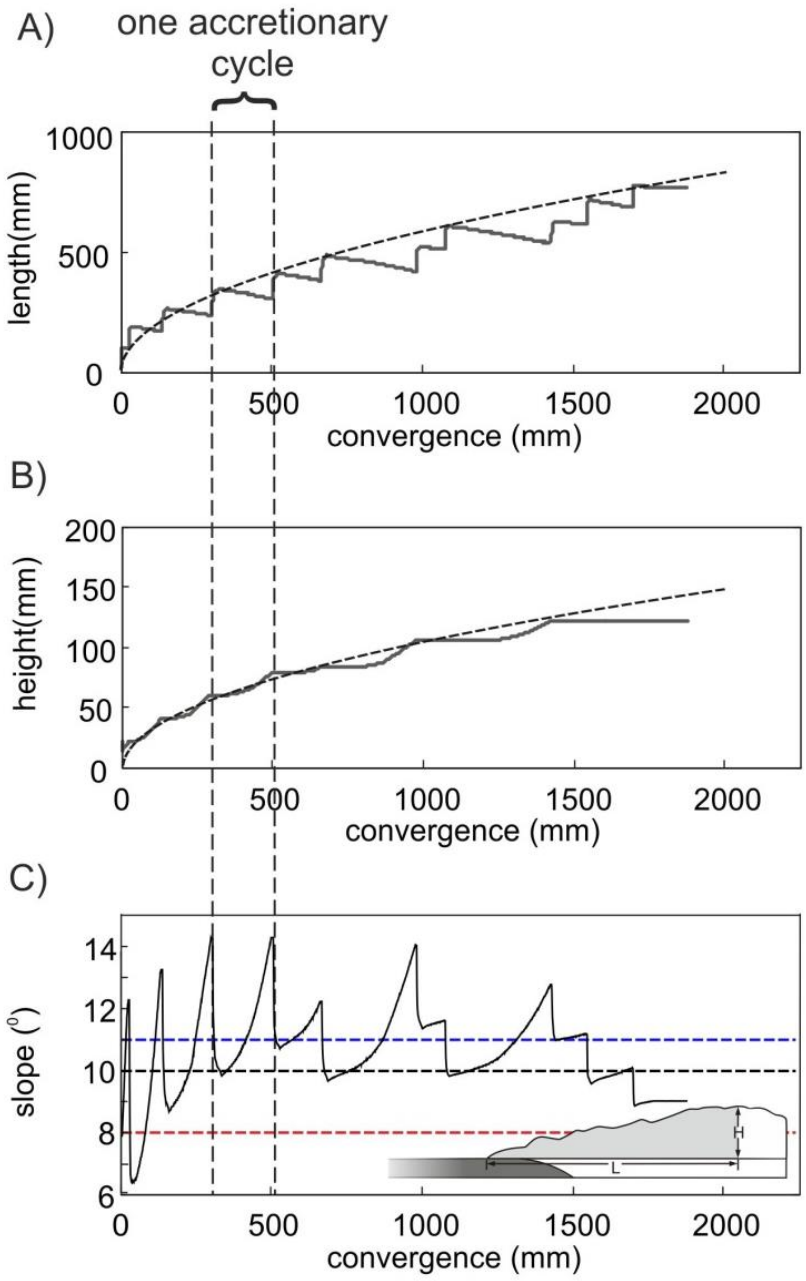

Figure 4.2- (A) Length (B) height and (C) slope of the analogue wedge over time. Dashed lines indicate the critical taper slope based on the static $\mu_{internal}$ (red) kinetic $\mu_{internal}$ (blue) and average slope from all experiments with the same setup (black). The wedge in (C) indicates the length (L) and height (H) of the wedge that is used to calculate the slope. Therefore only the gray area of the wedge is considered and not the part that is affected by the backwall. Dashed line represents the values from the SSW.

4.2) Wedge evolution in the analogue sand wedge and self-similar wedge (SSW)

The analogue sand wedge is compared to an analytical SSW that continuously follows the critical taper while doing minimum work. For more detailed information on the creation of the two wedges, measurement of slope and calculation of work, refer to Appendix 4.1.

The analogue wedge evolves in a typical cyclic manner of frontal accretion to underthrusting resulting in saw-tooth like growth curves in height, length and slope (Fig. 4.2A, B, C). With every accretionary cycle the length of the wedge increases first with the formation of a new fault and then decreases as the wedge shortens (Fig. 4.2A). The height of the wedge increases later in the accretionary cycle due to underthrusting of the fault and subsequent uplift of the wedge (Fig. 4.2B). Since length and height do not increase simultaneously, the slope of the wedge is shallow in the beginning and steepens at the end of each accretionary cycle (Fig. 4.2C). Initially the slope fluctuates around the static and kinetic critical taper envelope. This is in accordance with first order failure of the incoming sand layer and fault formation at the toe of the wedge related to the static $\mu_{internal}$ and displacement along the fault plane related to the kinetic $\mu_{internal}$. After a short initiation phase the wedge develops towards a stable wedge taper (~10°) with systematic fluctuations associated with each cycle (Fig. 4.2, 4.3).

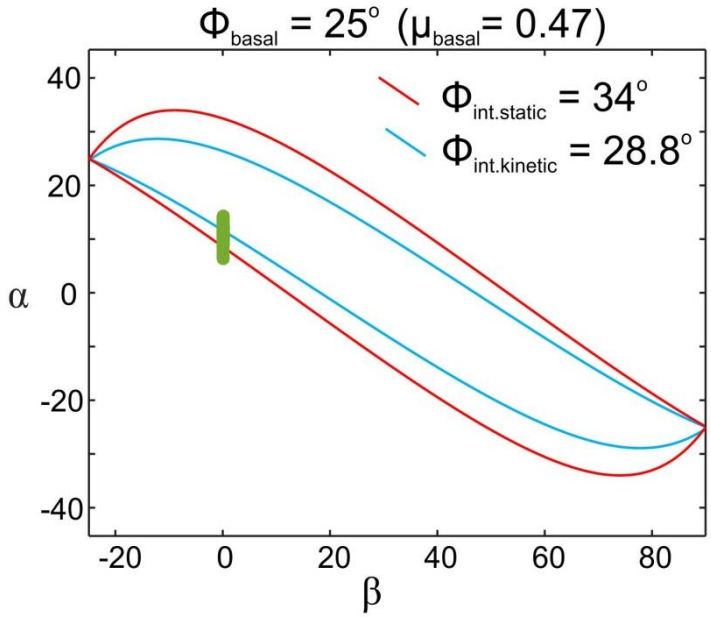

Figure 4.3- A) Critical taper envelope for the analogue wedge with $\mu_{internal}$ (0.68 / 0.55 – static / kinetic) with μ_{basal} = 0.47. The curves representing static (red) and kinetic (blue) friction are created after Dahlen, 1984 and Lehner, 1986. The green line is a cluster of dots that represents the slope of the wedge over time.

Work done by the wedge is divided into gravitational (work done against gravity) and frictional work (work done against friction on the horizontal plane). Gravitational work done by the analogue wedge and SSW is significantly lower than frictional work because vertical displacement is generally less than horizontal displacement of the wedge (Fig. 4.4). In addition, the greatest energy is consumed by the work done against friction (Del Castello and Cooke, 2007). Work done by the SSW increases at a constant rate due to increase in the volume sliding and therefore increasing frictional work. Gravitational work is done by the SSW is by uplift of the whole wedge due to basal accretion. Total work of the analogue wedge is minimized and closest to that of the SSW at the end of an accretion cycle. At the onset of a new accretion cycle, gravitational work is minimized but increases subsequently as

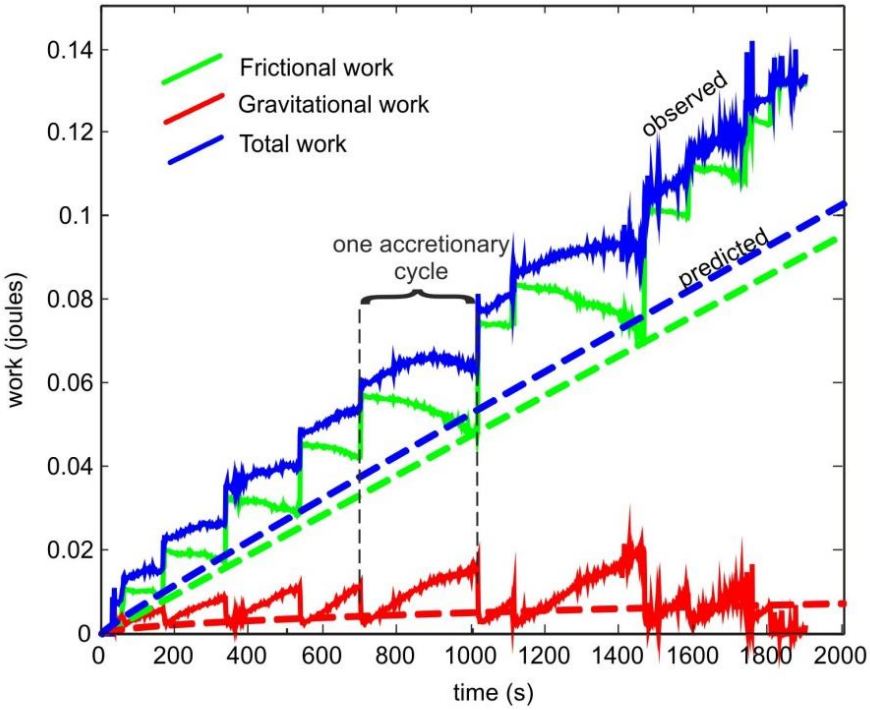

Figure 4.4- A comparison of work done by the analogue wedge (solid lines) and the SSW (dashed lines). Total work for both wedges is a combination of frictional and gravitational work. For further comparison of the two wedges, data from the analogue experiments and SSW is considered as the observed and predicted values respectively.

the active thrust ramp penetrates deeper into the wedge and therefore uplifts successively larger volumes. Frictional work, in contrast, is maximized at the onset of a new accretion cycle and subsequently decreases as the active thrust ramp underthrusts the wedge thus decreasing the décollement length.

4.3) Comparison of geometry and work between the two wedges

The difference in geometry and work between the analogue wedge and the SSW is compared by taking the difference between the two and dividing it by the predicted values from the SSW (Details of the calculation are presented in A4.1). Using this quantification and a comparison of percent difference in work vs. percent difference in slope, a time step of the analogue wedge with a low work percentage or low slope percentage would be considered a minimum work wedge or critical taper wedge respectively (Fig. 4.5). A combination of both low work percentage and low slope percentage can be considered a unification between meeting the critical taper and minimizing work or an ideal state. The slope of the analogue wedge is also compared with the static and kinetic critical taper, thus an ideal static and kinetic critical taper wedge is also considered. This comparison of work and slope in Fig. 4.5 indicates that the analogue wedge moves from the static critical taper towards the kinetic critical taper and also proceeds towards the minimum work model in each accretionary cycle (Fig. 4.5). On a longer time scale and with every accretionary cycle the analogue wedge deviates less and moves progressively towards the ideal state. The relative difference in wedge geometry and work is also calculated for wedges with different μ_{basal}

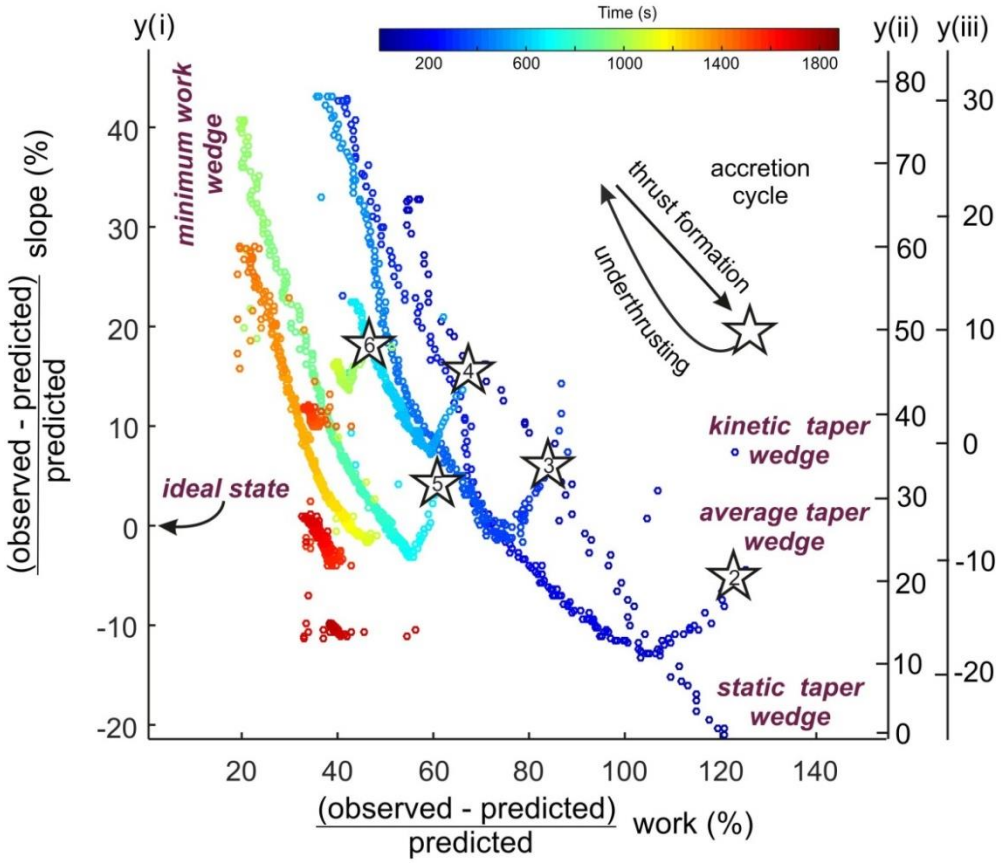

Figure 4.5- Comparison of the relative difference in slope vs. the relative difference in work, between the two wedges. Values closest to the y-axis and x-axis would be from a wedge following the minimum work concept and the critical taper theory respectively. The graph demonstrates that at the beginning of an accretionary cycle the analogue wedge is closest to being a critical taper wedge and at the end of the accretionary cycle it is closest to being a minimum work wedge. Over time and each accretionary cycle (numbered in the star) the wedge proceeds towards an ideal state.

(Appendix A4.2.1). The similarity in trends for relative difference in work indicates that the results and interpretations hold true regardless of the μ_{basal} except for variations in internal kinematics (Fig. A4.2.4A)

4.4) Implications for the analysis of accretionary wedges

The comparison of work and slope together demonstrates that sand wedges are sometimes smart and sometimes beautiful but never at the same time. At the beginning of a cycle, the lengthening of the wedge produces a shallower taper, making the wedge closest to the ideal critical taper wedge. As accretion proceeds, underthrusting appears to be the energetically preferred path of accreting material but leads to shortening and uplift of the wedge, and deviation away from an ideal critical taper wedge. The latter can only be re-established by forming a new, energetically unfavorable frontal thrust ahead of the wedge tip lowering the taper to the ideal geometry but away from the minimum work wedge. Although, the analogue wedge moves away from a MWC, external work on the underthrusting fault is lessened. When a new frontal thrust is favored, though it is energy wise expensive it is still cheaper than

underthrusting a progressively increasing wedge load (Del Castello and Cooke, 2007). In this way, accretionary cycles cannot reach the ideal state easily but rather circles between energetically vs. geometrically optimized states at progressively decreasing distance from the ideal state (Fig. 4.5). Therefore, only very mature wedges composed of several tens of accretion cycles may be able to reach a state where both geometry and work are optimized through the accretionary cycle. A calculation of relative work for several wedges with different μ_{basal} frictions indicates that after 50 cm of convergence (approximately 3-5 accretionary cycles) the relative difference in minimum work stabilizes at 50%.

The CTT accurately predicts the topography and a taper angle where the wedge is stable assuming that the wedge is continuously homogenous in terms of its physical properties (Fig. 4.3). However, the wedge is not always at criticality because the formation of faults to accommodate new material and allow the wedge to transition towards the preferred taper geometry is not considered. Localization of strain, varying $\mu_{internal}$ due to the transition from the static critical taper to the kinetic critical taper and varying fault properties due to the interaction of the basal décollement with the overlying wedge indicates that the wedge is heterogeneous. This interaction also presents a change in the stress regime and has significant influence on the timing of accretionary cycles and when the wedge is close to criticality. Although the critical taper is not always met in natural and analogue wedges, criticality is a systems attractor (Bak et al., 1988) because it is geometrically the taper limit of the wedge. From this analysis it is evident that the wedge is closest to the critical taper geometry not only after numerous cycles (Wang and Hu, 2006) but also on a smaller temporal scale and at the beginning of each accretionary cycle (Fig. 4.5).

The MWC functions on alleviating the external stress on the wedge system which includes the mature wedge (consisting of older faults) and the active fault. As an accretionary cycle progresses, underthrusting or formation of a new fault is favored based on energy efficiency. Therefore, when the friction along a fault plane is lowered, there is a change in stress regime that is taken into account and it is energetically easier to continue underthrusting a larger load of the wedge. In this respect MWC explains the deformation path in each finite time step, based on the varying stress regime that may be due to changing properties of the fault and wedge (Chapple, 1978; Gutscher et al., 1998; Cooke and Madden, 2014). In this study, only the work done by the wedge is considered (part of the wedge above the incoming layer - Fig. 4.2 c) and not the work done by the incoming layer or the new fault. Work done by the new active fault increases over the timespan of an accretionary cycle until the next fault is formed (Del Castello and Cooke, 2007). Therefore, together all the work done by the fault and wedge over the course of an accretionary cycle is balanced.

4.5) Towards understanding natural wedges

As seen in this study, the critical taper slope depends on the maturity of the wedge and stage of the accretionary cycle. Therefore, to ensure that a similar state of criticality is assumed for a natural study area, the study area to which the critical taper theory is applied should have the same geological setting, erosion activity (similar climatic conditions) and mechanical boundary conditions. Values for the coefficient of friction (ex. static and kinetic) also change

the state of criticality therefore it is important to have the same geology and kinematic deformation style. In addition from this analysis it is evident that inferences on wedge properties of natural observations based on CTT should be drawn when the wedge is closest to criticality. To apply the CTT, if one of these criteria are not the same then there is an added degree of freedom and this variation in the areas should be taken into consideration.

The critical taper theory has been applied to natural settings to determine the frictional properties of the basal décollement or the pore fluid pressure (Fagereng, 2011; Cubas et al., 2013; von Hagke et al., 2014,). To obtain precise results from this application the area of the wedge has to be at criticality. The next question that presents itself is how does one determine that the natural wedge is at criticality. A wedge is at the state of criticality when any perturbation causes failure or deformation of the wedge. Therefore, it is also important when applying the critical taper theory to state the criteria for determining that the wedge is at criticality. Von Hagke et al. (2014) assumed the area in the Alps was at criticality based on the fact that any perturbations like the drilling of tunnels, wells or rainfall caused deformation in the form of seismicity. Implication of calculating physical properties of the wedge when the wedge is not at criticality would cause overestimation or underestimation of the values. In this case one can also estimate the upper bound and the lower bound of taper angle, by measuring the taper of the entire area provided the above mentioned criteria holds (i.e. erosion activity, deformation style, same geological age).

Deformation paths in natural systems are based on the evolution and complexity of the physical property changes due to intrinsic or extrinsic conditions. Although the Central European Alps is close to critical state, application of the CTT shows a variation in the strength of the basal décollement that correlates well with the lithology of the décollement (von Hagke et al., 2014). Similarly, along strike variations along the Hikurangi subduction thrust in New Zealand are due to variations in relative strengths of the wedge material (Fagereng, 2011). In addition extrinsic conditions like the rate of erosion and sedimentation causes a variation in minimum work done by the wedge and affects the activity and distribution of faulting (Hardy et al., 1998; Yagupsky et al., 2014). Fundamentally, the MWC sheds light on the deformation events that took place to reach the present day configurations of the wedge.

4.6) Conclusion

It appears that natural accretionary wedges are described in rare instances as critical taper or minimum work wedges. Instead, most wedge stages reflect the competition between a geometrically coherent (reaching different stages of criticality based on the static and kinetic $\mu_{internal}$) and an energetically preferred state. Specifically, the CTT defines the geometry of the wedge and the MWC determines the deformation path taking into account the varying stress regimes over time. In this regard, natural wedges are neither model/theoretical critical taper wedge nor are they completely minimum work wedges but a combination of the two wedge models. Therefore, the combination of both theories has key implications for understanding the different parts of wedge behaviour and deformation path of natural orogens globally. Particularly, CTT applied to natural orogens close to criticality ensures better estimations of

the physical properties. The MWC helps determine the deformation style chosen to reach a sustainable geometry by alleviating external work (climatic effects, sedimentation, varying boundary conditions etc.) acting on the orogen.

References

Adam, J., Urai, J.L., Wieneke, B., Oncken, O., Pfeifer, K., Kukowski, N., Lohrmann, J., Hoth, S., van der Zee, W., Schmatz, J., 2005, Shear localization and strain distribution during tectonic faulting-new insights from granular-flow experiments and high-resolution optical image correlation techniques: Journal of Structural Geology, v. 27, p. 283-301

Chapple, W.M., 1978, Mechanics of thin-skinned fold-and-thrust belts: Geological Society of America Bulletin, v. 89, p. 1189-1198

Cooke, M.L., Madden, E. H., 2014, Is the Earth lazy? A review of work minimization in fault evolution: Journal of Structural Geology, v. 66, p. 334-346.

Cooke, M.L., Murphy, S., 2004, Assessing the work budget and efficiency of fault systems using mechanical models: Journal of Geophysical Research. Solid Earth, v.109, doi: 10.1029/2004JB002968

Cubas, N., Avouac, J-P., Souloumiac, P., Leroy, Y., 2013, Megathrust friction determined from mechanical analysis of the forearc in the Maule earthquake area: Earth and Planetary Science Letters, v. 381, p. 92-103

Cubas, N., Leroy, Y.M., Maillot, B., 2008, Prediction of thrusting sequences in accretionary wedges: Journal of Geophysical research, v. 113, doi:10.1029/2008JB005717

Dahlen, F.A., 1984, Noncohesive critical coulomb wedges: an exact solution: Journal of Geophysical Research, v. 89, no. B12, p. 10125-10133.

Davis, D., Suppe, J., Dahlen, F.A., 1983, Mechanics of Fold –and –Thrust Belts and Accretionary Wedges: Journal of Geophysical Research, v.88, p. 1153-1172.

Del Castello, M., Cooke, M.L., 2007, Underthrusting-accretion cycle: Work budget as revealed by the boundary element method. Journal of Geophysical Research, v. 112, doi: 10.1029/2007JB004997

Fagereng, Å., 2011, Wedge geometry, mechanical strength, and interseismic coupling on the Kikurangi subduction thrust, New Zealand: Tectonophysics, v. 507, p. 26-30

Gutscher, M-A., Kukowski, N., Malavieille, J., Lallemand, S., 1998, Episodic imbricate thrusting and underthrusting: Analog experiments and mechanical analysis applied to the Alaskan Accretionary Wedge: Journal of Geophysical Research, v. 103, no. B5, p. 10161 – 10176

Hampel, A., Adam, J., Kukowski, N., 2004, Response of the tectonically erosive south Peruvian forearc to subduction of the Nazca Ridge: analysis of three-dimensional analogue experiments: Tectonics, 23, doi:10.1029/2003TC001585

Hardy, S., Duncan, C., Masek, J., Brown, D., 1998, Minimum work, fault activity and the growth of critical wedges in fold and thrust belts: Basin Research, v. 10, p. 365-373.

Hoth, S., Hoffmann-Rothe, A., Kukowski, N., 2007, Frontal accretion: An internal clock for bivergent wedge deformation and surface uplift: Journal of Geophysical Research, v. 112, doi: 10.1029/2006JB004357.

Lehner, F.K., 1986, Comments on Noncohesive Critical Coulomb Wedges: An Exact Solution" by F.A. Dahlen: Journal of Geophysical Research, v. 91, no. B1, p. 793-796

Lohrmann, J., Kukowski, N., Adam, J., Oncken, O., 2003. The impact of analogue material properties on the geometry, kinematics, and dynamics of convergent sand wedges: Journal of Structural Geology, v. 25, p.1691-1711.

Masek, J.G., Duncan, C.C., 1998, Minimum-work mountain building: Journal of Geophysical Research, v. 103, no. B1, p. 907-917.

Mitra, G., Boyer, S.E., 1986. Energy balance and deformation mechanisms of duplexes: Journal of Structural Geology, v. 8, p. 291-304.

Simpson, G., 2011, Mechanics of non-critical fold-thrust belts based on finite element models: Tectonophysics, 499, p. 142-155

von Hagke, C., Oncken, O., Evseev, S., 2014, Critical taper analysis reveals lithological control of variations in detachment strength: An analysis of the Alpine basal detachment (Swiss Alps): Geochemistry Geophysics Geosystems, v. 15, p. 176-191

Wang, K., Hu, Y., 2006, Accretionary prisms in subduction earthquake cycles: The theory of dynamic Coulomb wedge: Journal of Geophysical Research, v. 111, doi:10.1029/2005JB003987

Yagupsky, D. L., Brooks, B., Whipple, K. X., Duncan, C. C., Michael, B., 2014, Distribution of active faulting along orogenic wedges: Minimum-work models and natural analogue: Journal of Structural Geology, v. 66, p.237-247

Appendix A4.1
Experimental design and analysis

The details of the analogue sand wedge experiments and analytical self-similar wedge are presented here. In addition, the calculation of work in each of the wedges and the comparison of geometry and work done by the analogue and self-similar wedge is also shown here.

Analogue wedge

The analogue accretionary wedge (Fig.4.1B) is created in a glass box with dimensions 300 cm long, 20 cm wide and has a base that consists of a rubber conveyor belt. On the conveyor belt, a sand layer (coefficient of friction, $\mu_{internal}$=0.68 / 0.55, static / kinetic) of 2.5cm is sieved over a layer of 0.5 cm of glass beads (basal coefficient of friction, μ_{basal}=0.47/ 0.40, static / kinetic) that acts as a low friction basal décollement. A typical plane strain compressional sand wedge is created by pulling the sand and glass bead layer against a rigid back wall. The evolution of the wedge is recorded from the side using CCD (charge coupled device, 11 MPx, 16 bit) cameras. Sequential images recorded at 1 Hz are calibrated, cross-correlated and analyzed by means of the Particle Image Velocimetry (PIV) software (Hampel al., 2004; Adam et al., 2005; Hoth et al, 2007). The processed data consists of a time-series collection of the incremental geometries and internal displacement fields (velocity) of the entire wedge. For analysis of the wedge geometry, the topographic static (crest) and the tip of the wedge were assigned active wedge height (H) and length (L) and are used for calculating the wedge slope (arc tan (H/L)). Therefore only the part that is truly wedge shaped is considered without the part that is dipping towards the backwall (Fig. 4.2C).

Deformation of the wedge allows for both frontal accretion and sporadic deep underthrusting due to smearing of the thrust ramp with low friction glass beads (Chapter 2). In this respect, the analogue model has an added complexity with the presence of a layer of glass beads as a basal décollement. The interaction of the low friction base with the internal friction of the wedge produces an irregular pattern of fault lengths and lifetime which makes the analogue wedge model a better representative of natural wedges.

Self-similar wedge

The ideal self-similar wedge (Fig. 4.1C) is created to follow the critical taper theory (Fig. 4.1A) continuously over time. In other words, the geometry of the wedge is always at the critical taper and therefore it is always at criticality. To create such a wedge a constant volume, similar to the analogue wedge, is added homogenously to the wedge. Therefore the wedge grows with a constant increase in volume at every time step while maintaining the critical taper. For calculating the gravitational work it is assumed that the material is added incrementally to the base over the whole length of the wedge. Since the wedge grows with a constant volume increase and constant slope the height and length ratio is also constant. However the height and length individually increase with a power law trend. The power law trend over time is due to the fact that the constant addition in volume is spread over a larger area with every time step leading to smaller increases in height and length. The analytical wedge is created using the same $\mu_{internal}$ (0.68 – static) and μ_{basal} (0.47 – static) as the analogue

wedge. To keep the wedge homogenous like the critical taper wedge only one value is considered for coefficient of friction and do not include the kinetic coefficient of friction. Strain localization and the formation of faults or accretionary cycles are also not taken into consideration therefore allowing it to increase in height and length simultaneously (Fig. 4.2A, B). The slope that is prescribed for the analytical self-similar wedge is the statistically calculated mean slope from all analogue experiments with the same setup. Since the mean slope appears to lie between the static critical taper and the kinetic critical taper (due to static and kinetic $\mu_{internal}$ respectively) (Fig. 4.2C), it is chosen as the slope for the self-similar wedge. Therefore, this is termed the average critical taper. However, the theoretical static and kinetic taper are also used for comparison with the analogue wedge. More information on the comparison of the self-similar wedge with wedges of different basal frictions is mentioned in the Appendix 4.2. The values for the static and kinetic $\mu_{internal}$ are obtained from the Ring-shear test that is used to calculate the coefficient of friction for the sand.

Calculation of work

In this study, work done by the wedge is calculated as a whole therefore not to be mistaken with work calculated for a fault in previous studies (Mitra and Boyer, 1986; Del Castello and Cooke, 2007; Cooke and Madden, 2014). However, the principles of calculating work in both cases are the same. Work is divided into two components, gravitational work and frictional work. The vertical component (Dy) of the observed incremental displacement field (i.e. uplift against gravity g) and the horizontal component (Dx, basal displacement against basal friction μ_{basal}) are used to calculate the gravitational (Wg) and frictional (Wf) work done by the wedge, respectively, with weight W (W = mass * gravity), as follows-

$$W_g = W * D_y \quad (1)$$

$$W_f = W * D_x * \mu_{basal} \quad (2)$$

Specifically Dy and Dx are the average uplift and displacement relative to a fixed base, respectively calculated from all the displacement vectors in the wedge. For each time step (t) a single value of Dy and Dx is calculated as follows

$$Dx_t = Avg\ (Dx) * n_{vectors} \quad (3)$$

$$Dy_t = Avg\ (Dy) * n_{vectors} \quad (4)$$

where Avg (Dx) and Avg (Dy) is the average uplift and displacement relative to a fixed base, for all vectors that make the wedge and $n_{vectors}$ is the number of vectors. Vectors that show negative displacement (displacement in the down direction or opposite of the convergence direction) due to subsidence of material are not included in the calculation of Dx and Dy.

The total work is the sum of the gravitational and frictional work. Other types of work like "seismic" work or heat due to slip along a fault and work due to generation of a new fault are part of the frictional work done by the wedge in this approach. Since work for the wedge is calculated as a whole, work done due to dilation of grains and internal work is part of the total work.

Comparison of geometry and work between the two wedges

To better realize the role of the CTT and MWC in the deformation of wedges, the analogue wedge is compared to the self-similar wedge. The self-similar wedge is considered the theoretical wedge that best follows both the MWC and the CTT. Observed values of total work and slope of the analogue wedge are compared to the predicted values obtained from the theoretical self-similar wedge. This is done by calculating the normalized difference between the two wedges, for both slope and total work, as follows

$$\% = \frac{observed - predicted}{predicted} * 100 \quad (3)$$

The percentage is calculated to quantify at each time step, how far the analogue wedge progresses away or towards the minimum work or critical taper wedge. To visualize this relationship, percent difference in work is plotted against percent difference in slope (Fig. 4.4).

Using this quantification and a comparison of percent difference in work vs. percent difference in slope, the stage of the analogue wedge with a low work percentage or low slope percentage would be considered a minimum work wedge or critical taper wedge respectively (Fig. 4.4). A combination of both low work percentage and low slope percentage can be considered a balance between meeting the critical taper and minimizing work or an ideal state.

Appendix A4.2
Analogue accretionary wedges with different basal frictions

Results from analogue accretionary wedges with different basal frictions is presented here. The experimental setups of the wedges are as follows and are the same as those presented in Chapter 2.
Setup 0) 3cm layer of sand
Setup 3) 2.5cm layer of sand on 0.5 cm 300-400 μm glass beads
Setup 2) 2.5cm layer of sand on 0.5 cm 200-300 μm glass beads
Setup 1a) 2.5cm layer of sand on 0.5 cm 100-200 μm glass beads (Setup a)
Setup 1b) 2.8cm layer of sand on 0.2 cm 100-200 μm glass beads (Setup b)

The coefficient of friction for the materials used in the above setups are presented in Table A4.2.1. These values have been calculated from tests on the material in the Ring-shear tester. For wedges in each setup, the mode of deformation also differs due to the evolution of the internal kinematics caused by the initial setup. Setup 0 has the strongest base and deforms mainly by frontal accretion. Wedges in setup 3, 2 and 1a deform mainly by underthrusting and occasionally by the reactivation of faults and wedges in setup 1b have the weakest base and deforms by frontal accretion and fault reactivation. For all wedges regardless of setup, the horizontal growth is more than the vertical growth (Fig. A4.2.1A). Compared to the self-similar wedge that has a power law trend in length and height of the wedge the height and length of the analogue wedge has a cyclic pattern with every accretionary cycle. Due to the cyclic growth of length and height the slope of the wedge is also cyclic (Fig. A4.2.1B).

setup	μ_{basal} (static/ kinetic)	Mean slope (n)	σ	Mode of deformation	Slope of SSW	Theoretical critical taper ($static_{internal}$ / $kinetic_{internal}$)
0	0.68 / 0.55	17 (7)	2.12	Underthrusting	17	18 / NA
3	0.53 / 0.43	12 (5)	3.23	Underthrusting and some fault reactivation	12	10 / 15
2	0.50 / 0.42	15 (5)	3.04	Underthrusting and some fault reactivation	11	9 / 13
1a	0.47 / 0.40	12 (5)	4.14	Underthrusting and some fault reactivation	10	8 / 11
1b	0.47 / 0.40	9.69 (5)	2.54	Mainly fault reactivation	10	8 / 11

Table A4.2.1- Static and kinetic friction of the basal décollement of the wedges in each setup, mean slope (n = number of experiments) and standard deviation (from Chapter 2) used to build the analytical self-similar wedge for comparison. The difference in mode of deformation of wedges in each setup and the theoretical critical taper is also mentioned.

The slope of the analogue wedge is compared to the slope prescribed for the self-similar wedge. The slope prescribed for the SSW is also shown in this Table A4.2.1. This slope is chosen based on the mean slope of all the wedges in that setup. However the mean slope for experiments with setup 2 is unusually high in comparison to the other setups. In this case a slope value was chosen closest to the slope of the wedge at the beginning of the accretionary cycles since this appears to be the trend for other wedges once the wedge is established (Fig. A4.2.1B). Similarly, for setup 1a and 1b (both with the same $\mu_{internal}$ and μ_{basal} values) a slope of 10 was chosen. In addition, the theoretical critical taper based on the static and kinetic $\mu_{internal}$ is also mentioned in the Table A4.2.1 and displayed in Fig. A4.2.1B and A4.2.2. For most experiments the average taper lies between the static critical taper and the kinetic critical taper. It is observed in most setups that in the first few accretionary cycles, the slope of the wedge moves away from the static critical taper envelope towards the kinetic critical taper envelope. As the wedge matures, it gets weaker and the slope at the beginning of an accretionary cycle is closest to the average taper. For setup 0 the theoretical static taper is higher than average taper by one degree. Here, the wedge has a strong base and may need few more accretionary cycles to reach the static taper. For setup 1b, the slope of the wedge shallows over time. The wedge has a weak base and deforms by frontal accretion and reactivation of older faults to produces a shallow wedge. Over time the hinterland part of the wedge has a very shallow dip and is almost plateau-like, almost inactive and not part of a critical taper wedge. However since the slope of the entire wedge (regardless of active or inactive parts) is measured similar to the measuring strategy of the other wedges in the other setups, the weak base wedge begins to shallow as it matures. Thus the difference between the analogue wedge slope and the average taper angles increases.

Gravitational work is minimum at the beginning of an accretionary cycle and maximized at the end in comparison to frictional work that is maximized at the beginning of an accretionary cycle and decreases over the timespan of the cycle (Fig. A4.2.1C). In all wedges, and in each accretionary cycle the analogue wedge moves away from the static critical taper wedge towards the kinetic critical taper wedge. In comparison to the minimum work the analogue wedge progressively moves toward being a minimum work wedge over the time span of an accretionary cycle. (Fig. A4.2.3A, B, C). Over the entire evolution of the wedge, the wedge moves closer to the ideal state that meets both the CTT and the MWC. The only exception is the wedge with the lowest μ_{basal} (Fig. A4.2.3D, A4.2.4A). Here, over time the shallowing of the wedge slope, creates an increase in difference compared to the average taper. For setup 0 the difference in slope increases as the wedge becomes steeper than the average critical taper. Here, the wedge perhaps has not yet reached stability in the accretionary cycles and therefore the average critical taper is lower than the true average if the wedge were at a state of stability. The relative difference in work for all wedges decreases and appears to stabilize to approximately less than 50% after 500 seconds (50 cm of convergence) (Fig. A4.2.4B). The similarity in trends indicates that these results and interpretations hold true regardless of the $\mu_{internal}$ and $\mu_{basal.}$

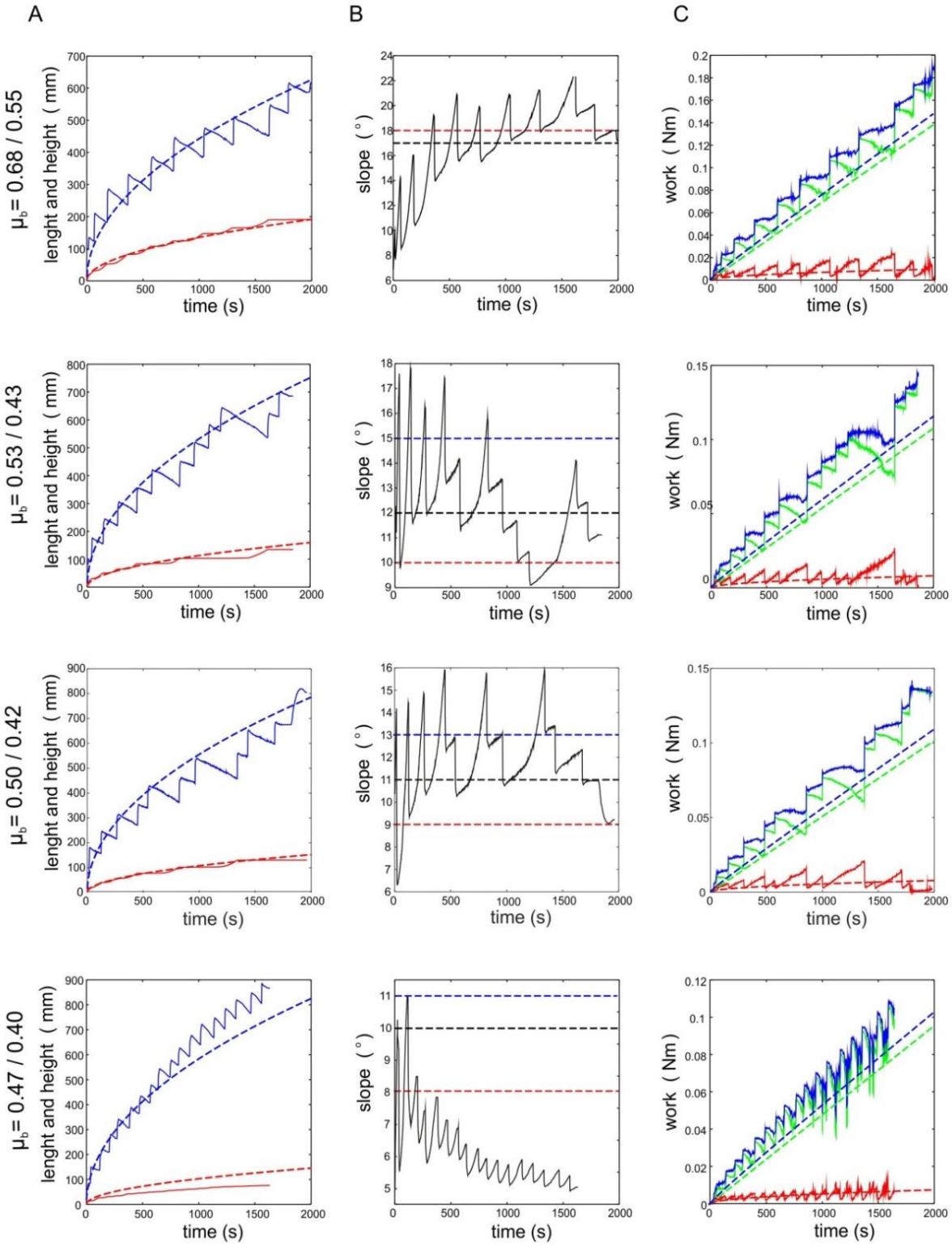

Figure A4.2.1- A) length (blue) and height (red) with the respective values from the self-similar wedge (dashed lines) B) slope of the analogue (solid). Slope of the three different self-similar wedge with slope based on the average slope of all experiments with like setups (black dashed) static $\mu_{internal}$ (red) and kinetic $\mu_{internal}$ (blue). C) work (frictional (blue), gravitational (red) and total work (green)) done by analogue wedge (solid lines) and self-similar wedge (dashed), with different μ_{basal} (static / kinetic)

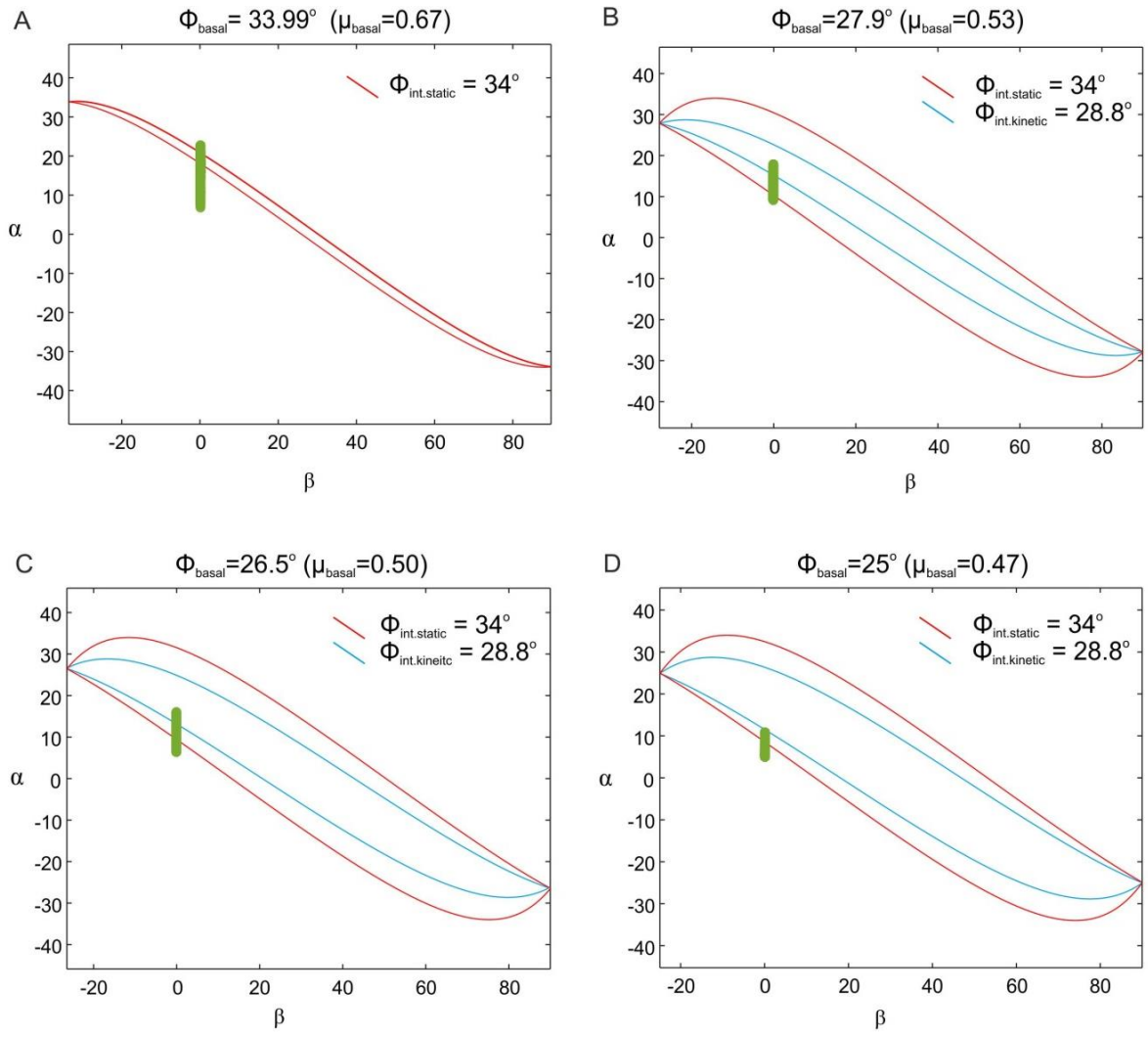

Figure A4.2.2- Critical taper envelopes for the static internal coefficient of friction (red curve) and kinetic internal coefficient of friction (blue curve) and for basal coefficient of friction of A) 33.99^o (setup 0) B) 27.9^o (setup 3) C) 26.5^o (setup 2) D) 25^o (setup 1b). The green line is a cluster of points representing the slope of the wedge over time. The critical taper envelopes have been calculated using equations and solutions from Dahlen, 1984 and Lehner, 1986.

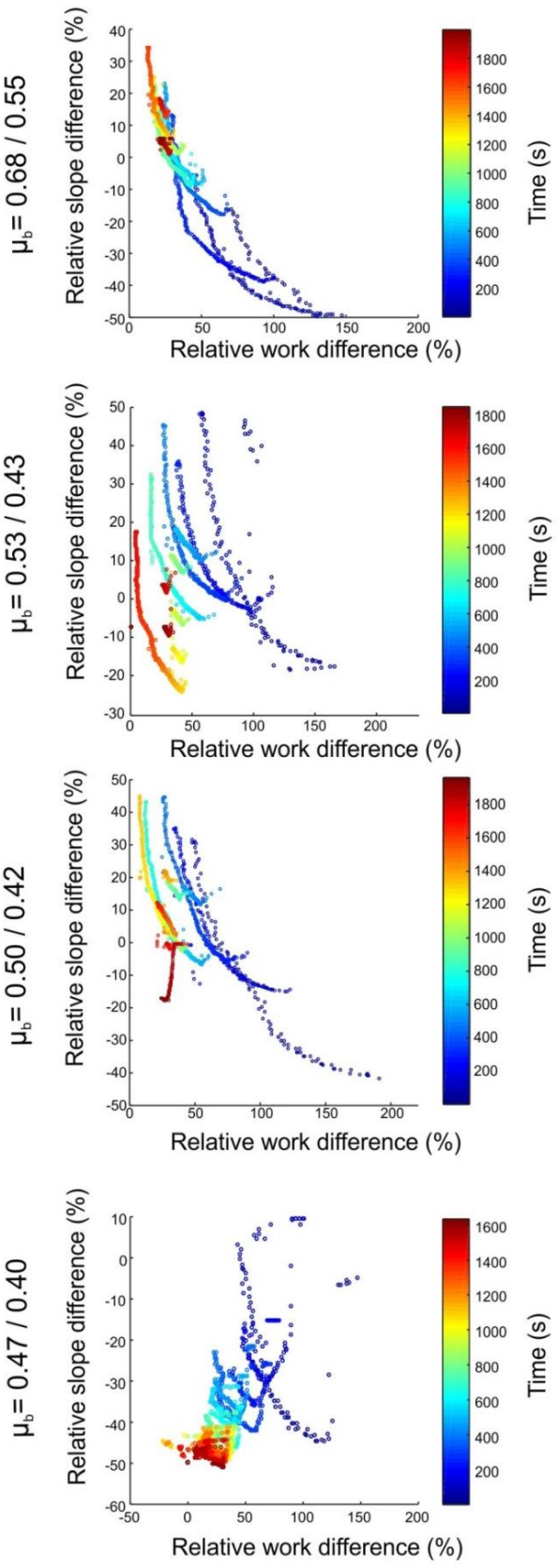

Figure A4.2.3- Relative difference of slope vs. relative difference of work for wedges from A) setup 0, B) setup 3, C) setup 2 and D) setup 1b.

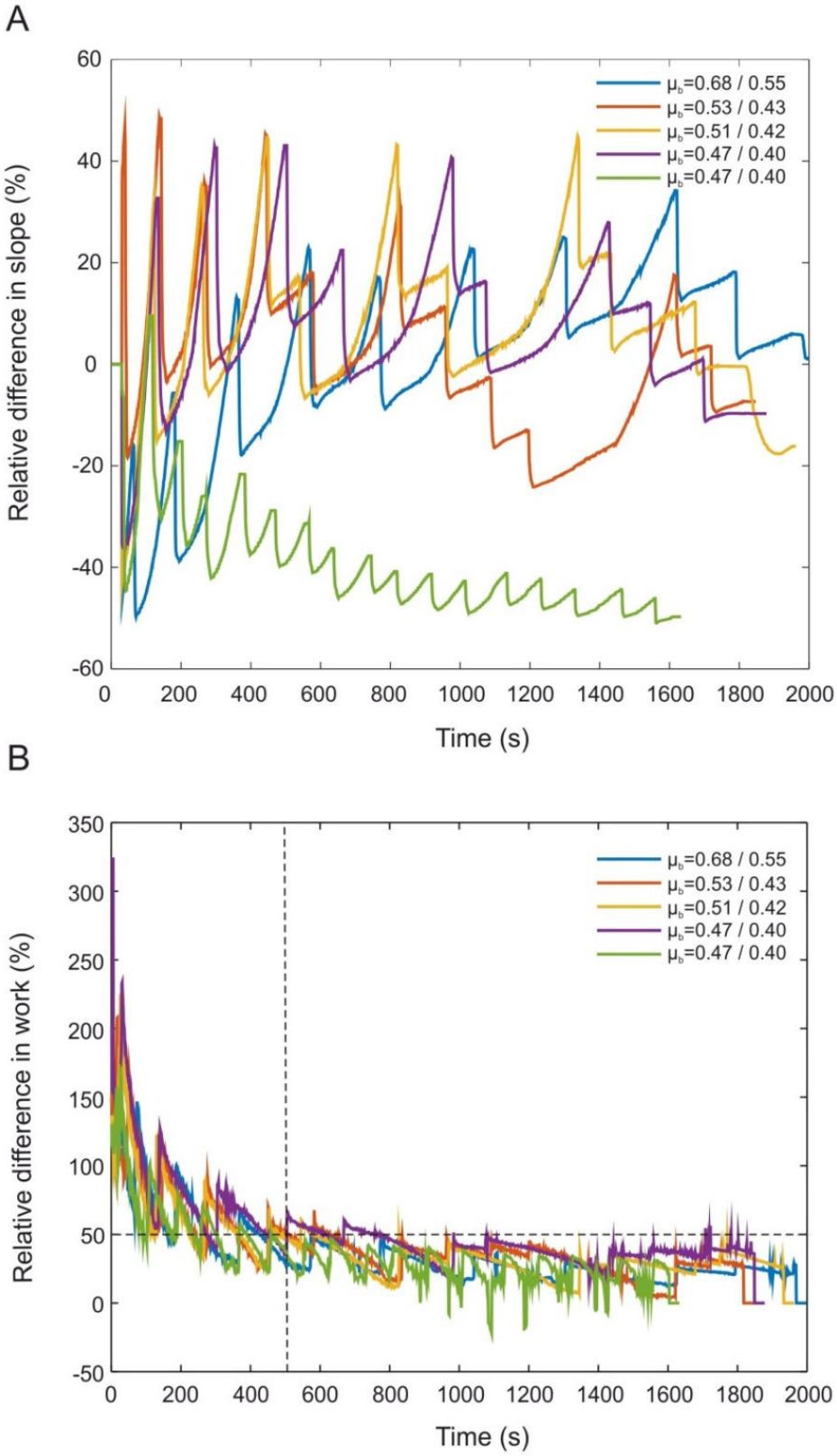

Figure A4.2.4- A) Relative difference in slope vs. time and B) Relative difference in work vs. time for the different basal frictions. The μ_{basal} values show static and kinetic values. Note the difference in trend for the wedge with the lowest basal friction. Vertical dashed line in (B) indicates the time needed for the work to stabilize to approximately 50% (horizontal dashed line) difference from the analytical (self-similar wedge) values.

Chapter 5- Further developments

5.1) Rheology of a new analogue material to study ductile deformation*

*This rheological study is part of a benchmark study between four international laboratories. Presented here is the part of the study completed by myself at the GFZ analogue modeling laboratory. The entire study is published as follows-
Di Giuseppe, E., Corbi, F., Funiciello, F., Massmeyer, A., Santimano, T.N., Rosenau, M., Davaille, A., 2014. Characterization of Carbopol hydrogel rheology for experimental tectonics and geodynamics. Tectonophysics. doi:10.1016/j.tecto.2014.12.005

5.1.1) Introduction

There is a need for an analogue material that is non-Newtonian to understand how ductile behavior affects deformation in the crust. An analogue material that can be used to study the plastic as well as elastic and viscous properties of the lithosphere. Therefore, the material has to have a stress strain relationship that is not linear where the viscosity depends on the degree of applied shear load and that has a yield strength such that if the yield strength is overcome the material begins to flow. Below this limit the material behaves elastically and once the threshold is overcome the material is strain rate softening. Carbopol is such a material that exhibits shear thinning behavior. It is usually used as rheology modifiers to thicken, suspend of beads or grains and stabilize gels especially in the cosmetic and medical industry. It has been previously and successfully used as an analogue for brittle crustal processes by Schrank et al., 2008; Reber et al., 2015 and also for mantle dynamics by Massmeyer et al., 2013.

Here, the part of the benchmark study that was performed by me at the Analogue modelling laboratory in the GFZ and partially at the LET laboratory in Roma Tre is presented. Commercially there are different types of Carbopol with specific properties based on their uses. In total six different Carbopol types were tested. At the GFZ and Roma Tre lab ETD 2050, EZ 2 and EZ 3 at concentrations 0.1wt%, 0.5wt% and 1.0wt% were tested.

5.1.2) Material properties of Carbopol

Carbopol is a cross-linked acrylic acid from the polymer family. Commercially it is found as a white powder. Each particle of Carbopol is a network of polymer chains that are cross linked. The powder is hydrophobic but when mixed with water at rigorous stirring rates, it absorbs the water and begins swells. At this point it is acidic and has a pH of around 2. To form a gel the Carbopol and water solution needs to be neutralized using a base. Samples in this study are neutralized using sodium Hydroxide (NaOH (18%)). Once the sample is neutralized it becomes a clear gel with very good transparency which is important for the observation during an experiment. The neutralized Carbopol samples are at the highest viscosity between the pH values 5 and 10 (Lubrizol, 2009). In the benchmark study, to ensure the reproducibility of the sample and to produce consistently similar sample every time, a detailed preparation protocol is prepared, tested and followed. The density of the material is realized using a pycnometer with a capillary tube. Measurements were made at room temperature (25^{o}c).

Since the material is made of water, the density of the material with the lowest concentration is close to that of water and increases with higher concentration. The preparation protocol and the density values can be found in Di Giuseppe et al., 2014

5.1.3) Rheology of Carbopol

To understand the rheology, rotational tests and oscillatory tests are performed. The rheometer used for this study is the Anton Paar Physica MCR301 rheometer. The geometrical plate used to test each sample is a stainless steel, sand blasted plate (PP50/SS) with a diameter of 50mm and a surface roughness of 30μm. The gap between the tool and the measuring plate is fixed at 0.5mm. The sample to be tested sits between this gap. Temperature during the test is kept constant with room temperature using the Peltier element of the Rheometer.

Results from the rotational test show the viscosity (η) as a function of the shear rate from 10^{-3} to 10^{-3} s^{-1}. For all three types of Carbopol regardless of concentration there is a decreasing trend in viscosity with increasing shear rate which is indicative of shear thinning behavior. Additionally, viscosity and the shear thinning behavior decreases with decreasing concentration. The oscillatory tests consist of the Amplitude sweep test (AST) and the Frequency sweep test (FST). In the AST the oscillatory test is performed at different amplitudes and constant frequency. Results from the AST show the storage modulus (G') and loss modulus (G"). The Linear viscoelastic (LVE) range at which G' and G" are constant and the yield stress at which G' and G" change is also displayed. The yield point or yield stress is the strain (γ (%)) at which the material changes properties. The γ (%) of the LVE range from the AST is then used to set the conditions for the FST. In the FST the oscillatory test is performed at different frequency keeping the amplitude constant.

Results of the AST and FST show that G' is greater than G" at low strain for all samples. This is indicative that the sample is gel-like at the beginning of the test. ETD2050 has an yield point at γ = 1.53% , 3.56 % and 9.58% for concentrations 0.1wt%, 0.5wt% and 1.0wt%. EZ2 has a an yield point at 4.36% for 0.5wt% and 7.77% for 1.0wt% while for EZ3 has an yield point at 7.85% for 0.5wt% and 10.4% for 1.0wt%. In all cases the γ value at the yield point increases as the concentration increases. All the Carbopol samples that were tested show an elastic behavior before the yield strength is met at which it behaves plastically and then flows with viscous behavior. The concentration of 0.5 – 1 wt% show yield stress in the order of hundreds of Pa and would be favorable to be used as an analogue for the ductile behavior of crustal rocks.

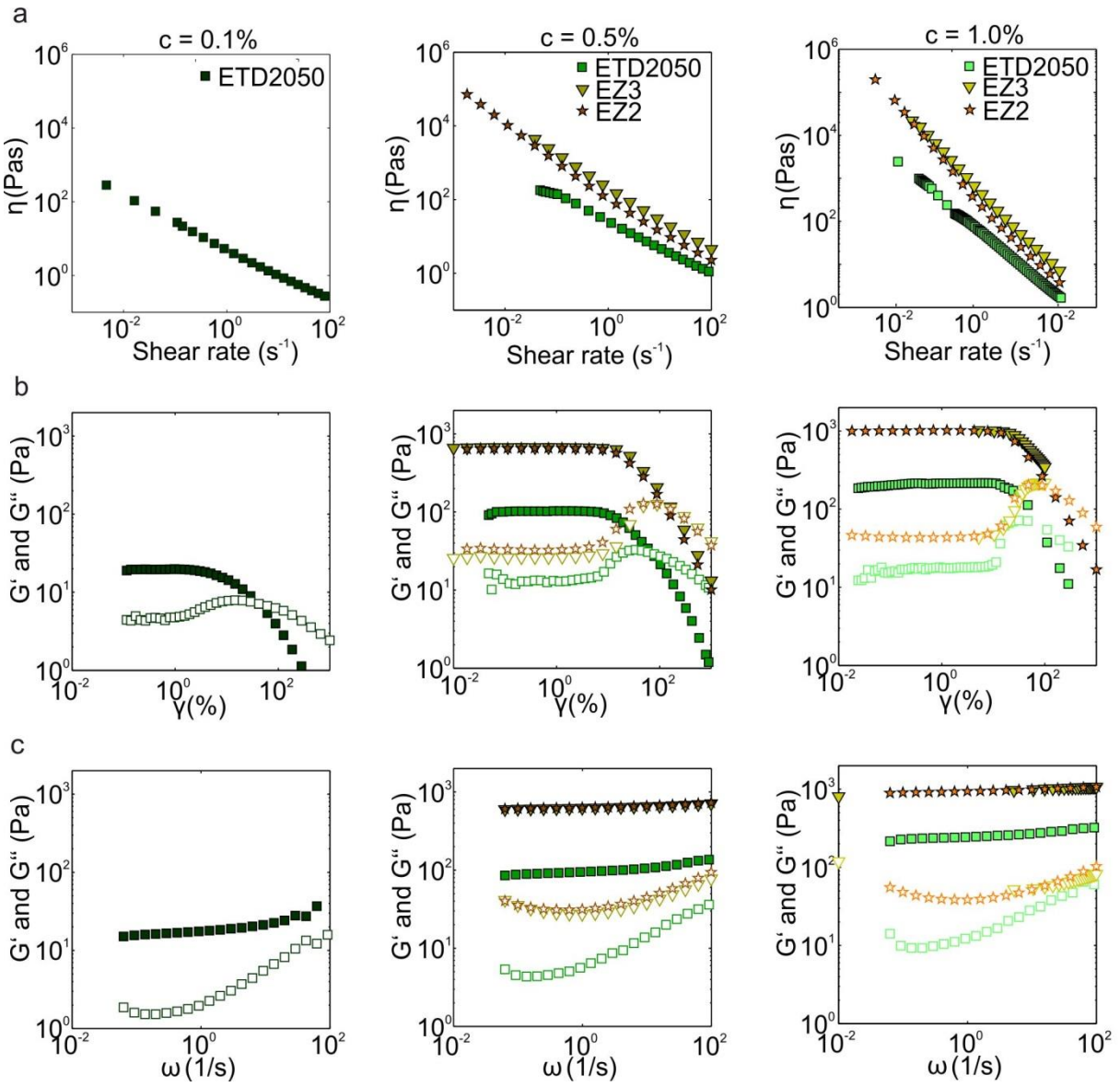

Figure 5.1- Test results for the three Carbopol types – ETD 2050, EZ 2 and EZ3 at concentrations 0.1 %, 0.5% and 1.0% are presented here. a) Rotational tests show the viscosity of the sample as a function of shear rate b) Oscillatory test- Amplitude sweep test shows the storage modulus (G") and loss modulus (G') as a function of shear strain and c) Frequency sweep test show the G' and G" as a function of angular frequency. In b and c filled symbols represent the storage modulus (G') and open symbols represent the loss modulus (G").

5.2) Force sensors in analogue experiments

5.2.1) Introduction

Understanding of geodynamic processes that are studied through analogue experiments is mainly based on the visual observation of an evolving model. Immense information is obtained from the incremental time-step analysis based on visualization of the surface processes in an analogue model. Analogue experimental setups have begun to include force sensors to record the change in forces and understand the stress regime in the model. As a first order observation, geological processes are an interaction of forces between different components of the natural system. In particular it is the balancing of forces, the accumulation of stress that drives deformation and produces the topography and formation of structures we see in analogue models. In this respect it is important to understand the stress regime in the model in order to gain insight of the geodynamic processes. Therefore, the monitoring of forces is an important addition to the analogue experimental design.

Force sensors have been used in studies to understand granular behavior in faults (Daniels and Hayman, 2008) the effect of erosion on tectonics (Cruz et al., 2010), to understand the stress regime during the processes of subduction (Boutelier and Oncken, 2011) and to quantify the effect of side wall friction in sand box experiments (Souloumiac et al., 2002). Here, an experimental setup is presented with a force sensor combined with the widely tested PIV technique. The PIV's recording technique is visually able to record spatial resolutions on the order of 0.1 mm over a temporal resolution of 10 Hz. The force sensor that is use has a higher temporal resolution of 1000 Hz and the best one documented so far in analogue experiments. A test experiment of a convergent wedge model and the data recorded by both the force sensor and PIV is presented here.

5.2.2) Experimental design

The experimental setup is designed to measure forces of a deforming model in a conventional sand box (Fig. 5.2a). It consists of a rectangular glass box 100 cm long, 30 cm wide and 60 cm deep that sits on a metal bench (Fig.5.2b, c). At one end of the box a moving back wall is held by a metal bar that slides along tracks on either side of the glass box. The bar is attached to a motor which is controlled by an in-house built computer software and has the possibility to move horizontally at a constant velocity or constant force. Between the bar that holds the back wall and the back wall itself, there is a force sensor (Fig. 5.2b). The force sensor is a Megatron C beam force sensor with a maximum load capacity of 500 N. Any force applied on the back is sensed by the force sensor and recorded by the same software that controls the movement of the back wall. The back wall is made of a certain thickness (>5 mm) so that it does not bend under the load of the deforming granular material. The box is long enough that the force reading is not affected by the force exert by the opposite end of the box (opposite to the back wall) on the deforming material. The elasticity of the force sensor is greater than that of the moving back wall (Fig. 5.2a). The force is measured at a sampling rate of 1000 Hz and the experiment is recorded from the top using digital cameras (CCD, 11 MPx, 16 bit) of the PIV system. The box is designed in such a way that it is versatile to be used in many tectonic settings; in this case a convergent wedge is presented.

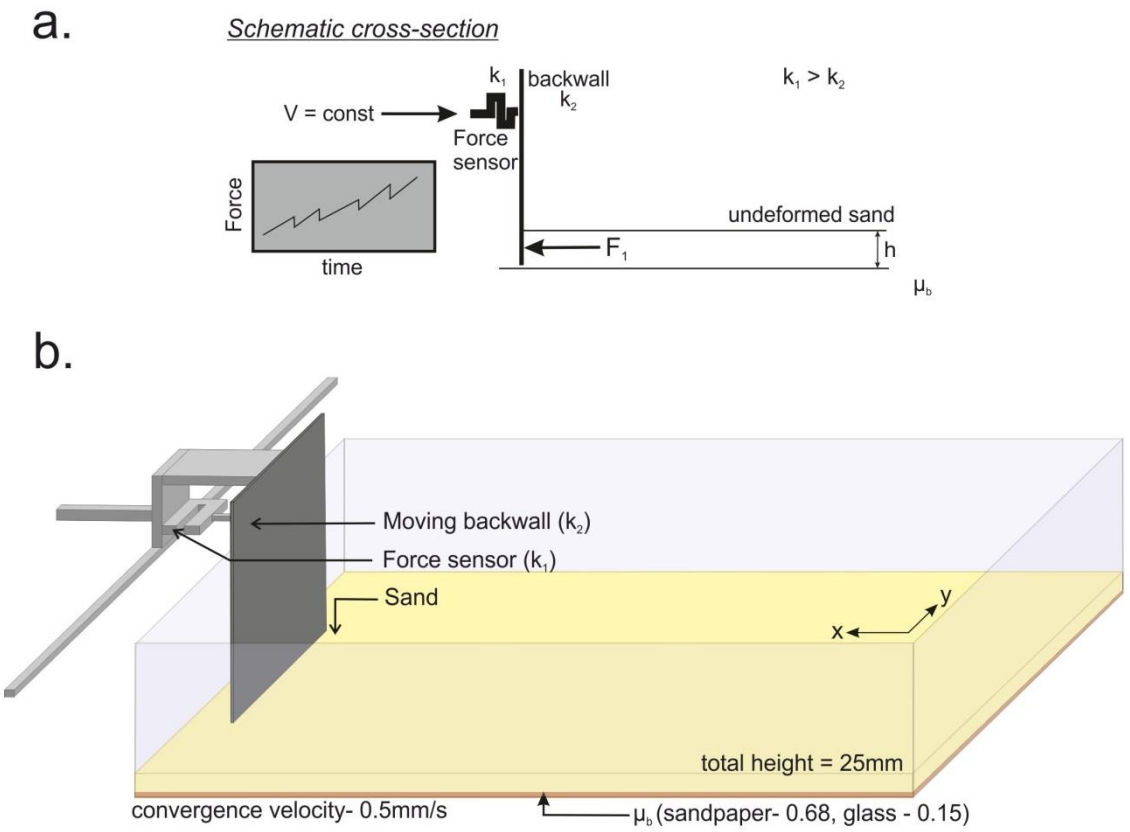

Figure 5.2-a) Schematic cross-section of the experimental design b) Experimental setup for the convergent sand wedge experiments.

5.2.3) Compressional wedge experiments

Compressional sand wedge experiments are used to characterize and analyze the change in force in the new setup. The main focus is on the evolving stress regime especially during the formation of a new fault at each accretionary cycle. To form the wedge the initial setup consist of a 2 cm layer of sand (coefficient of internal friction μ ~ 0.6) sieved over sand paper made with the same sand that is sieved in the box. The velocity of the back wall is 0.5 mm/s. In this setup, the back wall hangs a few mm above the bottom of the sand paper so that it does not drag on the bottom and affect the force measurements. The back wall is also approximately 10 cm away from the glass side walls of the box, thus reducing any effect of the side walls on the deforming sand layer (Souloumiac et al., 2012). As a result the deformed sand is allowed to subside along the sides of the back wall.

5.2.4) Data produced

5.2.4.1) PIV data

The horizontal plane of the experiments is recorded from above using PIV cameras (CCD, 11 MPx, 16 bit) at a frequency of 1 Hz for the convergent wedges experiments. To minimize

the noise and to record only the area of interest, the field of view consists of only the experiment i.e. the deforming sand layer. However the moving back wall and metal bar holding the back wall do enter the field of view in the duration of the experiment. To ensure that these moving mechanical parts of the setup are omitted from the post-processing, they are covered with a black light-absorbing cloth or painted black so that they are recorded as dark objects (i.e. zero intensity) and can be easily filtered from the images. Image data are calibrated and cross-correlated for deriving incremental displacement (i.e. velocity) fields (Adam et al., 2005).

Maps of the displacement field (Fig. 5.3) indicate strain in the y direction. The arrows on the side of the back wall show the subsidence of material. To quantify the deformation due to shortening of the wedge in each time step a zone is defined omitting the edges of the back wall where subsidence of sand from the growing wedge occurs. To better visualize the evolution of the deformation in the wedge, the cumulative displacement in this zone is averaged along the x axis. The displacement along the x axis for each time step is assembled together to produce a map of deformation (Fig. 5.4a). From these deformation maps the formation of a new fault is highlighted by a sharp change in the location of the displacement along the x-axis (Fig. 5.4a).

5.2.4.2) Force data

Measurements from the force sensor (Fig. 5.4b) are recorded digitally at a frequency of 1000 Hz by an in-house built software. Due to the experimental setup, the force sensor does not measure the force that the sand applies on the back wall directly. However, the force is measured at a certain height above the deformed layer. Therefore, the lever effect of the pivoting back wall is taken into consideration and the force measurements are corrected accordingly. Since the force sensor records the entire load against the back wall the force recordings represent the total load parallel to the convergence direction. The high frequency recordings from the force sensor capture two processes recognized as large decreases in force on the order tens of newtons caused by faulting and small decreases in force on the order of few newtons caused by internal deformation and re-arrangement of the sand grains (Fig. 5.3). The small scale deformation (Fig. 5.4c) can be characterized by a distinct amplitude and frequency of the force drops (Fig. 5.5). The varying scale of force recording is similar to those seen in the study by Nieuwland et al. (2000). A first-order observation of the smaller scale force recording shows that both amplitude and the frequency are positively correlated and increase as the wedge grows. The next step would be to correlate the PIV and force recordings in more detail to visualize how changes in the forces affect the topography of the wedge.

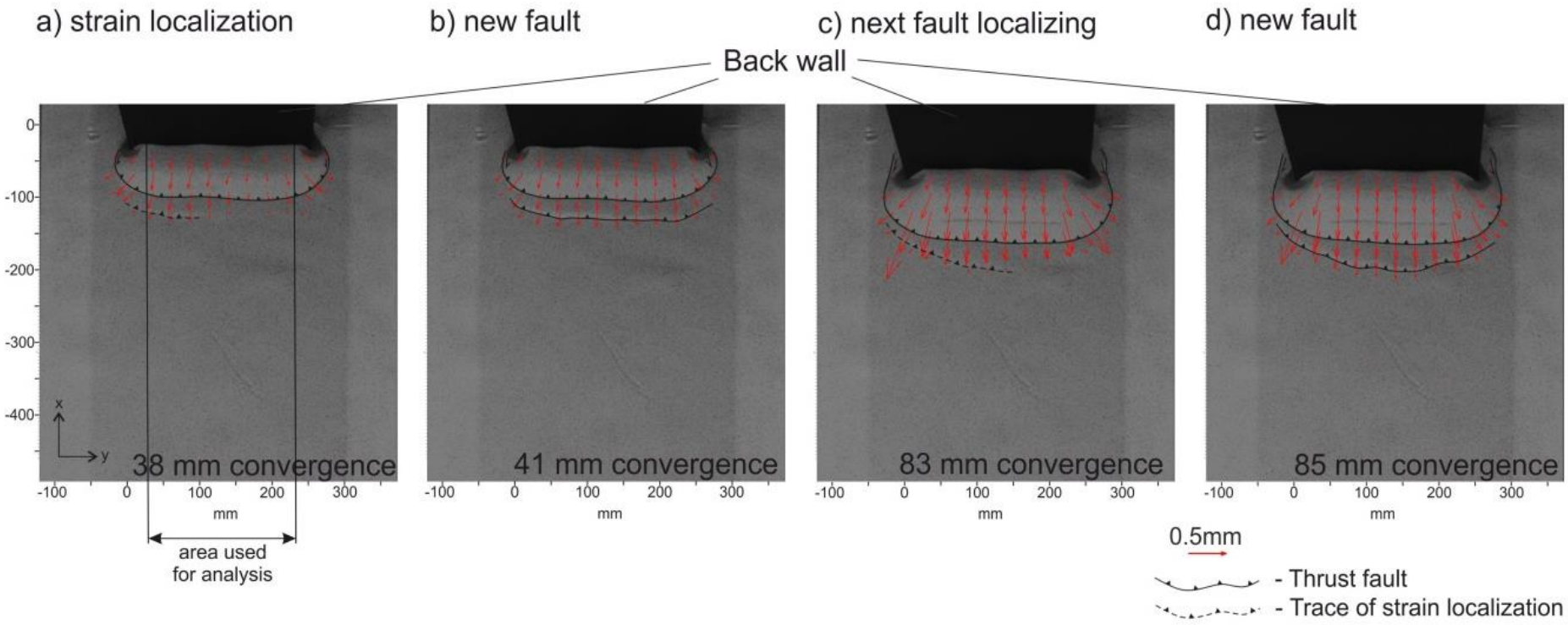

Figure 5.3- Top view of the convergent sand wedge experiments showing a) strain localization, b) formation of a new fault, c) strain localization before the next fault and d) formation of the next fault. Length of the arrows indicates the magnitude of the displacement and direction. To avoid the subsidence of sand on the sides of the wedge in the analysis, only the area highlighted in image 5.3a is analyzed. Together the images show the transition between two accretionary cycles.

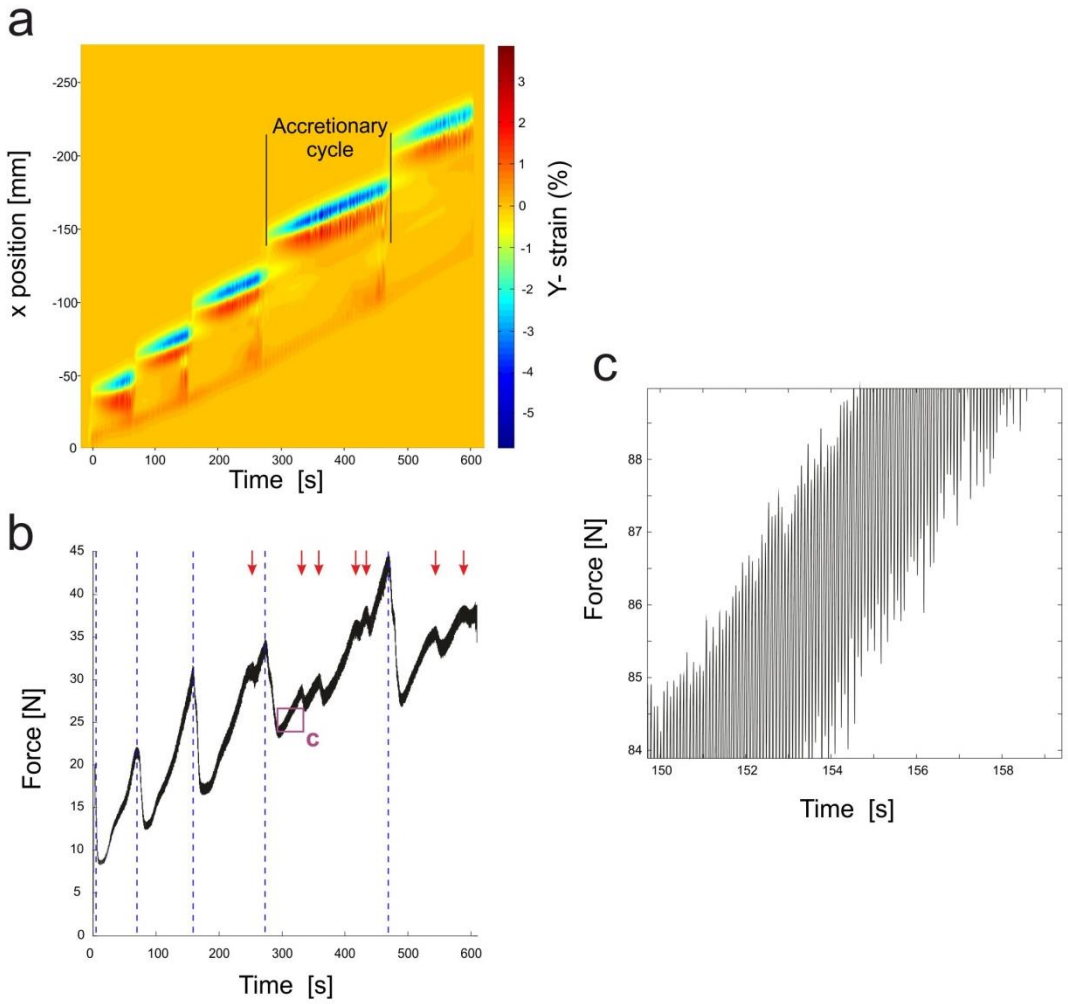

Figure 5.4- a) Strain map and b) force data for the convergent sand wedge. An accretionary cycle is defined in (a) can be correlated to a faulting event and the drop in force seen in (b) and highlighted with a blue dashed line. The small force drops pointed with a red arrow in the force graph are due to small faults formed at the sides of the wedge and outside the marked area in Figure 5.3. c) A magnification of the force data of the inset in b showing the small scale deformation.

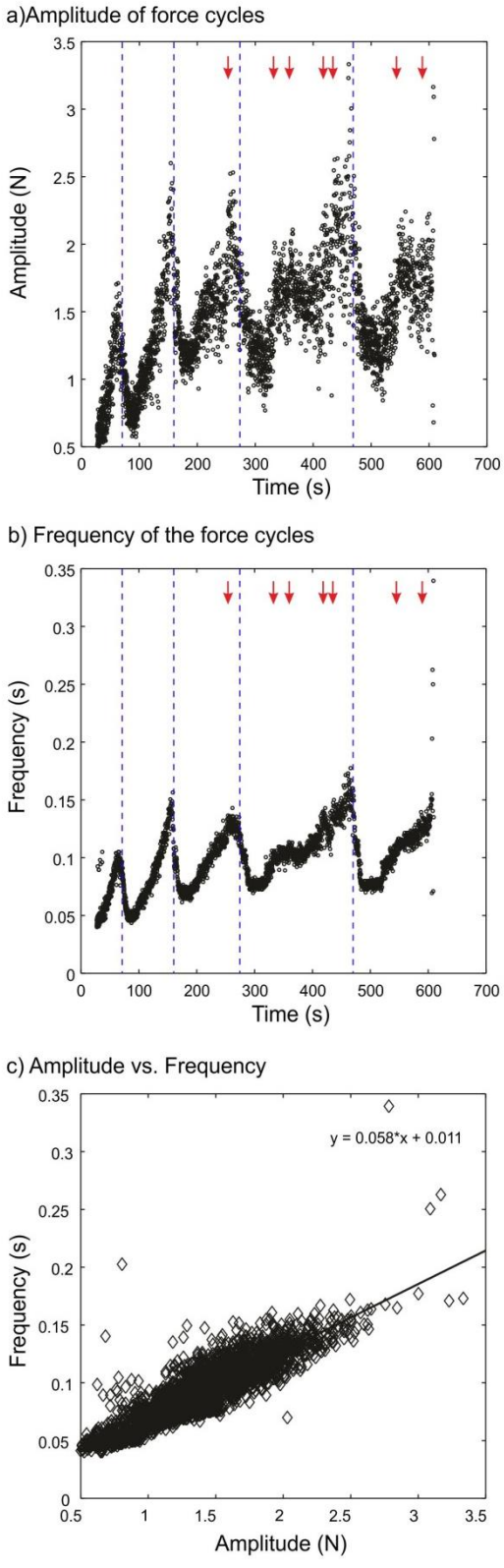

Figure 5.5- Trend of the a) amplitude and b) frequency of the force data for the convergent wedge experiment. Similar to Figure 5.4b, the vertical blue dashed lines correspond to large fault events seen in Figure 5.4a and red arrow correspond to small faults. c) Plot showing the linear relationship between frequency and amplitude.

References

Adam, J., Urai, J.L., Wieneke, B., Oncken, O., Pfeifer, K., Kukowski, N., Lohrmann, J., Hoth, S., van der Zee, W., Schmatz, J., 2005. Shear localization and strain distribution during tectonic faulting- new insights from granular-flow experiments and high-resolution optical image correlation techniques. Journal of Structural Geology 27, 283-301.

Boutelier, D., Oncken, O, 2011. 3-D thermo-mechanical laboratory modeling of plate-tectonics: modeling scheme, technique and first experiments. Solid Earth 2, 35-51.

Cruz, L., Malinski, J., Wilson, A., Take, W.A., Hilley, G., 2010. Erosional control of the kinematics and geometry of fold-and-thrust belts imaged in a physical and numerical sandbox. Journal of Geophysical Research 115, B09404, doi:10.1029/2010JB007472.

Daniels, K.E., Hayman, N.W., 2008. Force chains in seismogenic faults visualized with photoelastic granular shear experiments. Journal of Geophysical Research 113, B11411, doi:10.1029/2008JB005781.

Di Giuseppe, E., Corbi, F., Funiciello, F., Massmeyer, A., Santimano, T.N., Rosenau, M., Davaille, A., 2014. Characterization of Carbopol hydrogel rheology for experimental tectonics and geodynamics. Tectonophysics. doi:10.1016/j.tecto.2014.12.005

Lubrizol, 2009. Neutralizing Carbopol and pelumen polymers in aqueous and hydroalcoholic systems. Lubrizol Technical Data Sheet 237, pp. 1-3

Massmeyer, A., Di Giuseppe, E., Davaille, A., Rolf, T., Tackley, P., 2013 Numerical simulation of thermal plumes in a Herschel-Bulkley fluid. Journal of Non-Newtonian Fluid Mechanics. 195, 32-45

Mezger, T.G., 2006. The Rheology Handbook. 2nd revised edition. Vincentz Network, Hannover.

Nieuwland, D.A., Urai, J.L., Knoop, M., 2000. In-situ stress measurements in model experiments of tectonic faulting. In: Lehner, F.K. and Urai, J.L. (Eds.), Aspects of tectonic faulting- In Honour of Georg Mandl. Springer-Verlag, pp.155-167, Berlin

Reber, J.E., Lavier, L.L., Hayman, N.W., 2015. Experimental demonstration of a semi-brittle origin for crustal strain transients. Nature geoscience. doi: 10.1038/NGEO2496

Schrank, C.E., Boutelier, D.A., Cruden, A.R., 2008. The analogue shear zone: From rheology to associated geometry. Journal of Structural Geology 30. 177 -193.

Souloumiac, P., Maillot, B., Leroy, Y.M., 2012. Bias due to side wall friction in sand box experiments. Journal of Structural Geology 35, 90-101.

Conclusion

In Chapter two the statistical analysis confirmed that analogue models are repeatable and quantifies the degree of repeatability using the statistical test ANOVA. Not only is the difference in μ_{basal} between the wedges distinguishable in the results, but the test also identifies that repeatability (R^2) decreases as a function of decreasing μ_{basal}. In addition, fault and wedge observable, although from the same experimental setup, have different magnitudes of variability. This is because observables that are not time-dependent in this study like fault dip are least variable while variables that are time dependent and change with the evolution and geometry of the wedge like fault spacing and lifetime and wedge slope are more variable. Moreover, these results indicate that the intrinsic variability is related to the mechanical and dynamic processes in the wedge. This approach of repeating experiments quantifies the intrinsic variability due to geodynamic processes. It can also be used as a proxy for the strength of the interpretations made from, especially, complex experiments.

Faults being the main structures that control the lengthening or uplift of the wedge, are the focus in Chapter three. The change in fault dip i.e. the rotation of the fault over the life of an accretionary cycle and over the entire evolution of the wedge is described. Activity of first order faults and reactivated faults are also described. Together the change in geometry and fault activity is explained mechanically to understand how they affect the shape of the wedge. As the wedge matures the governing factors that controls slip along faults are the geometry of the fault plane and the friction along the fault plane. Temporal observations of fault activity and correlation with wedge characteristics demonstrate that fault activity governs the characteristics of the wedge and eventual zonation of the wedge. In addition, the rate at which these zones form and the initial conditions of the wedge are dependent on the initial physical properties of the wedge. A wedge with higher μ_{basal} needs a larger amount of shortening to develop zones than a wedge with lower μ_{basal}.

In Chapter four, the evolution of the wedge is compared to the two theories used to explain the mechanics of deformation in the wedge 1) the critical taper theory and 2) the minimum work theory. Comparison of the work done by the wedge and the geometry of the wedge over several accretionary cycle reveals that the wedge can be considered to be criticality at the beginning of an accretionary cycle and performing minimum work at the end of an accretionary cycle. Over the progression of each accretionary cycle the wedge dynamics moves towards an "ideal state" of being a critical taper wedge and minimum work wedge at the same time. However, a complete "ideal state" is never met. Thus the wedge finds a balance between these two energetic and geometric end member states. Therefore the evolution of the wedge is a competition between the critical taper theory and the minimum work theory. Specifically the critical taper theory determines the geometry of the wedge while the minimum work theory determines the path of deformation needed to meet that geometry.

Although analogue sand wedges are only models they do behave mechanically similar to natural wedges and reliably provide a high temporal resolution of deformation processes to be

observed. Results of this thesis have key implications on the interpretations that are made from analogue models or how theory like the critical taper theory is applied to natural settings. The repeating of experiments and quantification of intrinsic variability determines the robustness of the data and makes for better interpretations. In addition, the result that wedges are not always model critical taper or minimum work wedges indicates that the application of the critical taper theory to natural setting should be made when the natural wedge is at or closest to criticality. Overall, with the statistical study, the focus of the main structural feature and the comparison of theories this thesis presents a systematic approach toward addressing the complex deformation patterns in accretionary wedges.

Acknowledgements

The journey and successful completion of my Ph.D. would not be possible with only my hard work and persistence. There was a series of events that aligned together even before I started my Ph.D. that allowed me to reach my goal. This series of events were influenced by a lot of people who entered my life, and whom I am grateful for, with them I celebrate and share my work.

To my three supervisors Dr. Matthias Rosenau, Prof. Onno Oncken and Dr. Francesca Funiciello, I have the utmost gratitude. Matthias, who I jokingly but dearly call "Vorgesetzter", was incredibly patient with me. What I learnt from him especially is how to take my blurry cloud of ideas and to creatively and clearly present them in a nice graph. From Prof. Oncken I learnt how to put my results in the context of the "big picture". Together they were the perfect scientific advisors. Thank you for being so patient and showing me another intellectual level with our few but very enjoyable discussions on observations, uncertainties and the philosophy of doing research. Thank you also for encouraging my extra-curricular endeavors at Ph.D. day and Lange Nacht. Francesca will always be a great role model not only as a strong scientist but as a strong female scientist. I wish I worked more with her but in the few months that I spent in Rome each year, I learnt a lot about the work and personal life balance. Thank you Prof. Oncken, Vorgesetzter and Fra for choosing me to be part of the Marie Curie TOPOMOD team and for giving me this valuable life opportunity.

I have a great appreciation for Prof. Ulrich Riller (my Masters advisor) and Prof. Petra Arck (Prof. Riller's wife) for introducing me to their homeland. Prof. Riller's most important advice to me at the beginning of my Ph.D. was to "Think like a plain geologist the tools will follow, and you will find them at the GFZ". This advice greatly helped. In 2010 Prof. Arck suggested that I use my travel grant (that I won as a Masters student in Canada) to visit Germany with her and the analogue lab at the GFZ since I had great interest in this field. This was my first exposure to the GFZ and an experience where I wanted to take in as much as possible not knowing when and if I would return.

Thank you to Vasso for her wonderful and down to Earth positivity, Fabio for all the encouragement and motivational talks over gelatos and Karen for reminding me of my capabilities as a researcher for encouraging me. Thank you to all three for proof-reading my long sentences and chapters of this thesis.

I am very grateful to all the friends I made in Germany and all the people that put a smile on my face and that I shared a laugh with, especially all the former and present Ph.D. students of section 3.1, Thomas and Frank in the analogue lab. To Fang-Lin Wang I owe my introduction and knowledge of all the tricks in analogue modeling world. Thank you for also helping me discover the beauty and delicious places of Berlin. To Natalia, I am grateful for your listening ears, calming attitude and patience over many coffees around Berlin, Stralsund and in Potsdam especially Balzac. Thanks for also sharing in the tough moments especially at the end of the Ph.D. Thank you Isabelle for always laughing so freely with me, for reminding me to look at the brighter side of things, for trying to teach me Spanish (one day I will learn more than "cola frio"). You have been a great officemate.

Many thanks to Franziska for wishing me well before every talk and or concert and for being my "cheer leader". Many thanks to the Claudius Ensemble for making me part of your choir and for breaking up my thesis writing process with music, singing and most importantly

breathing. Together you showed me a different side of the German culture especially your passion for music.

Seema and Heiko, thank you very much for showing me a greener and healthier side of life. To Ameya and Mira (also my Godchild) thank you for keeping me sane and normal and teaching me that "I am not a lump of sugar and I won't melt in heavy rainfall". I am very grateful to Seema who has become a "Didi" (Big sister) to me, who checks up on me and feeds me and has always time to make me a glass of warm ginger chai.

I would like to also thank the TOPOMOD family for all the great unforgettable memories during field trip and workshops. A special thank you to my friends in Canada and around the world especially Emileen, Saira, Sharon, Aarthi, Nadia, Silvina, Yolanda who kept in touch and asked me how I was doing every now and then. To my dear parents Samson and Virginia and my brother Rahul thank you for encouraging me throughout my Ph.D. and for visiting me and sharing beautiful places in Europe with me.

Lastly, as inanimate as the Analog labor is, I have a special fondness and liking for this space. This is my favorite place on the beautiful Telegrafenberg. It was the first building I stepped into back in 2010 when I came to visit, not knowing of the rest of the GFZ and what the future would hold. It always welcomed me and like nature never judges its guests. This space allowed me to be creative, it offered me a playground to develop my ideas.

I am here not entirely on my own merit but with the enormous support of the people mentioned above. My father once told me that a person's destiny is already written for them. If someone told me six years ago that I would be doing a Ph.D., I would have laughed hysterically. Now, in hindsight with all the experiences and the people I met over the last four years, I do believe that a Ph.D. especially in Germany was written in my destiny and the above mentioned people made this journey even more wonderful and a richer experience.

The historical A14 building that houses the Analog labor. Don't be fooled by the simple and quiet exterior, on the inside it is a world of opportunity

Erklärung

Hiermit versichere ich, dass die vorliegende Dissertation ohne unzulässige Hilfe Dritter und ohne Benutzung anderer als der angegebenen Literatur angefertigt wurde. Die Stellen der Arbeit, die anderen Werken wörtlich oder inhaltlich entnommen sind, wurden durch entsprechende Angaben der Quellen kenntlich gemacht. Diese Arbeit hat in gleicher oder ähnlicher Form noch keiner Prüfungsbehörde vorgelegen.

Potsdam,
September 2015

Tasca Noela Santimano
Curriculum Vitae

EDUCATION

German Research Centre for Geosciences (GFZ) 2011- 2016
Freie Universität, Berlin Defence- Early 2016
Marie Curie Ph.D. Fellow
(EU Initial Training Network project TOPOMOD)
Thesis title: Kinematic complexity of accretionary wedges- Insights from analogue models towards understanding natural wedges

McMaster University, Hamilton 2009-2010
Masters of Science
Thesis title: Kinematics and mechanisms of upper-crustal deformation in the Eastern Cordillera, southern Central Andes, NW Argentina.

University of Toronto, Toronto 1999-2004
Honours Bachelor of Science
Major: Earth and Environmental Science
Minor: Biology

PROFESSIONAL EXPERIENCE

Research Assistant at McMaster University, Hamilton 2011

Teaching Assistant at McMaster University, Hamilton 2009-2011

Project Geologist at Wallbridge Mining Ltd., Sudbury 2007-2008

Field Geologist at Wallbridge Mining Ltd., Sudbury 2006

AWARDS

2011	Jack Henderson Award for best M.Sc. thesis, awarded by the Structural Geology and Tectonics Division of the Geological Association of Canada.
2010	Mineralogical Association of Canada travel grant.

PROFESSIONAL AFFILIATIONS

2013-2014	Ph.D. student representative for TOPOMOD
2012-2013	Ph.D. student representative at the GFZ
2010-2014	Member, European Geoscience Union
2008-2014	Member, American Geophysical Union
2008-2011	Member, Mineralogical Association of Canada

PUBLICATIONS

Submitted or in preparation

Riller, U., Clark M., Daxberger, H., Doman, D., Lenauer, I., Plath, S., **Santimano, T**. Fault-slip inversions: their importance in terms of strain, heterogeneity and kinematics of brittle deformation. *Journal of Structural Geology*- In review

Santimano, T., Rosenau, M., Oncken, O. Smart or beautiful? Accretionary wedge evolution seen as a competition between minimum work and critical taper. *Geology* – In review

Santimano, T., Ritter, M.C., Rosenau, M., Leever, K., Oncken, O. Stress and strain in sand box models- Insights from a high resolution force recording and image correlation setup. *Tectonophysics*- In preparation

Refereed journals

Santimano, T., Rosenau, M., Oncken, O. On the intrinsic variability of analogue sand-box experiments-insights from statistical analysis of repeated analogue experiments of accreationary sand wedges. *Journal of Structural Geology*. doi:10.1016/j.jsg.2015.03.008

Di Giuseppe, E., Corbi, F., Funiciello, F., Massmeyer, A., **Santimano, T.N.**, Rosenau, M., Davaille, A. (2014) Characterization of Carbopol® hydrogel rheology for experimental tectonics and geodynamics. *Tectonophysics*. doi:10.1016/j.tecto.2014.12.005

Santimano, T., Riller, U. (2012b) Kinematics of Tertiary to Pleistocene intracontinental deformation of upper crust in the Eastern Cordillera, southern Central Andes, NW Argentina. *Tectonics*. doi: 10.1029/2011TC003068

Santimano, T., Riller, U. (2012a) Revisiting thrusting, reverse faulting and transpression in the southern Sudbury Basin, Ontario. *Precambrian Research*. doi.10.1016/j.precamres.2012.01.012.

Dreuse, R., Doman, D., **Santimano, T.**, Riller, U. (2010) Crater-floor topography and impact melt sheet geometry of the Sudbury impact structure, Canada. *Terra Nova*. doi: 10.1111/j.1365-3121.2010.00965.x

Riller, U., Fletcher, S., **Santimano, T.** (2009) Sudbury area, Ontario: meteorite impact, ore deposits and regional geology. Field trip guide book for the Geological Association of Canada - Mineralogical Association of Canada. 43 pages.